Spring 2021

Data-Driven Approaches to Complex Materials: Applications to Amorphous Solids

Dil Kumar Limbu

DATA-DRIVEN APPROACHES TO COMPLEX MATERIALS: APPLICATIONS TO AMORPHOUS SOLIDS

by

Dil Kumar Limbu

A Dissertation
Submitted to the Graduate School,
the College of Arts and Sciences
and the School of Mathematics and Natural Sciences
at The University of Southern Mississippi
in Partial Fulfillment of the Requirements
for the Degree of Doctor of Philosophy

Approved by:

Dr. Parthapratim Biswas, Committee Chair
Dr. Christopher Winstead
Dr. Khin Maung Maung
Dr. Sungwook Lee
Dr. Andrew Sung

May 2021

Published by the Graduate School

THE UNIVERSITY OF
SOUTHERN
MISSISSIPPI®

ABSTRACT

While conventional approaches to materials modeling made significant contributions and advanced our understanding of materials properties in the past decades, these approaches often cannot be applied to disordered materials (e.g., glasses) for which accurate total-energy functionals or forces are either not available or it is infeasible to employ due to computational complexities associated with modeling disordered solids in the absence of translational symmetry. In this dissertation, a number of information-driven probabilistic methods were developed for the structural determination of a range of materials including disordered solids to transition metal clusters. The ground-state structures of transition-metal clusters of iron, nickel, and copper were determined by a force-biased Monte Carlo method and their structural and electronic properties were studied comparatively via force-biased Monte Carlo and *ab initio* simulations. The force-biased Monte Carlo approach has shown unambiguously that it can effectively determine the putative ground-state structures of a number of small transition-metal clusters.

For complex amorphous materials, an information-driven probabilistic viewpoint was adopted by posing structural determination of disordered solids as an inferential program and the problem of materials design was addressed as an optimization program, jointly supported by experimental data and information. The hallmark of this new approach is that it can produce atomistic configurations of amorphous solids, which are thermodynamically stable and close to a stable local minimum of a quantum-mechanical total-energy functional. The models have structural, topological, electronic, and vibrational properties comparable to experiments. The data-driven approach presented here for amorphous solids not only can produce overall structural and electronic properties but also the microstructural properties of realistic samples from experiments, such as voids and vacancy-type defects, which cannot be addressed directly using currently available computational methods. *Ab initio* hydrogen dynamics were simulated inside nanometer-size voids in *a*-Si within the framework of the density-functional theory and the study revealed that the microstructure of the hydrogen distribution and the morphology of the voids were characterized by the presence of a significant number of monohydride Si–H bonds, along with a few dihydride Si–H_2 configurations but not any isolated hydrogen. The study also revealed that a considerable number of total H atoms inside voids can appear as H_2 molecules. The densities of the bonded and non-bonded hydrogens are observed to be consistent with those from the infrared and Rutherford backscattering spectrometry measurements.

ACKNOWLEDGMENTS

I would like to express my deep gratitude to my advisor Dr. Parthapratim Biswas for his continuous support, guidance, and motivation throughout the process of getting my Ph.D. His scientific insights and pedagogical excellence nurtured me throughout my graduate career and helped me reach higher than what I thought possible.

I want to sincerely thank the members of this dissertation committee: Dr. Christopher Winstead, Dr. Khin Maung Maung, Dr. Sungwook Lee, and Dr. Andrew Sung for their challenging support, feedback, and advice throughout my studies. Also, I would like to thank Prof. Ras B. Pandey for providing valuable suggestions and comments during the completion of my Ph.D.

I like to thank my collaborators: Dr. Raymond Atta-Fynn (The University of Texas at Arlington), Prof. David A. Drabold (Ohio University), and Prof. Stephen R. Elliott (University of Cambridge), for their continuous feedback and valuable correction of my research work. Also, I would like to thank my colleague and senior group member Dr. Durga Paudel and fellow member Devilal Dahal for wonderful discussions, comments and suggestions, and fond memories.

I would like to extend my acknowledgment to the School of Mathematics and Natural Sciences, USM, for providing me the opportunity to be a graduate student and pursue my studies in this institution. I would like to thank National Science Foundation for partially funding financial support during my study.

Lastly, I would like to express my endless gratitude to my wife for her constant love, support, care, and motivation throughout my studies. I would like to extend my gratitude to the entire family of me and my wife for their unconditional support and encouragement throughout these years. They have always been on my side whenever I needed them during my Ph.D. journey. Without their constant support and encouragement, it would not be possible to achieve this goal.

DEDICATION

To my late mother,

To my son, Yuhang Limbu,

and

To my beloved wife, Parina Rai.

TABLE OF CONTENTS

ABSTRACT ii

ACKNOWLEDGMENTS iii

DEDICATION iv

LIST OF TABLES vii

LIST OF ILLUSTRATIONS viii

LIST OF ABBREVIATIONS xii

LIST OF PUBLICATIONS xiii

1 INTRODUCTION **1**
1.1 Amorphous Semiconductors 1
1.2 Amorphous Silicon 2
1.3 Modeling Methods of Amorphous Solids 4
1.3.1 Continuous Random Networks (CRN) 5
1.3.2 Wooten-Weaire-Winer (WWW) Method 6
1.3.3 Monte Carlo (MC) Method 6
1.3.4 Molecular Dynamics (MD) Simulation Method 7
1.3.5 Density Functional Theory (DFT) 7
1.4 Inverting Information: revised Reverse Monte Carlo (RMC) Method 10
1.5 Dissertation Outline 11

2 COMMON DESCRIPTORS OF AMORPHOUS SOLIDS **13**
2.1 Pair Distribution Function 13
2.2 Structure Factor 15
2.3 Bond-Angle Distribution 16
2.4 Ring Statistics 17
2.5 Electronic Structure 18
2.6 Vibrational Properties and Specific Heat Capacity 18

3 INFORMATION-DRIVEN INVERSE APPROACH **20**
3.1 Introduction 20
3.2 Computational Method 22
3.3 Results and Discussions 27

3.3.1 Structural Properties 28
3.3.2 Electronic and Vibrational Properties 37
3.4 Conclusions 40

4 DISORDER BY DESIGN: A DATA-DRIVEN APPROACH 42
4.1 Introduction 42
4.2 Materials and Methods 44
4.3 Results and Discussion 47
4.3.1 Comparison with earlier RMC-derived models 48
4.3.2 Comparison with total-energy-based models 49
4.3.3 Electronic properties of amorphous silicon from CMC19 54
4.3.4 Microstructure of *a*-Si: Modeling vacancies and voids via CMC19 59
4.4 Conclusions 61

5 *AB INITIO* HYDROGEN DYNAMICS AND MORPHOLOGY OF VOIDS . 63
5.1 Introduction 63
5.2 Method 65
5.3 Results and Discussion 67
5.3.1 Hydrogen dynamics inside voids in *a*-Si 67
5.3.2 Kinetics of Si–H bond formation and dissociation on the surface of voids 71
5.3.3 Hydrogen microstructure and morphology of voids in *a*-Si 74
5.4 Conclusions 80

6 TRANSITON-METAL CLUSTERS VIA FORCE-BIASED MONTE CARLO AND *AB INITIO* CALCULATIONS 81
6.1 Introduction 81
6.2 Structure of transition-metal clusters: An overview 82
6.3 Computational Method 85
6.4 Results and Discussions 88
6.4.1 Global minima from the classical FMC simulations 88
6.4.2 Part I: Structure of 13-atom Cu/Ni/Fe clusters from *ab initio* studies 89
6.4.3 Part II: Structure of 13-atom Cu/Ag clusters from *ab initio* studies 92
6.4.4 Local atomic structure and bonding environment 96
6.4.5 Bond-orientational order parameter 98
6.4.6 Geometry of transition-metal clusters 102
6.5 Conclusions 107

7 SUMMARY 109

BIBLIOGRAPHY 111

LIST OF TABLES

Table

3.1 Modified Stillinger-Weber (SW) potential parameters. 27
3.2 Structural properties of *ab initio*-relaxed INDIA, MD, and WWW models. Average bond length, the average bond angles, RMS deviations, and the percentage of n-fold coordinated atoms are denoted by $\langle r \rangle$, $\langle \theta \rangle$, $\Delta\theta(\Delta\theta_G)$ and C_n respectively. 32
3.3 Ring statistics for INDIA, WWW, and two MD models comprising $N = 216$–1024 atoms. 34
3.4 Comparison of band-gap values (in eV) for a-Si models obtained from the INDIA, WWW, and SW-MD simulations. 37

4.1 Comparison of results from various information-based approaches. N, $\langle \theta \rangle$, $\Delta\theta$, c_4 and E_g indicate the size of the system, the average bond angle, the RMS width of bond angles, the percentage of four-fold-coordinated atoms and the value of the electronic gap, respectively. 48
4.2 Comparison of CMC19 models with the best available models (of a-Si). E_g and bond angles are expressed in the unit of electron-volt (eV) and degree, respectively. 51

5.1 Statistics of bonded and non-bonded hydrogens inside voids for varying hydrogen loads. The tabulated values indicate the amount of H atoms (in per cent of total H) and H atoms outside the void region are listed as Ex_H. 75
5.2 Linear (Å) and volumetric (Å^3) measures of the voids, reconstructed from the convex-hull approximation. 79

6.1 Finnis-Sinclair and Sutton-Chen potential parameters 86
6.2 Total energy of Cu, Ni, and Fe clusters from the classical FMC simulation and the corresponding value of the CCD clusters. 89
6.3 Total energy of Fe, Ni, and Cu clusters from *ab initio* relaxation of the FMC and CCD structures. 89
6.4 *Ab initio* total-energy values of 13-atom transition-metal clusters from a joint FMC-NWChem simulation. For Cu_{13}, the energy difference $\Delta E = E - E_{\min}$ is expressed with respect to the lowest-energy configuration. 91
6.5 Total-energy differences (in eV) for 13-atom Cu and Ag clusters from their icosahedral counterpart, using SIESTA and VASP. 92
6.6 Average bond length (d_{av}) and effective coordination number (C_{av}) for Cu and Ag clusters 93

LIST OF ILLUSTRATIONS

Figure

1.1 Schematic diagram of the density of states of the conduction band and the valence band shwon by the brown color. The mobility edge and mobility gab are also shown 2

2.1 (a) Long-range order (LRO) and periodicity exhibited by a 1000-atom model of diamond crystalline silicon. (b) topological disorder exhibited by a 1000-atom model of amorphous silicon. 13
2.2 A schematic illustration of pair-correlation function and the structural origin of certain features in the density function 14
2.3 The PCF of computer-generated crystalline silicon (blue) and amorphous silicon (red). 15
2.4 Schematic illustration relating first and second nearest bond lengths, r_1 and r_2, and bond angle θ from the first two peaks in RDF 17
2.5 A schematic diagram of a irreduble 5-membered ring. 18

3.1 A schematic illustration of the augmented space, $\mathcal{P}$, consisting of the objective-function spaces spanned by the experimental data (red), constraint information (blue), and a total-energy functional (green) 23
3.2 A flowchart of information-driven inverse approach (INDIA) showing information flow during simulations which is capable of generating nearly defect-free configurations of a-Si 26
3.3 Different structural properties of INDIA and WWW models of size 512 atoms: (a) The reduced pair-correlation functions $G(r)$ (b) The corresponding static structure factors $S(k)$ along with experimental data. (c) The (approximate) distributions of Voronoi volumes obtained from the INDIA, WWW and SW-MD models. 30
3.4 The bond-angle distributions $B(\theta)$ of a-Si from 512-atom INDIA (red) and WWW (blue) models. 31
3.5 Dihedral-angle distributions, $P(\phi)$ from 512-atom INDIA and WWW models showing the characteristic dihedral peak at 60° and a dip at 120° 33
3.6 A ball-and-stick representation of a 512-atom INDIA model 33
3.7 The bond-orientational order parameter, Q_l, distribution for the 512-atom INDIA, WWW and SW-MD models. 34
3.8 Ring statistics for INDIA, WWW, SW-MD, and ML-MD models of a-Si of size 512 atoms. 35

3.9 The distribution of the radii of gyration for INDIA, WWW, and SW-MD models of (a) 6-member rings and (b) 7-member rings. The R_g value of 6-member rings for ideal *c*-Si networks is shown by a vertical (green) line in Fig. 3.9(a). 36
3.10 The electronic density of states of *a*-Si from INDIA and WWW models with the Fermi level at 0 eV. 38
3.11 The low-temperature dependence of the specific heat of the 300- and 512-atom INDIA models compared with the experimental data and the classical *Dulong-Petit limit*. 39
3.12 The vibrational densities of states (VDOS) of *a*-Si from 512-atom INDIA and WWW models compared with experimental data from inelastic neutron-scattering measurements 39

4.1 The variation of CPU time (in seconds) with system size N for a single MC move, associated with the evaluation of the objective function (see Eq. (4.1)). The CPU time is found to scale linearly with N. 47
4.2 Different structural properties of *a*-Si from CMC19 models. (a) The structure factor of a 512-atom CMC19 model and BMW3 model compared with experimental data. (b) The bond-angle distribution, $B(\theta)$. (c) The distribution, $T(Q_i)$, of the local tetrahedral order parameter, Q_i. 52
4.3 (a) The statistics of irreducible rings for CMC19 and BMW3 models. (b) The dihedral-angle distribution, $D(\phi)$. (c) The distribution of the resultant displacements of atoms during CMC19 simulations for a 512-atom model. (d) The radial distribution function, (RDF), J(r). 53
4.4 Electronic density of states (EDOS) of *a*-Si near the band gap. (a) The EDOS of *a*-Si before (upper panel) and after (lower panel) *ab initio* relaxation of the CMC19 model. (b) The formation of a clean electronic gap in the unrelaxed 512-atom CMC19 model via hydrogenation; the EDOS before and after H passivation, respectively. (c) A defect state at -3.472 eV and (d) the associated dangling bonds (i.e., 3-fold-coordinated sites) (red) in real space. 56
4.5 Electronic densities of states for *a*-Si from CMC19 models. (a) A 216-atom CMC19 model and its BMW3 counterpart. (b) A 300-atom CMC19 model and BMW3 model. (c) A 512-atom CMC19 model and BMW3 model. (d) The full EDOS of *a*-Si for a 512-atom CMC19 model and a BMW3 model. 57
4.6 Vibrational densities of states from a 512-atom CMC19 and a 512-atom BMW3 model along with experimental data from inelastic neutron-scattering measurements. 58
4.7 Formation of vacancies and voids in *a*-Si via CMC19. (a) A 300-atom CMC19 model with a void of radius 4 Å at the center. (b) The same model after *ab initio* total-energy relaxation, showing the structural stability of the void. (c) A 512-atom CMC19 model with two monovacancies, separated by a distance of 9 Å. (d) The *ab-initio*-relaxed 514-atom model obtained by adding a silicon atom (red) at the center of each vacancy in Fig. 4.7(c). 60

4.8 The EDOS of a 300-atom CMC19 model with a central void of radius 4 Å. . . . 61

5.1 A schematic representation of a void (gray region) in two dimensions. The annular region with Si atoms (green) indicates the void boundary, with a few H atoms (red circles) inside the void. The rest yellow atoms are the bulk Si atoms. 65
5.2 The time evolution of the average number of H atoms (including H_2 molecules) within a void at 400 and 700 K. The results correspond to a hydrogen load of: (a) 10 H atoms per void; (b) 30 H atoms per void. 67
5.3 The variation of the mean-square displacement (MSD) of H atoms, averaged over *all hydrogen* in four models, with time for three different hydrogen loads as indicated: (a) 400 K; (b) 700 K. 68
5.4 The time evolution of the MSD of H atoms *within* voids for a hydrogen load of 30 H atoms per void in the LDA (blue) and the GGA (red). The results for 400 and 700 K are shown in (a) and (b), respectively. 69
5.5 The average (radial) distances of SiH and SiH_2 bonds on the void surface from the center of the void. 70
5.6 The instantaneous kinetic energy (KE) of H atoms in two voids (in models M2 and M3) at 400 K, obtained from the GGA with a hydrogen load of (a) 10 H atoms per void, and (b) 30 H atoms per void, respectively. 71
5.7 The distribution of kinetic energy (KE) along the *y* axis for H atoms inside a void (in model M4) at 700 K. 71
5.8 The kinetics of Si–H bond formation and dissociation at 700 K for a hydrogen load of 30 H atoms per void obtained from the GGA in model M4. 72
5.9 The evolution of the kinetic energy (KE) of two H atoms, H2 and H30, in monohydride Si–H bonds at 700 K. (a) for stable monohydride (b) The Si–H bond which dissociates and forms a new Si–H bond shortly thereafter 72
5.10 (a) The variation of the bond length of a stable monohydride pair (Si40, H2) with time. (b) The dissociation of a monohydride Si–H bond during MD simulations. 73
5.11 Hydrogen-bonding configurations, including H_2 molecules, in a void-surface region of radius 8 Å for a hydrogen load of 30 H atoms per void at (a) 400 K and (b) 700 K from the GGA in model M4. 75
5.12 Histograms showing the content of H atoms (in at. %) in bonded and non-bonded hydrogens in the vicinity of voids in *a*-Si for a hydrogen load of 20 H atoms per void at 400 and 700 K. 76
5.13 The evolution of monohydride Si–H bonds at 400 K in the GGA and the LDA for a hydrogen load of 20 H atoms per void. (b) The formation of H_2 molecules within a void at 400 K in the GGA for a hydrogen load of 20 H atoms per void. 77

5.14 The reconstruction of a three-dimensional shape of a void (in M3) from two sets of void-surface atoms at 400 K for a hydrogen load of 30 H atoms per void. The convex polyhedra obtained from the void-surface atoms in (a) the GGA and (b) the LDA, using the convex-hull approximation. The corresponding non-convex surfaces using the same set of void-surface atoms are shown in (c) and (d), respectively. 78

6.1 The evolution of the total energy of an Fe_{55} cluster in the classical FMC and MC simulations. a) Total energy versus CPU time, b) Total energy versus MCS steps. 90
6.2 The putative ground-state structures of 13-atom transition-metal clusters from a joint FMC-NWChem simulation: a) Fe_{13} (icosahedron); b) Cu_{13} (bilayer2) with a buckled hexagonal layer (yellow); and c) Ni_{13} (icosahedron). 91
6.3 The structure of putative global minimum of a) 13-atom Cu cluster and b) 13-atom Ag cluster. 93
6.4 The structure of local minimum of 13-atom icosahedral, BBP and bilayer Cu cluster. 94
6.5 The structure of local minimum of 13-atom icosahedral, BBP and bilayer Ag cluster. 95
6.6 The pair-correlation functions for a) Fe, b) Ni, and c) Cu clusters from the FMC simulations and the corresponding CCD clusters 96
6.7 The pair-correlation functions of: a) Fe_{30}; b) Ni_{30}; and c) Cu_{30} clusters obtained from *ab initio* relaxations of FMC (blue) and CCD (red) structures using the density-functional code NWChem. 97
6.8 Bond-angle distributions for a) Fe, b) Ni, and c) Cu clusters from the FMC and CCD structures. 99
6.9 The distribution of the nearest-neighbor bond angles for *ab initio* NWChem relaxed: a) Fe_{30}; b) Ni_{30}; and c) Cu_{30} clusters. 100
6.10 Histograms showing the coordination numbers of the first-shell atoms in: a) Fe_{30}; b) Ni_{30}; and c) Cu_{30} clusters. The FMC-NWChem and CCD-NWChem configurations are indicated in the plots. 101
6.11 Bond-orientational order parameters (Q_l) for *ab initio* NWChem relaxed: a) Fe_{30}; b) Ni_{30}; and c) Cu_{30} clusters for several values of l. 103
6.12 Geometry of Fe_{30}, Ni_{30}, and Cu_{30} clusters obtained from *ab initio* NWChem relaxations of the FMC (left panel) and CCD (right panel) clusters. 104
6.13 The structure of 55-atom Fe, Ni, and Cu clusters obtained from the *ab initio* NWChem relaxation starting from the FMC and CCD configurations. 105
6.14 Electronic densities of states of 30-atom Fe, Ni, and Cu clusters. 106

LIST OF ABBREVIATIONS

***c*-Si**	-	Crystalline Silicon
***a*-Si**	-	Amorphous Silicon
***a*-Ge**	-	Amorphous Germanium
***a*-Si:H**	-	Hydrogenated Amorphous Silicon
SRO	-	Short Range Order
LRO	-	Long Range Order
IR	-	Infrared
DSC	-	Differential Scanning Calorimetry
ESR	-	Electron Spin Resonance
NMR	-	Nuclear Magnetic Resonance
SEM	-	Scaning Electron Microscopy
SAXS	-	Small-Angle X-ray Scattering
DB	-	Dangling Bond
FB	-	Floating Bond
MC	-	Monte Carlo
MD	-	Molecular Dynamics
RMC	-	Reverse Monte Carlo
DFT	-	Density Functional Theory
PCF	-	Pair Correlation Function
RDF	-	Radial Distribution Function
RMS	-	Root Mean Square
DOS	-	Density of States
EDOS	-	Electronic Density of States
VDOS	-	Vibrational Density of States
VASP	-	Vienna *Ab initio* Simulation Package
SIESTA	-	Spanish Initiative of Electronics Simulation with Thousands of Atoms
LDA	-	Local Density Approximation
GGA	-	Generalized Gradient Approximation
SZ	-	Single Zeta
DZ	-	Double Zeta
DZP	-	Double Zeta Polarization
H	-	Hydrogen
Si	-	Silicon
SiH	-	Silcon hydride
CRN	-	Continuous Random Network
WWW	-	Wooten, Winer and Weaire

LIST OF PUBLICATIONS

1. **Structural properties of transition-metal clusters via force-biased Monte Carlo and** *ab initio* **calculations: A comparative study.**
   D. K. Limbu, R. Atta-Fynn, D. A. Drabold, S. R. Elliott, & P. Biswas, *Physical Review B* **96**, 174208 (2017).

2. **Structure of transition metal clusters: A force-biased Monte Carlo approach.**
   D. K. Limbu, & P. Biswas, *Journal of Physics: Conference Series* **921**, 012010 (2017).

3. **Information-driven inverse approach to disordered solids: Applications to amorphous silicon.**
   D. K. Limbu, R. Atta-Fynn, D. A. Drabold, S. R. Elliott, & P. Biswas, *Physical Review Materials* **2**, 115602 (2018).

4. **Structural properties of amorphous graphene: A joint Monte Carlo and particle-swarm approach.**
   B. D. Oli, **D. K. Limbu**, & P. Biswas, *International Conference of Physics*, Mandalya 2018 (ICPM2018), Myanmar.

5. **Atomistic simulation of nearly defect-free models of amorphous silicon: An information-based approach.**
   D. K. Limbu, R. Atta-Fynn, & P. Biswas, *MRS Advances* **4**, 87 (2019).

6. *Ab initio* **density-functional studies of 13-atom Cu and Ag clusters.**
   D. K. Limbu, M. U. Madueke, R. Atta-Fynn, D. A. Drabold, & P. Biswas, *Journal of Physics: Conference Series* **1252**, 012009 (2019).

7. **Disorder by design: A data-driven approach to amorphous semiconductors without total-energy functionals.**
   D. K. Limbu, S. R. Elliott, R. Atta-Fynn, & P. Biswas, *Scientific Reports* **10**, 7742 (2020).

8. *Ab initio* **Hydrogen Dynamics and the Morphology of Voids in Amorphous Silicon.**
   P. Biswas, & **D. K. Limbu**, *physica status solidi (b)*, 2000494 (2021).

Chapter 1

INTRODUCTION

1.1 Amorphous Semiconductors

Amorphous semiconductors are technologically important semiconducting materials that lack the long-range translational and orientational order characteristic of crystalline materials [1]. This means the structure of amorphous materials cannot be expressed as a repetition of 'unit-cell' as analogous to crystalline solids and it is characterized as an irregular arrangement of atoms or molecules meta-stable states [2, 3]. The topological or geometric disorder that arises from the randomness due to positional disorder in the system with no translational periodicity forms the amorphous materials. The degree of local ordering in amorphous materials may vary but all amorphous materials have no long-range ordering of atoms and are distinguished by the absence of periodicity. Despite the lack of long-range ordering, covalent amorphous solids may exhibit structural ordering over both short and medium-length scales, the latter reaching up to 20 Å [4–6].

Amorphous materials can be prepared by some common experimental techniques as thermal evaporation, sputtering, glow-discharge decomposition, chemical vapor deposition, melt quenching, implantation, etc. Several techniques can be used to prepare amorphous materials, but the properties of so produced amorphous materials may not be the same. In principle, an infinite number of possible structures of an amorphous solid with short-range order (SRO) is possible and so the structure of amorphous materials, at both microscopic and macroscopic levels, often depends on the details of the method of preparation.

For crystals, structural ordering is the fundamental concept and a configuration of atoms is arrayed periodically. Experimental probes, like X-ray scattering experiments as "Bragg's diffraction" for crystals, give sharp peaks on structural factor, $S(k)$ [1]. From there, it is possible to uniquely construct a structural model by inverting the experiment. While disorder materials lack the long-range order (LRO) and have very few peaks and vastly less information in the diffraction experiment, it is difficult to invert one-dimensional experimental data alone to fully characterize the information inherent of the amorphous structure of a material, without additional information.

In amorphous semiconductors, the deficient the perfect number of bonding to an atom is known as dangling bond and the dangling bond defect introduces defect states in the

electronic band-gap. Due to the absence of translational symmetry in amorphous semiconductors, the Bloch theory is not applicable to understand the electronic properties of amorphous semiconductors. However, tight-binding approximations, Hartree–Fock calculations, and density functional theory (DFT) methods are applied to study the electronic properties of amorphous materials. The structural defects due to spatial fluctuations of bond lengths, bond angles, and dihedral angles lead to the broadening of the edges of the conduction and valence bands, constructing the band tail [7] even if the coordination is perfect. The presence of unpaired electron spins, detected in electron spin resonance (ESR) experiments, is the most informative measure of dangling bond defects [8]. A schematic density of states band diagram for an amorphous semiconductor is shown in Fig. 1.1. In the band tails, the electronic states have a localized character, and their nature changes from localized to delocalized at a critical boundary called the mobility edge, as shown in Fig. 1.1, where the mobility gap is the energy difference between the two mobility edges of the conduction and valence bands.

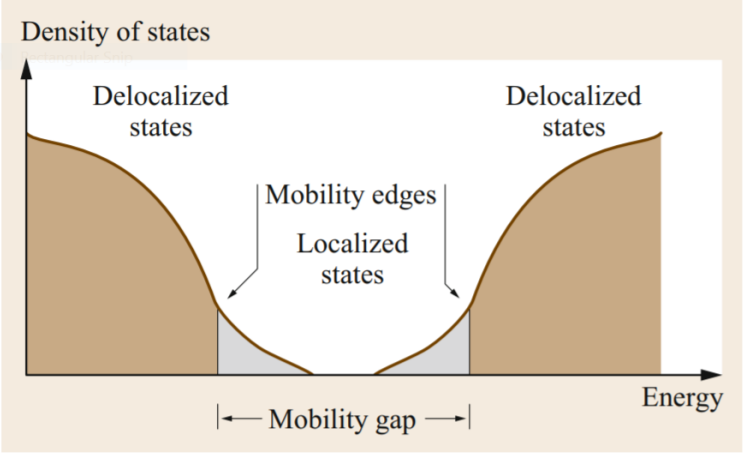

Figure 1.1: Schematic diagram of the density of states of the conduction band and the valence band shown by the brown color. The mobility edge and mobility gab are also shown from Ref. [7].

1.2 Amorphous Silicon

Amorphous silicon (*a*-Si) is a widely studied non-crystalline material [9]. It continues to play a major role in applications ranging from photovoltaic cells, thin-film transistors, electrodes in batteries to the two-qubit quantum logic gates [10–16]. Since the amorphous state of silicon is mainly due to the presence of disorder in the radial and bond-angle distributions, along with a distinctly different topological ordering from its crystalline counterpart, there

are a number of models based on the presence of small clusters of ordered materials as the paracrystalline model [17–19] and the crystalline hypothesis [20]. Despite these, a continuous-random network (CRN) model of Zachariasen [21] is conceptually simple and representative of most of the characteristic properties of *a*-Si and *a*-Si:H as observed in experiments. The structure of *a*-Si can be described fairly accurately by the CRN model and the chemistry of amorphous silicon demands that an ideal CRN model of *a*-Si should satisfy the following properties:

1. every Si atom in the network must be perfectly coordinated, that is, each Si-atom must be bonded to four neighboring Si atoms,

2. the network must exhibit a well-defined short-range order and an intermediate-range order characterized by narrow bond-length and bond-angle distributions,

3. any deviation from the ideal 4-fold coordination of the atoms must be as minimal as possible, preferably 1–100 in 10^5 atoms, so that the resulting electronic, optical, and vibrational properties obtained from a model of *a*-Si must be in agreement with experimental data.

While the structure of *a*-Si can be readily described by using a CRN model, the construction of CRN models with minimal strain and few coordination defects has been a vexing problem in the structural modeling of amorphous silicon. Until recently, high-quality structural models of *a*-Si are best produced by the Monte Carlo based bond-switching algorithm of Wooten, Winer, and Weaire (WWW) [22]. Barkema and Mousseau [23] modified the WWW algorithm for producing large structural models of *a*-Si, exhibiting experimentally compliant structural, electronic and vibrational properties. Other important approaches that are often employed to simulate *a*-Si are molecular-dynamics (MD) simulations [24–29], reverse Monte Carlo simulations (RMC) [30–33], and hybrid RMC methods like hybrid reverse Monte Carlo (HRMC) [34], experimentally constrained molecular relaxation (ECMR) [35], force enhanced atomic refinement (FEAR) [36] and information-driven inverse approach (INDIA) [37, 38].

However, realistic samples of amorphous silicon contain a number of coordination defects. The under-coordinated 3-fold atoms are known as “dangling bonds” and over-coordinated atoms are known as “floating bonds”. Defects in *a*-Si network are broadly characterized as geometrical defects and knowing the properties and abundance of such defects is important, as they can control electronic and other macroscopic properties. In perfectly coordinated amorphous networks, the missing single Si atom in the network is called mono-vacancy and that of two atoms creates divacancy [39]. An extended vacancy or

defect with a relatively larger empty region is called void. The defect density can be reduced via passivation of coordination defects (e.g., dangling bond of Si atom) with hydrogen and the presence of such a small amount of hydrogen in *a*-Si is particularly beneficial for significantly improving photoconductivity in device-grade samples of *a*-Si:H [13].

To study amorphous materials experimentally, we have a variety of characterisation tools including X-ray Absorption Spectroscopy [40], X-ray Diffraction and Fluctuation Contrast Microscopy [18, 41], Rutherford backscattering spectroscopy (RBS) [42], X-ray photoelectron spectroscopy (XPS) [43], scanning tunneling microscopy (STM) [44], ultraviolet photoelectron spectroscopy (UPS) [45], atomic force microscopy (AFM) [46], transmission electron microscope (TEM) [47] and scanning electron microscope (SEM)[48], extended x-ray absorption fine structure (EXAFS) [49], small-angle X-ray scattering (SAXS) [50], Raman scattering [51], infrared absorption (IR) [52, 53] and nuclear magnetic resonance (NMR) [54]. These experiments must be complemented by structural modeling to a detailed understanding of the materials. By performing atomistic structural modeling, a "complete picture" about the materials is anticipated to yield by adding the known facts from experiment to theory. There must be a realistic structural model to make any progress at all on electrons, optical or transport properties of amorphous materials. Therefore, structure determination is an important problem in the field of studying amorphous materials.

1.3 Modeling Methods of Amorphous Solids

Amorphous solids lack long-range ordering and periodicity and these pose one of the greatest challenges to the applications of modeling techniques. Experimental methods cannot at present yield accurate structures at the atomic level: they give averaged structures as in the radial distribution functions (RDFs) provided by diffraction measurements, or very local information as in Extended X-ray Absorption Fine Structure (EXAFS) and Nuclear Magnetic Resonance (NMR) experiments. Computer modeling techniques have, however, the opportunity of yielding detailed models for the structures of amorphous materials at the short and intermediate levels. Several computational methods have been developed for generating models of the structure of amorphous materials at the atomic level like random network models, Monte Carlo (MC), Molecular Dynamics (MD), Reverse Monte Carlo (RMC), and Quantum Mechanical (QM) methods.

The current approaches to structural modeling of *a*-Si can be broadly classified into three categories: simulation paradigm, information paradigm, and hybrid approach. The simulation paradigm comprises a natural approach of traditional computer simulations of molecular dynamics or Monte Carlo techniques with suitable interatomic potentials. The

interactions could be classical empirical [55–57], quantum mechanical (*ab initio* MD) [58], or machine-learning-based [25, 59] potentials. For amorphous and glassy materials, "melt-quench" is the most common simulation technique, where the system is melted at high temperature and then quenched to the desired temperature.

On the other hand, inversion of experimental data is carried out to reconstruct a model of amorphous semiconductors, without any total-energy functional/forces. This technique is generally known as the information paradigm as the different information from the experimental data and/or chemistry of the materials as constraints are used for the reconstruction of a three-dimensional model of amorphous materials. The information paradigm in its purest form produces models reproducing the data using a random process. By including an appropriate number of constraints and diffraction data, a realistic atomistic structure of complex materials can be determined even without using any total energy functional. The reverse Monte Carlo (RMC) [31, 60] and Constraint Monte Carlo (CMC19) [33] are the archetypal examples of the information paradigm.

The hybrid approach is the mixture of information paradigm and simulation paradigm that uses both experimental data inversion and interatomic interaction simulations. In this method, prior knowledge of materials from experiments, often in conjunction with structural and chemical constraints is employed along with an appropriate total-energy functional for the structural determination of complex solids. Some examples of such hybrid schemes are hybrid reverse Monte Carlo (HRMC) [34], experimentally constrained molecular relaxation (ECMR) [35, 61], force enhanced atomic refinement (FEAR) [36], and information-driven inverse approach (INDIA) [38].

Now, we discuss some common structural modeling methods in the following sections.

1.3.1 Continuous Random Networks (CRN)

Zachariasen [21] proposed a continuous random network (CRN), one of the earliest theoretical approaches, to study topologically disordered networks in 1932. The CRN concept is a simplified model to study amorphous semiconductors. The CRN model may not be truly random but also it is certainly *non-crystalline* in nature. The CRN model can be built utilizing values for the bond length and the bond angle from the experimental RDFs. The CRN model should be perfectly coordinated defect-free characterized by having a narrow bond angle distribution, i.e., small distortion in bond angles. For a covalently bonded materials system, coordination satisfies the $8-N$ rule [62], where N is the number of valence electrons. CRN model shows distinct short-range order similar to crystals but lacks the long-range order Early CRN models were studied as physically building of a hand-made

model for a covalently bonded amorphous solids as 'ball-and-stick' arrangement [63, 64], and later in 1976, a computer was used to built CRN models of *a*-Si [65].

1.3.2 Wooten-Weaire-Winer (WWW) Method

In 1985, Wooten, Weaire, and Winer (WWW) introduced a Monte Carlo method for modeling amorphous solids based on a bond-switching algorithm [22]. In WWW method, the starting point is a crystal diamond structure of silicon and has exact 4 neighbors and only six-fold rings exist with periodic boundary conditions. To generate a CRN starting with the diamond crystal, starting crystal is heavily randomized by a large number of bond switches at a temperature, T, that leads to the creation of five-fold and seven-fold rings. After bond switching and rearrangement, the structure is partially relaxed by the use of the Keating potential [55]. Because of the nature of the Keating potential, unphysical short and long bonds will eventually become normal as the simulation proceeds. The final structure is a low strain, defect-free CRN model of amorphous silicon. And later, this method was modified by Mousseau and Barkema for extremely fast computation to generate extremely large and high-quality amorphous silicon [23]. The modified WWW approach can produce a large number of fully coordinated models of *a*-Si, and it is often considered as the benchmark for high-quality *a*-Si models from simulations.

1.3.3 Monte Carlo (MC) Method

Monte Carlo (MC) method is a probabilistic simulation method based on random number generation. In MC simulations, the initial random system hops from one configuration space to another and the "hoping" probability depends on the energy difference between the initial and final configuration as well as the temperature of the system. This sequence of probability distributions satisfying a nonlinear equation can always be interpreted as the distribution of the random states of the Markov chain [66]. MC can search for different trajectories for the system and even jumps over energy barriers. Also, MC methods are useful for computing multi-dimensional integrals that are otherwise difficult to compute analytically. Generally, Monte Carlo is based on the *Markov chain*. In this case, probability of transition follows the Boltzmann distribution given by,

$$P(\Gamma_{old} \to \Gamma_{new}) = \begin{cases} 1 & \text{if } \Delta E < 0 \\ \exp(-\beta \Delta E) & \text{if } \Delta E \geq 0 \end{cases} \tag{1.1}$$

where the energy difference $\Delta E = E(\Gamma_{new}) - E(\Gamma_{old})$, $\beta = \frac{1}{k_B T}$, T is the temperature of the system, and k_B is the Boltzmann constant.

1.3.4 Molecular Dynamics (MD) Simulation Method

Molecular Dynamics (MD) is the time evolution of a system of atoms described by Newton's second law of motion under the influence of temperature. In MD, atoms are represented as point particles with a certain mass, m, and the time evolution of the system is obtained by integrating classical Newton's equations of motion numerically [67]. MD provides a means for dynamical quantities, i.e., time-dependent quantities, and thermal quantities of a system to be computed. Examples of such properties are the rate of diffusion, thermal conductivity of the material, phase transformation in materials, and so on. The evolution of equations of motion for N particle system with position r_i at time t with each mass m_i is given as

$$m_i \frac{d^2 \boldsymbol{r_i}(t)}{dt^2} = -\frac{\partial \Phi(r_1, r_2, ..., r_{3N})}{\partial r_i}. \tag{1.2}$$

So, the important ingredient of MD is the potential that describes the inter-atomic interaction of the system. For amorphous silicon, there exists a range of potentials from highly accurate first principle potential to empirical potentials. Empirical potentials like Keating potential [55] and Stillinger-Weber (SW) potentials [56, 57] estimate the interaction between ions in the system. Empirical potentials are parameter-based potentials, which are simple and computationally cheap, and straightforward to implement. But, in all empirical methods, the forces are purely ionic, and force experienced by an ion i at position r_i is given by,

$$\boldsymbol{F}_i = -\frac{\partial \Phi}{\partial \boldsymbol{r}_i}. \tag{1.3}$$

MD simulations consist of three major steps as (i) initialization of atomic position $\{\boldsymbol{r}_i\}$ and initial velocity $\{\boldsymbol{v}_i\}$; (ii)equilibration of the system over the period of time by solving the equations of motion and (iii) the production of the interested observable quantities. "Melt and Quench" (MQ) is the most common MD method for glassy systems.

1.3.5 Density Functional Theory (DFT)

Density functional theory (DFT) is a first-principle quantum mechanical modeling method to investigate the ground-state electronic structure of many-body systems [68]. The many-body Schrodinger equation that involves full interaction between all the electrons and ions is an almost intractable problem and prohibitively complex [69]. DFT is exact in principle but approximate in practice, and a very successful solution to some aspects of this problem exists. Decoupling of ionic and electronic motion as in the Born-Oppenheimer approximation, a physically observable quantity, i.e., the electron density, $n(r)$, is used to simplify the

complicated many-body equation into a simple one-electron equation which is possible due to a set of theorems by Hohenberg, Kohn, and Sham [70, 71].

Thomas and Fermi were the first to purpose that the total electronic energy of the atom or molecule is a functional of electron density, $n(\boldsymbol{r})$ [72, 73]. The electron-electron interaction energy can be determined from the classical Coulomb potential. Hartree developed a method for calculating the wave function of an atom by introducing the self-consistent field (SCF) approach [74, 75]. Dirac introduced exchange energy for homogeneous electron gas and recast the Hartree-Fock theory in terms of density function [76].

Modern DFT has its root in the two theorems put forward by Hohenberg and Kohn and the tractable equation developed by Kohn and Sham as a practical computational tool. Hohenberg and Kohn showed that a universal functional for the total electronic energy, $E_{tot}[n(r)]$, can be defined in terms of the electron density, $n(r)$, and showed that the total electronic energy and other observable properties are a functional of $n(r)$ and also proved that the input of the exact ground-state electron density into this universal functional yields the global minimum value of this energy functional [70]. Kohn and Sham [71] postulated a form of Schrodinger equation that self-consistently depends on electron density. They invented an indirect approach by assuming a fictitious system of non-interacting particles in an effective potential ($V_{eff}(\boldsymbol{r})$) that generates the same density as any given system of interest of interacting particles in a static external potential [71]. The following single-particle Schrödinger-like Kohn-Sham equation can be obtained by using variational principle with an effective potential.

$$\left[-\frac{1}{2}\nabla^2 + V_{eff}(\boldsymbol{r})\right]\psi_i(\boldsymbol{r}) = \varepsilon_i\psi_i(\boldsymbol{r}) \tag{1.4}$$

where, ψ_i and ε_i are electron orbitals and the corresponding eigenvalues.

The effective potential which contains external potential and exchange-correlation interations is given by,

$$V_{eff}(\boldsymbol{r}) = V_{ext}(\boldsymbol{r}) + \int \frac{n(\boldsymbol{r}')}{|\boldsymbol{r}-\boldsymbol{r}'|}\, d\boldsymbol{r}' + E_{xc}(\boldsymbol{r}) \tag{1.5}$$

with exchange-correlation potential,

$$E_{xc}(\boldsymbol{r}) = \frac{\delta E_{xc} n(\boldsymbol{r})}{\delta n(\boldsymbol{r})} \tag{1.6}$$

Solving self-consistent Kohn-Sham equations iteratively, electronic density of all electronic state are obtained in terms of Kohn-Sham orbitals and the occupation numbers f_i as,

$$n(\boldsymbol{r}) = \sum_{i=1}^{N} f_i |\psi_i(\boldsymbol{r})|^2 \tag{1.7}$$

So, in DFT, the functional constitutes the total energy that is determined from the electron density, which accounts for electron exchange effects coming from Pauli's exclusion principle and electron correlation effects coming from homogenization. However, the exact form of the exchange-correlation function has not been identified, and hence, there are a number of approximations exist to describe the explicit form for the exchange-correlation functional. The most widely used approximations are the local density approximation (LDA) and the generalized gradient approximation (GGA). The LDA is based on the assumption of a locally homogenous system where the exchange-correlation functional depends only on the local value of density $n(\boldsymbol{r})$ [69]. The expression of exchange-correlation E_{xc} can be calculated using local density approximation (LDA) [77] as:

$$E_{xc}^{LDA}[n] = \int n(\boldsymbol{r}) \varepsilon_{xc}[n(\boldsymbol{r})]\, d\boldsymbol{r} \tag{1.8}$$

where, $\varepsilon_{xc}[n(\boldsymbol{r})]$ is the exchange-correlation energy per particle.

For a varying density, generalized gradient approximation (GGA) is used which assumes $\varepsilon_{xc}[n(\boldsymbol{r})]$ is a function of electron density and its gradient at each point [78, 79] given as:

$$E_{xc}^{GGA}[n(\boldsymbol{r})] = \int n(\boldsymbol{r}) \varepsilon_{xc}[n(\boldsymbol{r}), \nabla n(\boldsymbol{r})]\, d\boldsymbol{r} \tag{1.9}$$

In this work, we have extensively used mainly SIESTA (Spanish Initiative for Electronic Simulations with Thousands of Atoms) [80] for *ab initio* Molecular Dynamics (AIMD) and geometry relaxation of the system. SIESTA is a computer program implementation to perform electronic structure calculations and *ab initio* molecular dynamics simulations of molecules and solids. It uses the standard Kohn-Sham self-consistent density functional method in the local density (LDA) and generalized gradient (GGA) approximations [77, 79], as well as in a non-local functional that includes van der Waals interactions (VDW-DF). It uses norm-conserving pseudopotentials in their fully non-local (Kleinman-Bylander) form. Atomic orbitals and their linear combination which include multiple zetas and polarization orbitals are used as a basis set [80]. It projects the electron wavefunctions and density onto a real-space grid in order to calculate the Hartree and exchange-correlation potentials and their matrix elements. It routinely provides total and partial energies, atomic forces, electron density, electric dipole moment, stress tensor, and atomic, orbital, and bond populations. It can also perform structural relaxation, dynamical matrix calculation, phonon (vibrations) calculations and can provide band structure [80].

1.4 Inverting Information: revised Reverse Monte Carlo (RMC) Method

Reverse Monte Carlo (RMC) method is a variation of the standard Metropolis Monte Carlo (MMC) method [14] of structural modeling based on fitting with one or more sets of experimental data [31]. RMC method was developed and extended by McGreevy and Puzstai [31, 60, 81]. The cost function of RMC is given as,

$$\chi^2(\mathbf{R}) = \sum_{i=1} \left[\frac{F_{ex}(q_i) - F_c(q_i;\mathbf{R})}{\sigma(q_i)} \right]^2, \tag{1.10}$$

where $F_c(q;\mathbf{R})$ correspond to simulated diffraction data, either in wavevector space ($q = k$) or in real space ($q = r$), obtained from a distribution of atoms $\mathbf{R}$, $\sigma(q_i)$ is the error associated with experimental data, $F_{ex}(q_i)$. The basic idea is to minimize the cost function value (χ^2), the difference between experiment and model.

The basics of the reverse Monte Carlo (RMC) method can be summarized as [31],

1. Start with an initial random configuration by placing N atoms in a periodic supercell with the consistent density to the experimental data.

2. Compute cost function value χ_0^2 using equation 1.10

3. Choose an atom randomly and move it within the allowed maximum move distance. If any two are closer than the predefined minimum, then reject the move. Choose another at random and again move within the distance until it satisfies the minimum distance condition.

4. Compute the new cost function value of χ_n^2 using equation 1.10 for this new configuration.

5. If $\chi_n^2 < \chi_0^2$, then the move is accepted and the 'new' configuration becomes the 'old' configuration. If $\chi_n^2 > \chi_0^2$ accept with metropolis probability else reject the move.

6. Repeat steps 2-5 until desired convergence is achieved.

Reverse modeling methods provide a platform for the interpretation of experimental information via atomistic modeling. However, reverse modeling methods suffer from the problem of non-uniqueness in the sense that different models will satisfy the same set of experimental data used in the modeling scheme but may entirely fail to match experimental data not used in the scheme [32]. This drawback can be overcome by including several constraints incorporated into the cost function to provide a meaningful chemical

description of the system. The objective function, $\chi^2(\mathbf{R})$, as a multi-objective constraint optimization approach which includes information from experimental diffraction data and a set of structural constraints, can be written as,

$$\chi^2(\mathbf{R}) = \sum_{i=1} \left[\frac{F_{ex}(q_i) - F_c(q_i;\mathbf{R})}{\sigma(q_i)} \right]^2 + \sum_{l=1}^{l_m} \lambda_l C_l(\mathbf{R}), \tag{1.11}$$

where $F_c(q;\mathbf{R})$ correspond to simulated diffraction data, either in wavevector space ($q = k$) or in real space ($q = r$), obtained from a distribution of atoms $\mathbf{R}$, $\sigma(q_i)$ is the error associated with experimental data, $F_{ex}(q_i)$, and C_ls are a set of l_m constraints, providing additional information on the structural properties of the solid. The coefficients λ_l are weights, which determine the relative strength of each constraint in Eq. (1.11).

1.5 Dissertation Outline

The rest of the dissertation is organized in the following way: In Chapter 2, several different descriptors are reviewed to analyze structural, electronic, and phonon properties of amorphous semiconductors from their crystalline counterparts.

In Chapter 3, a subspace optimization technique is introduced that sequentially optimizes two objective functions (involving experimental diffraction data, a total-energy functional, and a few geometric constraints) as an information-driven inverse approach (INDIA). The efficacy of the approach is illustrated by choosing amorphous silicon as an example and shows that it is possible to produce models of amorphous silicon with very little or no coordination defects and an electronic gap around the Fermi level in the electronic spectrum.

A constraint Monte Carlo method is developed for the reconstruction of realistic atomic models of amorphous solids as a multiobjective optimization program that solves the problem accurately using a few structural constraints but no total-energy functionals/forces in Chapter 4. The approach yields highly realistic models of amorphous silicon, with no or only a few coordination defects, a narrow bond-angle distribution, and an electronic gap. This method demonstrates that information-driven inverse approaches not only can enhance existing methodologies for modeling disordered materials, but also offer a directional step-change in materials computation.

In Chapter 5, *ab initio* hydrogen dynamics is studied in nanovoids in amorphous silicon for a varying concentration of hydrogen at low and high temperatures. The dynamics of hydrogen atoms inside the voids are examined with an emphasis on the diffusion of H atoms/molecules and the resulting nanostructural changes of the void surface by using both the local density approximation and the generalized gradient approximation.

In Chapter 6, a force-biased Monte Carlo (FMC) method is developed to model the structure of transition metals cluster (TMC). The structural properties of TMC of iron (Fe), nickel (Ni), and copper (Cu) via FMC and *ab initio* calculations are studied comparatively. Further, *ab initio* molecular dynamics (AIMD), based on density-functional theory (DFT), is carried out to find the putative ground-state structures of 13-atom copper (Cu) and silver (Ag) clusters.

Finally, the entire work is summarized in Chapter 7. Much of the text of the chapters that follow are from my published works cited here: [33, 37, 38, 82–85]

Chapter 2

COMMON DESCRIPTORS OF AMORPHOUS SOLIDS

Amorphous materials are characterized by local atomic environments. This local information can be described mathematically in real space. While the crystalline structure can be uniquely defined by using a unit cell and the periodicity as shown in Fig. 2.1(a), the structure of amorphous solids exhibits a significant variation in the local atomic environment (see Fig. 2.1(b)). Statistical analyses are used to describe the structural properties. The methods to analyze structural, electronic and vibrational properties are presented briefly in the following sections.

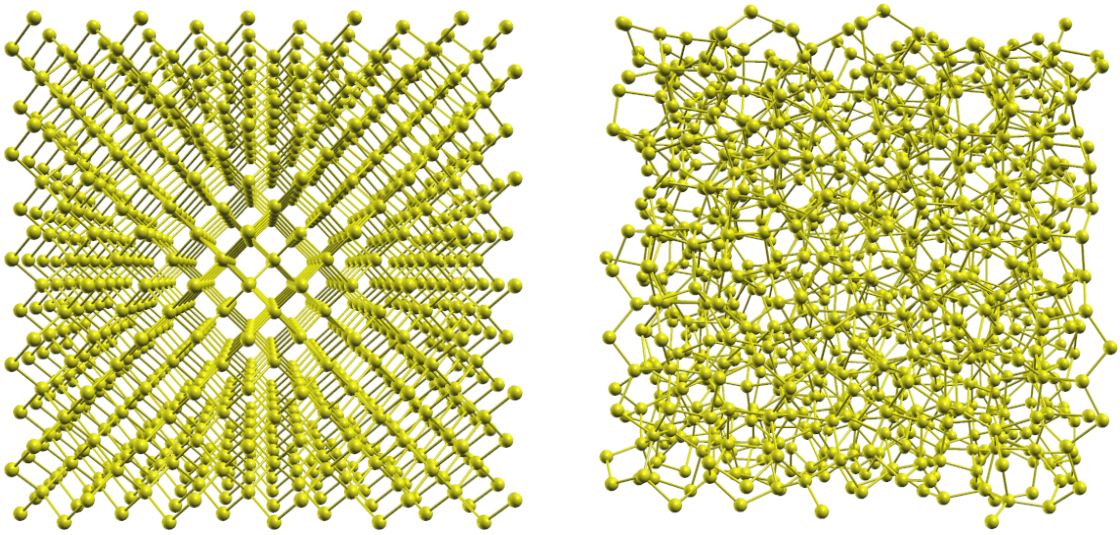

Figure 2.1: (a) Long-range order (LRO) and periodicity exhibited by a 1000-atom model of diamond crystalline silicon. (b) topological disorder exhibited by a 1000-atom model of amorphous silicon.

2.1 Pair Distribution Function

Atomic two-body correlation in the amorphous environment can be best described by the pair correlation function (PCF), which measures the probability of finding an atom at distance $\boldsymbol{r}$ and $\boldsymbol{r}+d\boldsymbol{r}$. For a system of N atoms, it is written as [86]:

$$g(\boldsymbol{r}) = \frac{1}{\rho N} \sum_i \sum_{j \neq i} \delta(\boldsymbol{r} - \boldsymbol{r}_i) \delta(\boldsymbol{r} - \boldsymbol{r}_j) \tag{2.1}$$

where ρ is the number density, given by $\rho = {}^{N}/_{V}$, and V is the volume of the system. Assuming isotropic disordered system and integrating over the angular dependencies θ and ϕ, this results in a purely radially dependent function, $g(r)$, called radial distribution function (RDF), given as [86]

$$g(r) = \int \frac{d\Omega}{4\pi} g(\boldsymbol{r}) = \frac{1}{4\pi\rho r^2 N} \sum_{i \neq j} \delta(r - r_{ij}) \tag{2.2}$$

where r_{ij} is the distance between i-atom and j-atom, i.e., $r_{ij} = |\boldsymbol{r}_i - \boldsymbol{r}_j|$. The RDF is most widely used to describe the structure of amorphous material and can be explained many amorphous structural properties. The position of the first peak and the first minimum in RDF show the average bond length of the atoms in the amorphous system and the first nearest-neighbor cut-off distance. This also shows the degree of short-range order in the amorphous solid. The PCF is shown schematically in Fig 2.2 showing the relationship of PCF to the atomic structure of amorphous material, showing the first peak in $g(r)$ corresponds to the first shell, the second peak to the second shell of atoms, and so on [1].

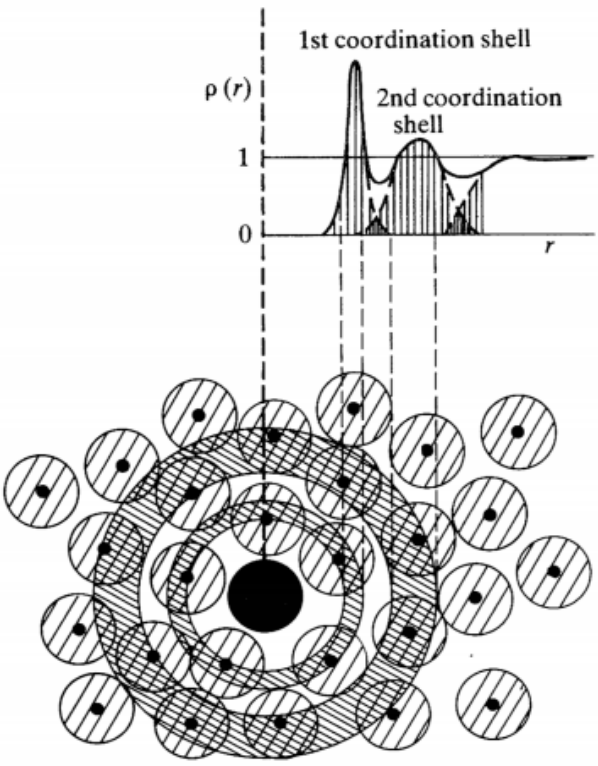

Figure 2.2: A schematic illustration of pair-correlation function and the structural origin of certain features in the density function [1].

The area under a given peak in RDF, $J(r)$, gives the effective coordination number of that particular shell [1] and so the integration over the first peak represents the average coordination number or the number of nearest-neighbor atoms in the first shell.

$$n = \int_0^{r_{cut}} J(r)\, dr \tag{2.3}$$

with,

$$J(r) = 4\pi\rho r^2 g(r) = \frac{1}{N}\sum_{i\neq j}\delta(r - r_{ij}) \tag{2.4}$$

Figure 2.3 shows a comparison of PCFs of computationally generated crystalline and amorphous forms of silicon. The blue curve, labeled *c*-Si, corresponds to crystalline silicon and the red curve, labeled *a*-Si, corresponds to amorphous silicon. The curve for *c*-Si displays sharp peaks over the range shown, corresponding to well-defined shells of neighboring atoms at specific distances, which arise from the long-range regularity of the crystalâĂŹs atomic arrangement. In contrast, *a*-Si exhibits a close-in sharp peak corresponding to the nearest-neighbor atoms, but at longer distances, the undulations in the PCF curve become washed out owing to the absence of the long-range order.

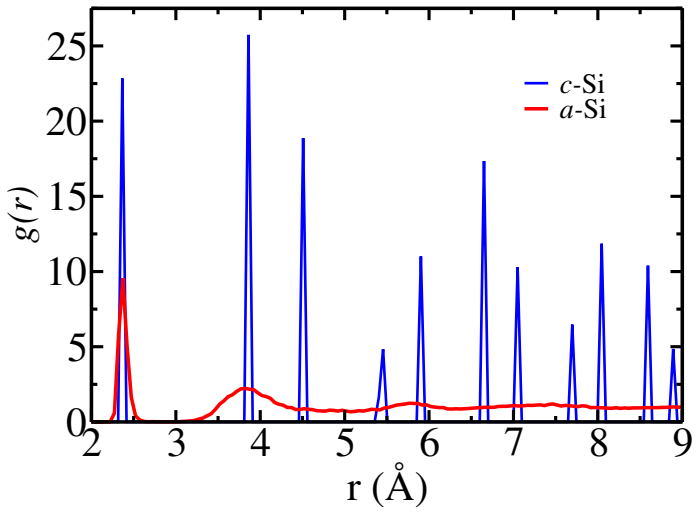

Figure 2.3: The PCF of computer-generated crystalline silicon (blue) and amorphous silicon (red).

2.2 Structure Factor

Experimentally most commonly observed quantity in reciprocal space is the static structure factor (SSF) for amorphous solids which is experimentally obtained by X-ray, neutron, or electron diffraction. A structure factor is a critical tool in the interpretation of scattering

patterns and the internal arrangement of materials obtained in X-ray, neutron, and electron diffraction experiments. This is defined as, [1],

$$S(\boldsymbol{k}) = \frac{1}{N}\left\langle \sum_i \sum_j e^{-i\boldsymbol{k}.(\boldsymbol{r_i}-\boldsymbol{r_j})} \right\rangle, \tag{2.5}$$

where $\boldsymbol{k}$ is the scattering vector. For isotropic system, this can be shown as [1, 87],

$$S(k) = 1 + 4\pi\rho_0 \int_0^\infty r^2 \frac{\sin(kr)}{kr} \left(g(r) - 1\right) dr \tag{2.6}$$

Conversely, the pair correlation function, $g(r)$, can be extracted by Fourier transform of the experimentally measured $S(k)$ as,

$$g(r) = 1 + \frac{1}{2\pi^2\rho_0} \int_0^\infty k^2 \frac{\sin(kr)}{kr} \left(S(k) - 1\right) dk \tag{2.7}$$

It must be noted that PCF and SSF are the one-dimensional representation of a three-dimensional structure and hence the one-dimensional PCF/SSF alone will not be sufficient to fully characterize the information inherent of the amorphous structure of materials, unless other higher degree of correlation.

2.3 Bond-Angle Distribution

It is crucial to analyze higher order of correlation for a realistic model of amorphous materials. For this, the three-body correlation is calculated by calculating the bond angle between three-neighboring atoms, and bond angle distribution (BAD) must exhibit a small value of the deviation of bond angle ($\Delta\theta$). From the knowledge of the position of first and second peaks in RDF, the value for the bond angle is immediately given by, [1]

$$\theta = 2\,\sin^{-1}\left(\frac{r_2}{2r_1}\right) \tag{2.8}$$

where r_1 is the position of the first peak, i.e., the value of the first nearest-neighbor bond length and r_2 is the position of the second peak that gives the second-nearest-neighbor distance.

Additionally, the width of bond angle distribution must be sufficiently narrow so that the system is subjected to minimal structural distortions with a fluctuation in the BAD consistent with the value estimated from Raman spectroscopy [2] for amorphous materials.

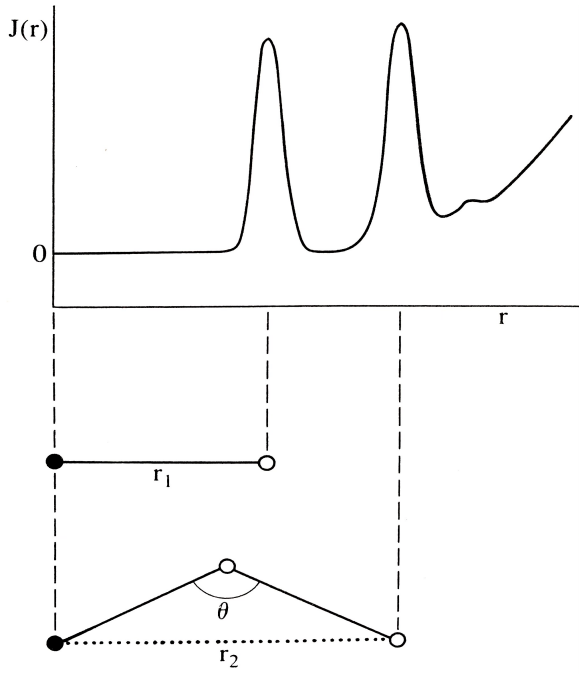

Figure 2.4: A schematic illustration of the first and second neighbor bond lengths, r_1 and r_2, and their relation to the bond angle θ from the first two peaks in RDF from Ref. [1].

2.4 Ring Statistics

A closed irreversible path or loop that starts and ends at the same atomic site of topological networks is called rings. The connectivity of atoms in amorphous networks can be analyzed by computing the statistics of irreducible rings of varying sizes. Here, irreducibility implies that the ring cannot be further partitioned into rings of smaller/equal size by topologically deforming the original ring in the space of the embedding dimension [88, 89]. For this, it must be counted only minimal rings, i.e., closed paths of some number of bonded atoms for which there is no other path between any pair of atoms in the ring which has fewer bonds than the shorter path between them along the ring. As in Fig. 2.5, the path *a-b-c-d-e-f-a* is a closed path that contains six bonded atoms but this could not be an irreducible ring as there exists a shorter path from *c*-to-*f* through atom *g*. Therefore, the figure does not show a 6-membered ring, but two 5-membered rings.

By examining the topological connectivity of the networks as irreducible rings of various sizes, for the given local tetrahedral character of the network, the distribution of $n-$member rings ($n \geq 4$) provides some information about the atomistic structure on the medium-range length scale and the presence of high-member rings ($\geq$ 7-member) can be indicative of the presence of intermediate-range order (IRO) in amorphous networks.

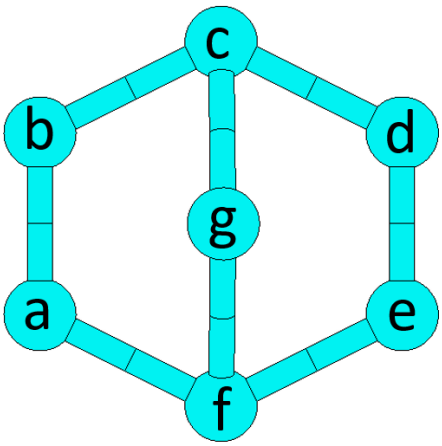

Figure 2.5: A schematic diagram of a irreduble 5-membered ring.

2.5 Electronic Structure

While structural properties of amorphous model networks provide a wealth of atomistic information, the most compelling evidence of the atomistic realistic model comes from its ability to produce the correct electronic properties. In amorphous solids, the wave-function of electrons lacks the periodicity and does not allow to express of wave-function in terms of Block waves as in crystal [1]. So, the electronic structure in amorphous solids is described by the electronic density of states (EDOS). It provides information about the electronic gap and electronic quality of the materials. The structural defect and topological irregularities in the system lead to spatially localized electronic states near the tails of the band-gap. In particular, we carry out density functional theory (DFT) based calculations and use the Kohn-Sham eigenvalues to describe the EDOS defined below [69],

$$D(E) = \frac{1}{N}\sum_{i=1}^{N}\delta(E - E_i), \tag{2.9}$$

where N is the size of the basis set, E_i is the ith eigenvector and $D(E)$ is the electronic density of states.

2.6 Vibrational Properties and Specific Heat Capacity

Both in the case of crystalline and amorphous solids, atomic vibrations are quite important in many ways as they determine the thermal properties of the materials. Like in crystal, heat is transported via vibrational excitements and even the specific heat capacity of the amorphous solids is calculated by the spectrum of allowed vibrational mode [1].

The calculation of vibrational density of states (VDOS) is carried out in the harmonic approximation by diagonalization of the dynamical matrix, which is obtained from a well-relaxed system. The dynamical matrix is given by the relation [90, 91],

$$\mathcal{D}_{I_\alpha, J_\beta} = \frac{1}{\sqrt{M_I M_J}} \frac{F_{J_\beta}}{\Delta x_{I_\alpha}}. \tag{2.10}$$

where M's are the ionic masses of the atoms, and α and β are the Cartesian coordinates of atoms I and J, respectively. To construct a matrix element, each atom is displaced in 6-directions ($\pm$x, $\pm$y, $\pm$z) with a small displacement Δx_{I_α} and an *ab initio* force calculation is performed to obtain the force constant matrix resulting due to displacement of each atom from it's equilibrium position. For a given atom, there are $3N$ matrix elements, and this implies that the dimension of $\mathcal{D}$ is $3N \times 3N$. Since the vibrational modes are the eigenstates of dynamical matrix $\mathcal{D}$, the eigenvalue problem is solved to get the eigenvalues of $\mathcal{D}$ as $\{\omega_i^2 : i = 1, 2, ..., 3N\}$.

If ω is the frequency of vibration, then $g(\omega)d\omega$ is the number of modes within the interval $[\omega, \omega + d\omega]$, where $g(\omega)$ denotes the VDOS of the system. The VDOS, of an amorphous system with N atoms, is defined as

$$g(\omega) = \frac{1}{3N} \sum_{i=1}^{N} \delta(\omega - \omega_i), \tag{2.11}$$

With the known values of the density of states, $g(\omega)$, the evaluation of the specific heat within the harmonic approximation is straightforward and it is calculated from the (discrete) vibrational frequencies (ω) obtained from direct diagonalization of the dynamical matrices in the harmonic approximation using the relation, [92]

$$C_v(T) = k_B \sum_{\boldsymbol{k}, i} \frac{(\frac{\hbar\omega_i(\boldsymbol{k})}{2k_BT})^2}{\sinh^2(\frac{\hbar\omega_i(\boldsymbol{k})}{2k_BT})}, \tag{2.12}$$

Chapter 3

INFORMATION-DRIVEN INVERSE APPROACH

The work presented in this chapter has been published in (i) **Limbu, D. K., Atta-Fynn, R., Drabold, D. A., Elliott, S. R. & Biswas, P. Information-driven inverse approach to disordered solids: Applications to amorphous silicon.** *Physical Review Materials* **2,** 115602 (2018), and (ii) **Limbu, D. K., Atta-Fynn, R. & Biswas, P. Atomistic simulation of nearly defect-free models of amorphous silicon: An information-based approach.** *MRS Advances* **4,** 87–93 (2019).

3.1 Introduction

The reconstruction of three-dimensional models of complex non-crystalline solids from experimental data constitutes an archetypal example of inverse problems in materials modeling. Inverse approaches provide a distinct route to design complex disordered materials by directly incorporating a set of experimental observables in simulation methodologies. The resulting atomistic models thus exhibit a high degree of compliance with a set of experimental data, and the method, by construction, eliminates the need for accurate total-energy functionals, which are necessary for conventional simulations. A classic example is the Reverse Monte Carlo (RMC) method,[30–32, 60, 93] which attempts to construct a three-dimensional model of disordered solids by inverting experimental diffraction data in conjunction with a few structural constraints. However, the difficulty associated with inverting one-dimensional pair-correlation diffraction data in the presence of competing structural constraints, which leads to a difficult non-convex optimization problem, has been a major obstacle in producing realistic structural solutions from RMC simulations. Although the method has been employed for a variety of disordered solids,[31] the problem is particularly acute for highly-coordinated systems, such as amorphous silicon (*a*-Si) and tetrahedral amorphous carbon (*ta*-C). To our knowledge, none of the RMC-derived models of *a*-Si reported in the literature [30–32, 60, 93] to date exhibits a clean gap in the electronic density of states around the Fermi level and a low defect density as observed in electron spin resonance (ESR) experiments.[94]

Inverse problems are often characterized by their ill-conditioned nature and they are notoriously difficult to solve satisfactorily. [95] In the context of materials modeling, the

difficulty primarily arises from the volume of structural (and additional) information to be incorporated in the problem by constructing suitable penalty/constraint functions and the subsequent optimization of an objective function (involving experimental data and constraint functions) in a high-dimensional solution space. The presence of hierarchy among higher-order correlation functions[96, 97] suggests that a minimal number of constraints and experimental data sets need to be included in the problem in order to produce structurally unique models. However, the inclusion of too much information can make very difficult the resulting non-convex optimization problem and its accurate solution that satisfies the requirements of a physical model.

An approximate solution of the constrained RMC problem for *a*-Si was proposed by some of us more than a decade ago.[32] While this approach produced correctly the two- and three-body atomic correlation functions, as well as a reasonably good electronic density of states (EDOS) with a hint of a spectral gap in the vicinity of the Fermi level, the presence of a significant number of coordination defects (e.g., 3- and 5-fold coordinated atoms) limits the applicability of the method and the resulting models for high-quality predictive studies of amorphous silicon. Although a number of hybrid methods,[35, 36, 61, 98–101] i.e., methods that involve a total-energy functional in RMC simulations in addition to scattering data, have been developed in the last decade to produce improved structural models of *a*-Si, none of the methods lead to atomistic models that can match the high quality of the bond-switching Wooten-Winer-Weaire (WWW) models.[22, 23, 102] The purpose of this chapter is to present an information-driven inverse approach (INDIA), combining experimental data and constraint information with a total-energy functional to yield high-quality atomistic models of amorphous silicon. We demonstrate that the resulting structural models produce a clean gap in the electronic density of states around the Fermi level with a few coordination defects. The atomistic models from the new approach represent the very best of its class and they are comparable to those obtained from the WWW method.

In recent years, information-based approaches have played a crucial role in designing complex materials.[35, 36, 61, 98, 101, 103–105] Molecular-dynamics (MD) simulations, using knowledge-based interactions obtained via machine-learning algorithms, have been employed to produce high-quality MD models of *a*-Si.[25] Likewise, experimental data from nuclear magnetic resonance and infrared spectroscopy have been employed profitably to understand the microstructure of hydrogen in *a*-Si:H and the distribution of extended inhomogeneities (e.g., voids) in *a*-Si.[106–109] Electronic information too, from electronic densities of states, has been used in an effort to control and engineer the band gap of *a*-Si using constrained molecular-dynamics simulations.[110] Thus, the incorporation of relevant structural,[32] electronic,[110] NMR,[108] and IR[111] information played a decisive role

in simulations, not only to develop better structural models but also to understand physical properties of the amorphous state that were not accessible from using conventional atomistic simulations. This observation also applies to the WWW method. An examination of the latter suggests that the so-called WWW bond switches essentially introduce 5-member and 7-member rings in crystalline or disordered silicon networks while maintaining four-fold coordination for each atom, which are followed by total-energy optimization to obtain stable local minima on the potential-energy surface (PES). Thus, the application of bond switches in the WWW method can be viewed as an inclusion of topological information (i.e., 5- and 7-member rings) in simulations that greatly facilitates the system to explore the relevant region of the PES consistent with the induced ring topology and four-fold coordination and to determine amorphous configurations of silicon in the resulting procedure.

The rest of the chapter is as follows. In Sec. 3.2, we present an information-driven inverse approach (INDIA) that entails optimization of an augmented objective function, incorporating experimental diffraction data, a few structural constraints, and a total-energy functional. We show that the difficulty associated with the optimization of the augmented objective function can be considerably reduced by introducing a subspace optimization technique, which sequentially optimizes total-energy and experimental diffraction data (including a few geometrical constraints) in a self-consistent manner to determine optimal structural solutions, satisfying experiments and a total-energy functional simultaneously. Section 3.3 discusses the results from the simulations by examining structural, electronic, and vibrational properties of the resultant *a*-Si models. A comparison of the results with experimental data and those from the WWW and high-quality molecular-dynamics models[24, 25] of identical size from the literature are also presented here. This is followed by conclusions in Sec. 3.4.

3.2 Computational Method

In conventional RMC simulations, one attempts to invert a set of experimental diffraction data, $F_{ex}(k)$, by writing an objective function, [30, 31, 60]

$$\chi^2(\mathbf{R}) = \sum_i \left[\frac{F_{ex}(k_i) - F_c(k_i;\mathbf{R})}{\sigma(k_i)} \right]^2 + \sum_l \lambda_l C_l(\mathbf{R}), \tag{3.1}$$

where $F_c(k;\mathbf{R})$ correspond to simulated diffraction data obtained from a three-dimensional distribution of atoms $\mathbf{R}$, $\sigma(k_i)$ is the error associated with $F_{ex}(k_i)$, and C_l are a number of structural constraints, providing additional information on the atomistic properties of the solid. The coefficients λ_l are weights associated with C_l, which determine the relative strength of the constraints in simulations. While Eq. (3.1) appears to present a well-posed

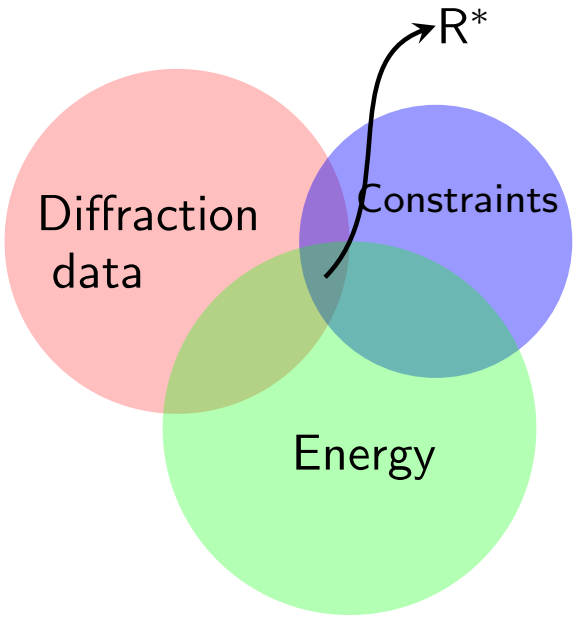

Figure 3.1: A schematic illustration of the augmented space, $\mathcal{P}$, consisting of the objective-function spaces spanned by the experimental data (red), constraint information (blue), and a total-energy functional (green). An optimal structural solution, $\mathbf{R}^*$, corresponds to the region of intersection of the three circles.

inverse problem [112] for structural determination of a solid, a direct determination of an *accurate* optimal physical solution of the resulting non-convex optimization problem has proven to be too difficult to obtain, owing to the high dimensionality of the search space and the presence of competing constraints in Eq. (3.1). The phrase 'well-posed' is used here in a Hadamard sense. Following Hadamard,[112] a problem is 'well-posed' if a mathematical model of the physical problem has the properties of uniqueness, existence, and stability of the solution. In the present context, assuming that the first two properties are satisfied in the presence of structural constraints, it is not evident that the solution (of Eq. 3.1) continuously depends upon experimental data and constraint information. By including additional *a priori* information, it is often possible to augment the solution space and improve the smoothness and stability of the solution with respect to input data. The present study is a case in point. The information-driven strategy adopted here relies on the following two observations: (a) an optimal structural solution should originate from the region of the solution space that simultaneously satisfies a set of experimental data and a total-energy functional; (b) the solution must represent a good local minimum on the potential-energy surface and that it ought to be consistent with the structural constraints included in Eq. (3.1) (see Fig. 3.1). Toward this end, we form an augmented objective function $\mathcal{P}(E,\mathbf{R})$, which is the direct

product of a total-energy functional $E(\mathbf{R})$ and the function χ^2 in Eq. (3.1),

$$\begin{aligned}
\mathcal{P} &\equiv E(\mathbf{R}) \otimes \chi^2(\mathbf{R}) \\
&\equiv E(\mathbf{R}) \otimes \left[\sum_i \left(\frac{F_{ex}(k_i) - F_c(k_i;\mathbf{R})}{\sigma(k_i)} \right)^2 + \sum_l \lambda_l C_l(\mathbf{R}) \right] \\
&\equiv \left[E(\mathbf{R}) \otimes \sum_i \left(\frac{F_{ex}(k_i) - F_c(k_i;\mathbf{R})}{\sigma(k_i)} \right)^2 \right] \\
&\qquad \oplus \left[E(\mathbf{R}) \otimes \sum_l \lambda_l C_l(\mathbf{R}) \right] \\
&\equiv \chi^2_M \oplus \chi^2_K. \qquad (3.2)
\end{aligned}$$

In Eq. (3.2), χ_M is the objective function in subspace $\mathcal{M}$, spanned by the total-energy functional and experimental diffraction data. A similar definition applies to χ_K in subspace $\mathcal{K}$, where experimental diffraction data are replaced by a set of structural constraints. Here, we are optimizing the values of χ_M and χ_K by varying $\mathbf{R}$, and $\mathcal{M}$ and $\mathcal{K}$ denote the set of all possible values χ_M and χ_K, respectively, obtained via the mapping $f : \mathbf{R} \to \mathcal{X}$. The map f is defined by Eq. 3.2 and the objective functions χ_M and χ_K are two-dimensional vectors or 2-tuple objects in the subspaces $\mathcal{M}$ and $\mathcal{K}$, respectively. The symbols $\otimes$ and $\oplus$ stand for the operation of direct product and direct sum between the subspaces that form the augmented objective function space $\mathcal{P}$. A schematic illustration of these regions and their relationship to $\mathcal{P}$ is shown in Fig. 3.1. All optimal structural solutions correspond to the region of intersection between the subspaces via the mapping, $f : \mathbf{R} \to \mathcal{P}$. We emphasize that, while several optimal solutions might exist that can differ from each other microscopically, it is necessary that they are macroscopically similar in order to be considered as correct physical solutions of the problem. In the following, we provide an ansatz to obtain optimal structural solutions, $\mathbf{R}^*$ that simultaneously satisfy the objective functions χ_M and χ_K in subspaces $\mathcal{M}$ and $\mathcal{K}$, respectively. The procedure for determining an optimal solution in $\mathbf{R}$, by jointly optimizing χ_M and χ_K, consists of the following steps:

(1) Start with a random distribution of atoms and optimize the objective function χ_M to fit experimental diffraction data and a total-energy functional in $\mathcal{M}$. This is achieved by conducting a reverse Monte Carlo simulation to fit the diffraction data and minimizing the total potential energy via the Conjugate-Gradient (CG) or an appropriate method in a self-consistent manner. We refer to this step as the M loop (see Fig. 3.2). The convergence of this self-consistent loop is obtained by specifying a maximum value of M and tolerance values for RMC fitting and total-energy relaxations.

(2) The structural solution $\mathbf{R}_M^*$, obtained on successful completion of step 1, is subjected to further treatment so that the objective function χ_K, involving a coordination constraint $C_l(\mathbf{R})$ and a total-energy functional $E(\mathbf{R})$, is now optimized. The constraint function, $C_l(\mathbf{R})$, corresponds to the square of the deviation of the average coordination, $n_l(\mathbf{R})$, from an ideal target value of n_0. Here, we have used the following functional form of $C_l(\mathbf{R})$,

$$C_l(\mathbf{R}) = \sum_l \left(1 - \frac{n_l(\mathbf{R})}{n_0}\right)^2$$

A value of λ_l = 1 to 5 and n_0 = 4 have been observed to work well in our work. The optimization is performed as before for fitting a coordinate-constraint function using a second RMC simulation and total-energy optimization via CG relaxations or a suitable scheme. The step is indicated as the K loop in Fig. 3.2 and the convergence is handled in a similar manner by specifying tolerance values for atomic coordination and total energy;

(3) To ensure that the final solution satisfies both the objective functions χ_M and χ_K, a coupling is established between $\mathcal{M}$ and $\mathcal{K}$ so that the resulting output, $\mathbf{R}_K^*$, from step 2, can be fed back to the M loop to achieve self-consistency between $\mathbf{R}_M^*$ and $\mathbf{R}_K^*$, using suitable convergence criteria. The latter involves specification of a coordination-defect density, a root-mean-square deviation of the bond-angle distribution, and a goodness-of-fit of the diffraction data in RMC simulations within the feedback loop (via a green diamond), which determine the final converged solution $\mathbf{R}^*$. In the event that a converged solution cannot be obtained for a given number of iterations, the program can either continue by generating a new random configuration or exit the loop prematurely with the current solution.

A flowchart of the optimization program is shown in Fig. 3.2. The subspace optimizations of χ_M and χ_K are indicated in the flowchart as shaded regions in light red and light blue colors, respectively. The two regions are connected by a feedback loop through a green diamond in Fig. 3.2 in order to achieve a self-consistent solution in subspaces χ_M and χ_K.

For total-energy optimizations, one can choose an appropriate classical, semiclassical, or quantum-mechanical force field, depending upon the complexity of the problem to be addressed. Here, we have employed the modified Stillinger-Weber (SW) potential, [56, 57]

$$E(\mathbf{R}) = \frac{1}{2}\sum_{i=1}^{N}\sum_{\substack{j=1\\(j\neq i)}}^{N} v_2(r_{ij}) + \sum_{i=1}^{N}\sum_{\substack{j=1\\(j\neq i)}}^{N}\sum_{\substack{k=1\\(k\neq i)\\(k>j)}}^{N} v_3(\boldsymbol{r}_{ij}, \boldsymbol{r}_{ik}), \tag{3.3}$$

where v_2 and v_3 are the two-body and three-body contributions to the total potential energy,

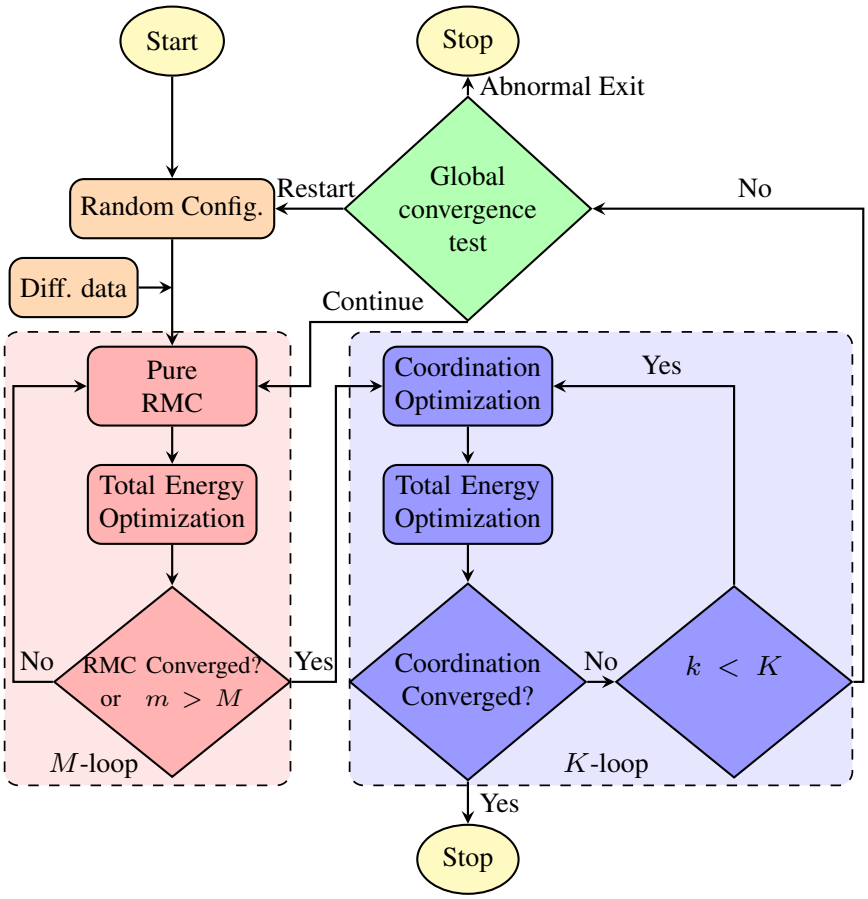

Figure 3.2: A flowchart showing information flow during simulations. The subspace coupling between the M loop and K loop reduces the computational complexity of the optimization problem and leads to the generation of nearly defect-free configurations of amorphous silicon.

respectively, and they are given by,

$$v_2 = \begin{cases} \varepsilon A \left[B \left(\frac{r_{ij}}{\sigma} \right)^{-p} - 1 \right] e^{\left(\frac{\sigma}{r_{ij} - a\sigma} \right)}, & \text{if } r_{ij} < a\sigma \\ 0, & \text{otherwise} \end{cases}$$

and

$$v_3 = \begin{cases} \varepsilon\lambda \left(\cos\theta_{jik} + \frac{1}{3} \right)^2 e^{\left(\frac{\sigma\gamma}{r_{ij} - a\sigma} + \frac{\sigma\gamma}{r_{ik} - a\sigma} \right)}, & \text{if } r_{ij}, r_{ik} < a\sigma \\ 0. & \text{otherwise} \end{cases}$$

In Eq. (3.3), r_{ij} is the distance between two atoms at sites i and j, and θ_{jik} is the angle subtended at site i by the vectors $\mathbf{r}_{ij}$ and $\mathbf{r}_{ik}$. We employed the modified SW potential parameters from Ref. [57], which are listed in Table 3.1. Throughout the work, we have

used the experimental density of *a*-Si of 2.25 g/cm^3 and a maximum value of M=200 and K=1000 for achieving self-consistency within the M loop and K loop, respectively. To compute the electronic and vibrational properties of the optimal structural configuration, we have used the first-principles density-functional code SIESTA[80, 113] to thoroughly relax the final INDIA structures using fully self-consistent field calculations. SIESTA employs local basis functions, based on numerical pseudoatomic orbitals, and norm-conserving Troullier-Martins pseudopotentials [114] to solve the Kohn-Sham equations self-consistently within the framework of density functional theory. In this work, we employed double-zeta basis functions and the electronic correlations were handled using the generalized gradient approximation (GGA), via the Perdew-Burke-Ernzerhof (PBE) [79] formulation.

Table 3.1: Modified Stillinger-Weber (SW) potential parameters [57]

ε (eV)	λ	σ (Å)	γ	A	B	a	p
1.64833	31.5	2.0951	1.20	7.049556277	0.6022245584	1.80	4

3.3 Results and Discussions

Since the structural quality of *a*-Si networks is largely determined by the two- and three-body correlation functions, along with the concentration of dangling and floating bonds (i.e., threefold- and fivefold-coordinated atoms, respectively), we begin by examining the radial and angular correlations between atoms in the models. Noting that the method, by construction, incorporates structural information at the two-body level in real/reciprocal space, we shall focus our attention on network properties that involve higher-order correlation functions, such as the bond-angle distribution (BAD) and dihedral-angle distribution (DAD), statistics of the ring-size distribution, and the local coordinations of atoms in the networks. These will be followed by an analysis of electronic and vibrational properties of the models. Below, we discuss the results from four INDIA models of size 216, 300, 512, and 1024 atoms, each averaged over three independent configurations, and provide comparisons with the corresponding WWW and MD models, as well as experimental data from *as-deposited* *a*-Si samples. For comparison, we generated a set of MD models, using the modified SW potential, following the methodology described in Ref. [24] and refer to those as SW-MD models. Likewise, the WWW models were constructed using the modified bond-switching WWW algorithm of Barkema and Mousseau. [23] In addition, we have also compared our results with a 512-atom model by Deringer *et al.* [25], from using machine-learning-driven

MD simulations (ML-MD), 216- and 512-, and 1024-atom models by Pandey *et al.* [98] and Igram *et al.* [101], respectively, from using the Force Enhanced Atomic Relaxation (FEAR) approach.

3.3.1 Structural Properties

Figure 3.3 shows the reduced pair-correlation function (PCF), $G(r)$, and the corresponding structure factor (SF), $S(k)$, for the 512-atom INDIA and WWW models. Experimental data from *as-deposited* samples [115] of *a*-Si are also shown in the plot for comparison. Although the results, in particular the simulated structure-factor data, are expected to match with experiments accurately, it is important to examine the PCF and structure factor closely due to the complementary nature of these (primal and dual) quantities in expressing atomic pair correlations. While a PCF expresses local (two-body) correlations explicitly, its Fourier counterpart provides an overall match (of two-body correlations) incorporating information from all length scales. This is reflected in the first sharp diffraction peaks (FSDP) in Fig. 3.3(b): the presence of small deviations in $G(r)$ beyond 5.0 Å appears to be translated into a small but visible difference in the height of the FSDPs (see inset in Fig. 3.3(b)). To examine the interstitial volumes associated with the model networks, we computed the Voronoi volumes (of the atoms) of the 512-atom INDIA, WWW and SW-MD models and plotted the respective Voronoi-volume distributions in Fig. 3.3(c). The following observations are now in order. First, the Voronoi-volume distribution of a model can provide additional information on the degree of local ordering of a disordered network in a manner similar to the pair-correlation and bond-angle distributions. A narrow distribution with a sharp peak is indicative of more ordered networks, whereas networks with less order tend to show a relatively broad distribution. Second, since the Voronoi volume associated with an atom depends on the spatial positions of its nearest neighbors, the degree of inhomogeneity of a disordered network can be approximately gauged by analyzing the volume distribution, particularly the region away from the central peak. A large (or small) Voronoi volume is indicative of the presence of sparse (or dense) atomic environment in the network. It may be noted that the Voronoi volume associated with an atom having a low-coordination number (≤ 3 for *a*-Si) may not be well-defined depending upon the angles subtended by its neighbors at its center. The presence of large bond angles can make the Voronoi volume abnormally large or ill-defined, and the Voronoi partition of such three-dimensional networks may not be possible for the *given* nearest-neighbor list. In the present case, the Voronoi volumes of few 3-fold-coordinated atoms have been replaced by the average Voronoi volume/atom, derived from the 4-fold-coordinated atoms in the network. Thus, the presence of microvoids

and the density-deficient regions in the network can be readily manifested in the Voronoi-volume distribution. It is apparent from Fig. 3.3(c) that, as far as the Voronoi volumes or the interstitial regions of the atoms are concerned, the SW-MD models exhibit more order than the corresponding WWW and INDIA models. This observation is quite consistent with the fact that MD models generally represent annealed samples of *a*-Si more closely, and hence more ordered, than those obtained from the relaxation-based Monte Carlo or similar approaches.

The hierarchy among atomic-correlation functions implies that the one-dimensional PCF/SF alone cannot fully characterize a three-dimensional model of *a*-Si, unless the PCF/SF is also consistent with, at the very least, the bond-angle distribution (BAD) $B(\theta)$, and its width. Additionally, the latter must be sufficiently narrow so that the network is subjected to minimal structural distortions with a fluctuation in the BAD consistent with the value estimated from Raman spectroscopy [2]. These considerations lead to the conclusion that the root-mean-square (RMS) deviation or fluctuation of the bond-angle distribution of a high-quality *a*-Si network should not exceed 9°–11°. Figure 3.4 shows the bond-angle distributions for 512-atom INDIA and WWW models. The BADs from the INDIA and WWW models closely match each other, with an average bond angle of $109.1^\circ \pm 10.6^\circ$ (INDIA) and $109.1^\circ \pm 10.5^\circ$ (WWW), obtained from a Gaussian approximation to the shape of the respective BADs. A comparison of structural properties of the models in Table 3.2, obtained from a range of simulation techniques, establishes that the INDIA methodology has the ability to yield *a*-Si models par excellence. Thus, it would not be inappropriate to conclude that the INDIA models presented here are significantly better than earlier RMC models [30,32] and their hybrid counterparts [36,98,101,116] and that they are on a par with the models obtained from the WWW method and recent high-quality molecular-dynamics simulations [24,25] of amorphous silicon.

Table 3.2 summarizes some key structural properties of *a*-Si models obtained from MD simulations and total-energy-based relaxation methods that are particularly useful for direct comparison. Recognizing that the structural quality of *a*-Si models is chiefly determined by the PCF, the BAD and its width, and the concentration of coordination defects in the networks and that the FEAR and INDIA methods essentially belong to the same universality class (in the sense that they both rely on the information paradigm), it is evident from Table 3.2 that the latter consistently produces *a*-Si models with a smaller bond-angle width and fewer coordination defects than the FEAR. This observation is indicative of the electronic quality of the models too. We shall see later that, unlike the FEAR models (see Refs. [36,101]), the INDIA models produce a pristine gap around the Fermi level. Further, we shall demonstrate that the size of the electronic gaps obtained from the INDIA models is

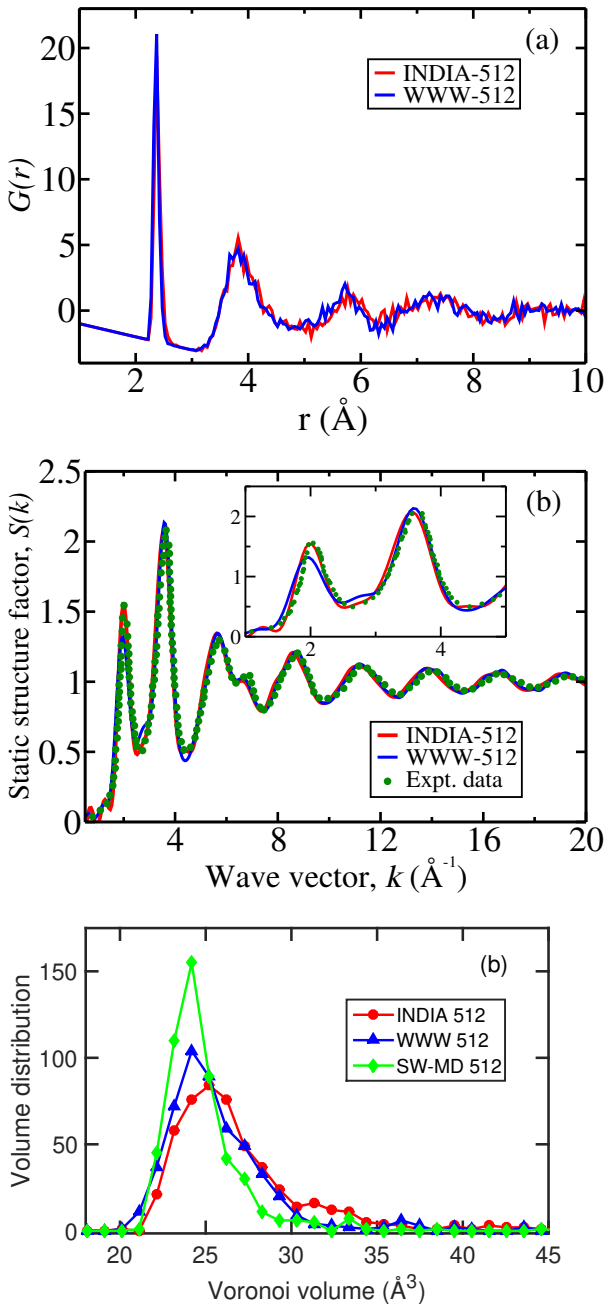

Figure 3.3: (a) The reduced pair-correlation functions $G(r)$ of *a*-Si from INDIA (red) and WWW (blue) models of size 512 atoms. (b) The corresponding static structure factors $S(k)$ from the INDIA (red) and WWW (blue) models. Experimental data for *as-deposited a*-Si samples (green) are included from Ref. [115]. An enlarged view of the first two peaks of the structure factors is shown in the inset for a close comparison of the results. (c) The (approximate) distributions of Voronoi volumes obtained from the INDIA (red), WWW (blue) and SW-MD (green) models.

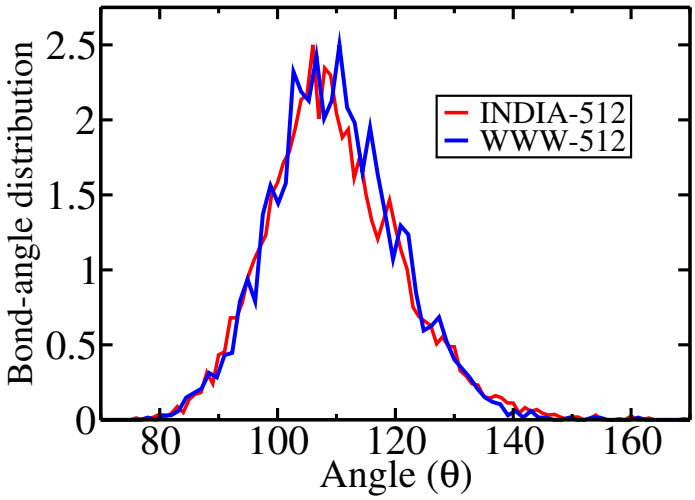

Figure 3.4: The bond-angle distributions $B(\theta)$ of a-Si from 512-atom INDIA (red) and WWW (blue) models. The average bond angles and the corresponding root-mean-square deviations are given by $109.1^\circ \pm 11.5^\circ$(INDIA) and $109.1^\circ \pm 10.7^\circ$(WWW).

comparable with those from the WWW models, as far as the models with 216, 300, and 512 atoms are concerned.

In Table 3.2, we have listed the value of $\Delta E = E(N) - E_c$, where $E(N)$ and E_c correspond to the energy per atom for *ab initio*-relaxed configurations of a-Si containing N atoms and a crystalline network of silicon comprising 1000 atoms, respectively. The value of E_c has been found to be practically independent of N for $N \geq 512$. Here, ΔE is associated with the heat of crystallization of a-Si and has been obtained from differential scanning calorimetry by Roorda *et al.* [117] and Rutherford backscattering and channeling, coupled with differential scanning calorimetry, by Donovan *et al.* [118]. For annealed (at 500 °C) and as-implanted samples of a-Si, the values of ΔE have been determined by Roorda *et al.* to be 13.7 $\pm$ 0.7 kJ/mol and 18.8 $\pm$ 1.0 kJ/mol, respectively. These values correspond to the range of 0.135–0.205 eV/atom. Likewise, Donovan *et al.* have reported a value of the heat of crystallization to be 11.9 $\pm$ 0.7 kJ/mol or 0.116–0.131 eV/atom. Thus, the experimental value of the heat of crystallization matches quite closely with the computed values from the INDIA and SW-MD models

Probing higher-order correlations between atoms proves to be rather difficult due to the high-dimensional nature of information involving four or more atoms. The distribution of angles between two dihedral planes provides limited information about four-body correlations but it is useful to examine this correlation as an independent check for added credibility. Figure 3.5 shows the distribution of dihedral angle for two 512-atom INDIA and WWW models. The presence of a characteristic maximum at 60° and a minimum at 120°

Table 3.2: Structural properties of *ab initio*-relaxed INDIA, MD, and WWW models. $\langle r \rangle$, $\langle \theta \rangle$, $\Delta\theta(\Delta\theta_G)$ and C_n represent average bond length, the average bond angles, RMS deviations, and the percentage of n-fold coordinated atoms, respectively. ΔE is the relative energy difference (in eV) per atom from a 1000-atom crystalline silicon configuration and it is related to heat of crystallization.

Model	N	$\langle r \rangle$	$\langle \theta \rangle$	$\Delta\theta(\Delta\theta_G)^*$	C_4	$C_3 + C_5$	ΔE
INDIA	216	2.391	109.10	11.8 (11.3)	99.08	0.46+0.46	0.232
SW-MD		2.383	109.32	8.8 (8.4)	100.0	0.0+0.0	0.116
FEAR [§]		–	108.80	14.6	99.08	0.46+0.46	–
WWW		2.373	109.16	11.1 (10.9)	100.0	0.0+0.0	0.185
INDIA	300	2.386	109.11	11.4 (10.8)	99.33	0.33+0.33	0.219
SW-MD		2.380	109.22	9.3 (8.5)	99.33	0.33+0.33	0.140
WWW		2.378	109.18	10.5 (10.1)	100.0	0.0+0.0	0.185
INDIA	512	2.387	109.09	11.5 (10.6)	99.60	0.20+0.20	0.216
SW-MD		2.379	109.27	9.1 (8.6)	99.22	0.39+0.39	0.125
ML-MD[†]		2.371	109.19	9.7 (9.4)	98.44	0.78+0.78	0.138
FEAR[‡]		2.350	–	–	95.90	1.17+2.73	–
WWW		2.365	109.11	10.7 (10.5)	100.0	0.0+0.0	0.192
INDIA	1024	2.390	109.01	11.9 (10.8)	98.34	1.07+0.49	0.236
SW-MD		2.381	109.27	9.3 (8.6)	99.22	0.59+0.19	0.132
FEAR[‡]		2.360	–	–	94.53	2.34 + 3.13	–
WWW		2.371	109.14	10.6 (10.3)	100.0	0.0+0.0	0.189

[*] Values within parentheses are from a Gaussian approximation.
[§] From Ref. [98].
[†] From Ref. [25].
[‡] From Ref. [101].

suggests that the two models are similar as far as the correlations between dihedral angles are concerned. A ball-and-stick representation of a 512-atom INDIA model is shown in Fig. 3.6.

Further characterization of the network is possible by examining the bond-orientational order parameter (BOP), Q_l, as defined by Steinhardt *et al.* , [119] which provides information on the orientation of a group of bonds. Figure 3.7 shows the Q_l values, for l = 1 to 8, for INDIA, WWW and SW-MD models consisting of 512 atoms. The BOP not only incorporates some aspects of structural information from higher-order correlation functions, but also provides a simple and effective measure for determining the presence of microcrystalline or paracrystalline structural units in the networks. [83] Here, we have used Q_l (l=1,2,5) to determine the *degree of crystallinity*. While the magnitude of Q_1, Q_2 and Q_5 are exactly zero

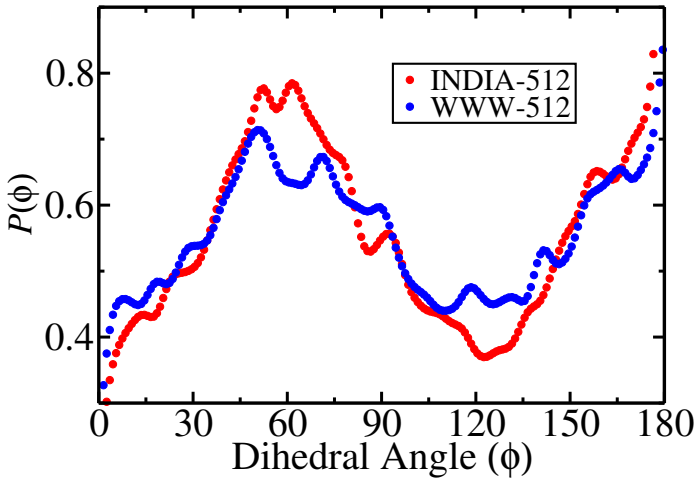

Figure 3.5: Dihedral-angle distributions, $P(\phi)$ from 512-atom INDIA (red) and WWW (blue) models. The characteristic dihedral peak at 60° and a dip at 120° are distinctly visible in the distributions.

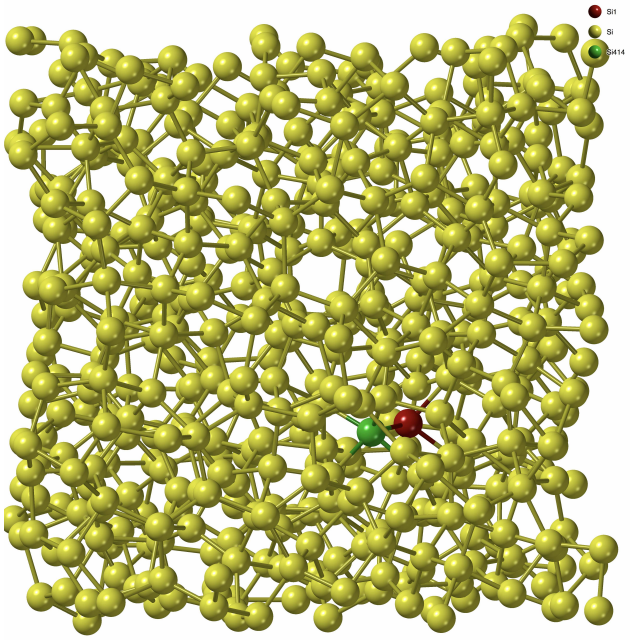

Figure 3.6: A ball-and-stick representation of a 512-atom INDIA model with a pair of floating (green) and dangling (red) bonds. The remaining 4-fold coordinated Si atoms are shown in yellow color.

for ideal *c*-Si [24] networks, a high value of Q_5 for the INDIA and WWW models indicates more amorphous or disordered nature of these models in comparison to the SW-MD model. This observation is in agreement with the conclusion followed from the Voronoi-volume

Table 3.3: Ring statistics for INDIA, WWW, and two MD models comprising N = 216, 300, 512, 1024 atoms. Columns 3 to 8 list the number of rings per atom from ring sizes 4 to 9, respectively.

Model	N	4	5	6	7	8	9
INDIA		0.005	0.389	0.889	0.611	0.139	0.032
SW-MD	216	0	0.278	1.125	0.676	0.060	0.009
WWW		0.028	0.444	0.745	0.528	0.171	0.040
INDIA		0.017	0.403	0.860	0.537	0.173	0.023
SW-MD	300	0.007	0.353	0.990	0.597	0.107	0.017
WWW		0.003	0.420	0.857	0.537	0.133	0.020
INDIA		0.018	0.404	0.789	0.613	0.152	0.014
SW-MD	512	0.008	0.359	0.939	0.619	0.133	0.023
ML-MD[†]		0.014	0.389	0.856	0.643	0.104	0.018
WWW		0.039	0.467	0.717	0.465	0.191	0.033
INDIA		0.020	0.422	0.785	0.535	0.157	0.035
SW-MD	1024	0.003	0.320	1.044	0.609	0.094	0.021
WWW		0.026	0.443	0.754	0.505	0.153	0.027

[†] From Ref. [25].

distribution as shown in Fig. 3.3(c).

The connectivity of atoms in amorphous networks can be analyzed by computing the statistics of irreducible rings of varying sizes. Rings are an important feature of topological networks, which are defined as closed irreversible paths or loops that start and end at

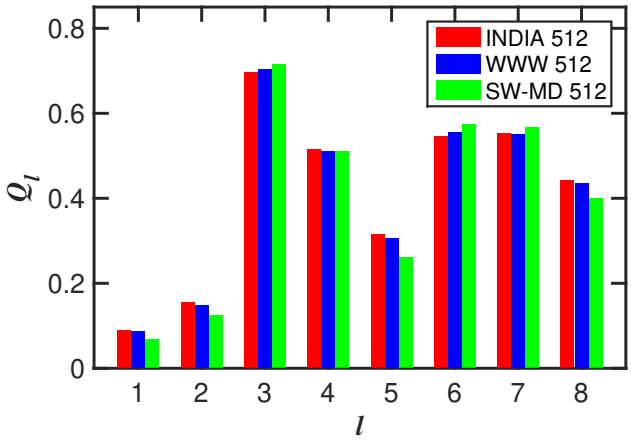

Figure 3.7: The distribution of the bond-orientational order parameter, Q_l, for the 512-atom INDIA (red), WWW (blue) and SW-MD (green) models.

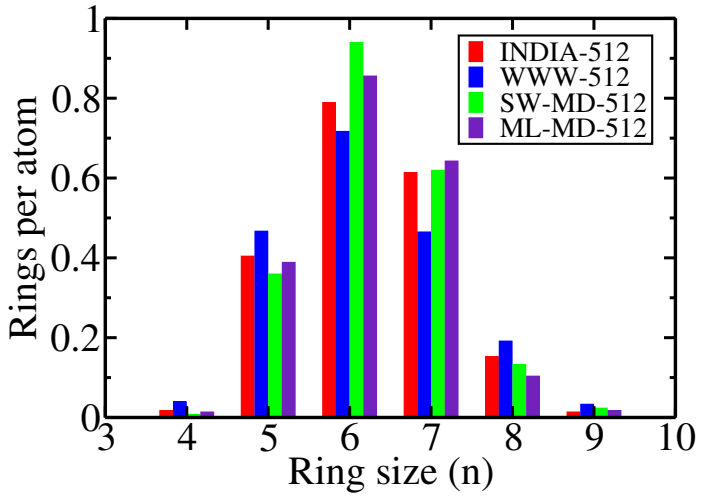

Figure 3.8: Ring statistics for four different models of *a*-Si of size 512 atoms. The SW-MD model shows a relatively strong presence of six-member rings compared to its WWW and INDIA counterparts.

the same atomic site. Here, irreducibility implies that the ring cannot be further divided into rings of smaller/equal size by topologically deforming the original ring in the space of the embedding dimension. By treating an amorphous network as a *simple connected* graph, $G = (V,E)$, where $V(G)$ is a vertex set consisting of atomic centers and $E(G)$ is an edge set consisting of bonds between two nearest-neighbor atoms, one can obtain the irreducible ring-size distribution by computing the adjacency matrix of $V(G)$. Table 3.3 lists the irreducible-ring statistics for a number of INDIA, WWW, and two MD models, obtained using periodic boundary conditions. The results for these four 512-atom models are presented in Fig. 3.8. It is apparent that the ring-size distributions in the INDIA and WWW models are essentially similar, whereas the SW-MD model shows a comparatively high number of 6-member rings in the network. Table 3.3 confirms that this observation also applies to the rest of the SW-MD models. A comparison with the results obtained from 216-, 300- and 1024-atom INDIA and WWW models leads us to believe that this *excess topological crystal-like feature* of SW-MD models could be attributed to the modified SW potential, which exhibits a tendency to form diamond crystals during MD simulations. It is also plausible that MD simulations can sample the solution space more accurately than a total-energy-based relaxation method in determining a low-energy structure, which is topologically closer to the crystalline diamond network. The values of ΔE for the MD models, listed in Table 3.2, appear to support this conjecture. In future, we expect to address this issue by taking into account the presence of a few coordination defects that may affect the ring-size distribution.

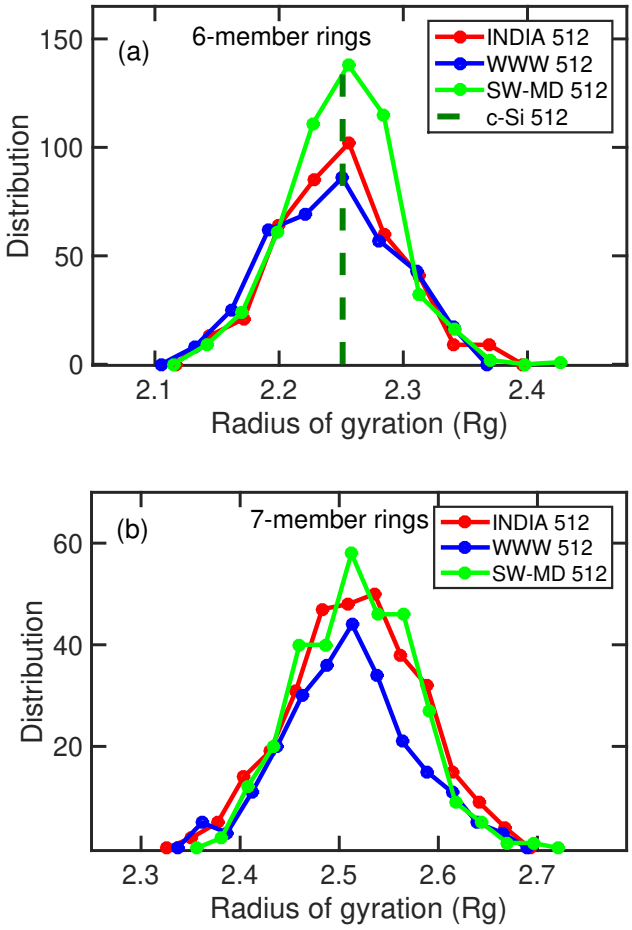

Figure 3.9: The distribution of the radii of gyration of (a) 6-member rings and (b) 7-member rings for the 512-atom INDIA (red), WWW (blue) and SW-MD (green) models of *a*-Si. The R_g value of 6-member rings for ideal *c*-Si networks is shown by a vertical (green) line in Fig. 3.9(a).

We also examined the topological connectivity and the associated length scale(s) for various irreducible ring structures present in the amorphous networks by computing the radius of gyration (R_g) of the rings. The R_g values and the numbers of the high-member rings ($\geq$ 7-member) can be indicative of the presence of intermediate range order (IRO) in amorphous networks. The distributions of R_g of 6-member rings and 7-member rings are shown in Fig. 3.9(a) and Fig. 3.9(b) for the 512-atom models, respectively. The plot in Fig. 3.9(a) indicates the presence of more 6-member rings in the SW-MD model compared to the INDIA and WWW models of an identical size. This can be attributed to the somewhat more ordered nature of the SW-MD model, which has been obtained from the MD simulations and thus can be compared with annealed samples of *a*-Si. The average R_g value of 6-member rings in *c*-Si is found to be 2.25 Å, which is somewhat lower that the average

bond length (of 2.35 Å) in ideal *c*-Si, due to the non-planar nature of the hexagonal rings. Similarly, Fig. 3.9(b) shows the results for 7-member rings that are somewhat larger than the corresponding 6-member rings.

3.3.2 Electronic and Vibrational Properties

While the results in the preceding section establish the structural quality of the INDIA models, a strong coupling between local environments of atoms and the vibrational and electronic degrees of freedom in *a*-Si warrants further examination to validate the vibrational and electronic properties of the models. A good atomistic model of *a*-Si must exhibit a clean elelctronic band gap around the Fermi level and the size of the gap should determine the electronic quality of the model, by jointly taking into account the structural quality and the density of coordination defects in the network. Although theoretical considerations [120] lead to the existence of such a spectral gap in tetrahedral amorphous networks, it has been noted that the size of the gap and the density of states in its vicinity are particularly susceptible to coordination defects. Until the recent developments of high-quality MD models [24, 25], only WWW models were capable of producing a clean gap in the electronic spectrum around the Fermi level. It is therefore imperative to validate the accuracy of new atomistic models by computing the EDOS and the size of the gap therefrom. Likewise, the energy required to excite vibrational degrees of freedom in *a*-Si, typically a few tens of meV, suggests that the latter can be very sensitive to local atomic arrangements, which may not be apparent in the electronic spectrum. Thus, a final analysis should also include a statement on the vibrational density of states of the models.

Table 3.4: Comparison of band-gap values (in eV) for *a*-Si models obtained from the INDIA, WWW, and SW-MD simulations.

Model size	216	300	512	1024
INDIA	0.753	0.884	1.007	0.38
WWW	1.007	1.008	1.013	1.012
SW-MD	1.003	0.881	1.006	1.009
Experiments*		1.6–1.75		

* Quoted values are for device-grade *a*-Si:H from Ref. [121].

Figure 3.10 depicts the EDOS for 512-atom INDIA and WWW models, with the Fermi levels at 0 eV. The INDIA model produces a clean gap, which accurately matches the same from the WWW model. This observation also applies to the 216- and 300-atom INDIA models. Table 3.4 lists the values of the band gaps obtained from four INDIA models, along

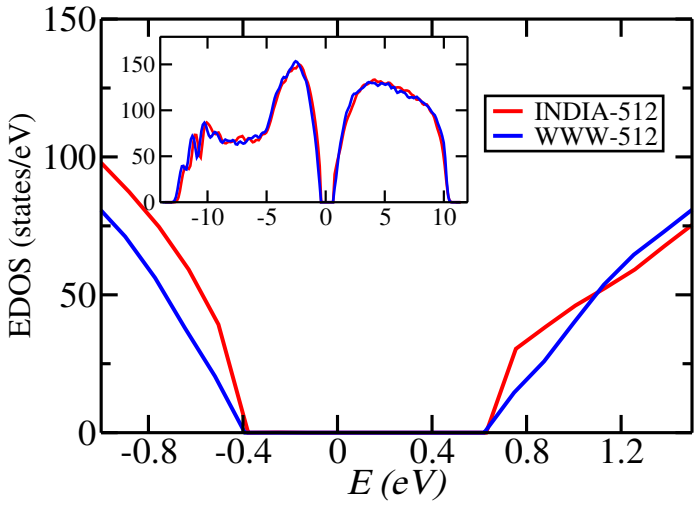

Figure 3.10: The densities of electronic states of *a*-Si from INDIA (red) and WWW (blue) models with the Fermi level at 0 eV. A pristine electronic gap of size approximately 1 eV is clearly visible.

with the corresponding values from the WWW and SW-MD models. The results can be summarized by making the following observations: (1) The EDOS and the size of the gap from the 512-atom INDIA model match accurately with the corresponding results from the WWW and SW-MD models (cf. Table 3.4). (2) A small but noticeable difference in the shape of the valence-band tails for the 512-atom INDIA and WWW models in Fig. 3.10 can be attributed to a combination of the lack of statistics and the different degree of disorder associated with bond angles and bond lengths, and ΔE of the networks (0.22 eV for INDIA vs. 0.19 eV for WWW). (3) A small value of the band gap (0.38 eV) noted for the 1024-atom INDIA model points to the presence of 1.6% coordination defects and, possibly, the presence of a few strained bonds, as indicated by a slightly higher value of ΔE = 0.24 eV. Overall, the electronic properties of the INDIA models are on a par with the WWW models.

We studied the specific heat at constant volume (C_v) of the 300- and 512-atom INDIA models in the temperature range of 10 K–300 K. The specific heat was calculated from the (discrete) vibrational frequencies (ω) obtained from direct diagonalization of the dynamical matrices in the harmonic approximation using the relation, [92]

$$C_v(T) = k_B \sum_{\boldsymbol{k},j} \frac{(\frac{\hbar\omega_j(\boldsymbol{k})}{2k_BT})^2}{\sinh^2(\frac{\hbar\omega_j(\boldsymbol{k})}{2k_BT})}, \tag{3.4}$$

and compared the resulting values with the experimental data obtained by Zink *et al.* [122] at low temperature in the range from 10 K to 300 K. As mentioned in Sec. 3.2, the dynamical matrices of the models were obtained from employing the density-functional code SIESTA.

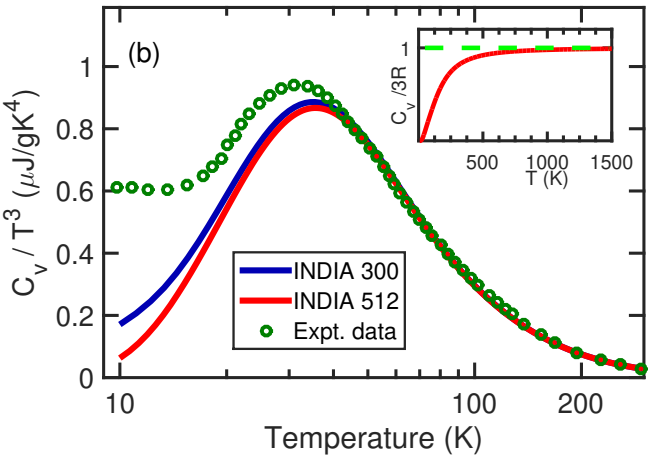

Figure 3.11: The low-temperature dependence of the specific heat of the 300- and 512-atom INDIA models compared with the experimental data (green) from Zink *et al.* , [122] and the classical *Dulong-Petit limit*.

Given the temperature range studied here, the harmonic approximation was found to be adequate in the present work. In Eq. 3.4, the sum over $\boldsymbol{k}$ corresponds to the Γ point only. Figure 3.11 shows the low-temperature dependence of the specific heat (C_v/T^3) with temperature from 10 K to 300 K. The results suggest that the INDIA models are in good agreement with the experimental data for $T > 40$ K. The inset shows the classical Dulong-Petit limit, $C_v \rightarrow 3R$, as the temperature approaches to 300 K.

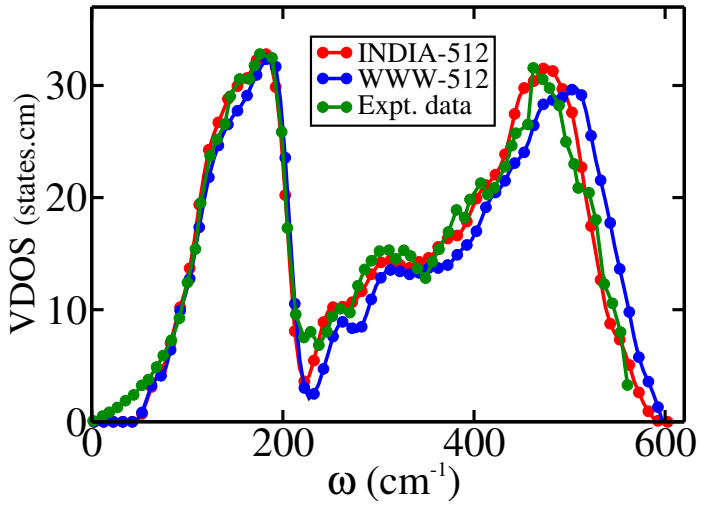

Figure 3.12: The vibrational densities of states (VDOS) of *a*-Si from 512-atom INDIA (red) and WWW (blue) models. Experimental data from inelastic neutron-scattering measurements, from Ref. [123], are also shown for comparison.

Finally, Fig. 3.12 shows the vibrational densities of states of 512-atom INDIA and WWW models, obtained by diagonalizing dynamical matrices that were constructed in the harmonic approximation, along with the experimental data from inelastic neutron-scattering measurements by Kamitakahara *et al.* [123]. The computed VDOS from the INDIA model agrees well with experiments. In particular, the VDOS from the INDIA model in the region from 300 cm^{-1} to 600 cm^{-1} has been found to fit more accurately with experimental data than its WWW counterpart.

3.4 Conclusions

In this work, we have presented an information-driven inverse approach, or INDIA, to invert experimental diffraction data in conjunction with a few structural constraints and a total-energy functional. Since one-dimensional scattering data alone cannot describe a three-dimensional distribution of atoms uniquely, and the presence of too many structural constraints can make the inversion problem somewhat ill posed, we have followed a hybrid strategy to augment the dimension of the search space in an effort to determine an accurate structural solution of the inversion problem, aided by a total-energy functional. It has been shown that the original inversion problem can be posed as a non-convex optimization problem in an extended or augmented search space that involves information from a set of experimental diffraction data, a few structural constraints, and an approximate total-energy functional of the system. We then demonstrate that the complexity associated with solving the resulting optimization program can be considerably reduced by decomposing the extended objective function into two subspace objective functions and optimizing these two functions sequentially in a self-consistent way.

An examination of the optimal structural models, consisting of up to 1024 atoms, shows that the vibrational, electronic, and structural properties of the models match accurately with the corresponding experimental data from *as-deposited* samples of amorphous silicon. In particular, the first sharp diffraction peak of a 512-atom INDIA model has been found to match somewhat more accurately with experimental structure-factor data than its corresponding WWW counterpart. Likewise, a comparison of the vibrational density of states (VDOS) with inelastic neutron-scattering data reveals that the 512-atom INDIA model reproduces the density of high-frequency vibrations more accurately than the corresponding WWW model. Further analyses of various structural properties, involving the pair-correlation function, the bond- and dihedral-angle distributions, and the statistics of n-member irreducible rings ($n = 4$ to 9) in the networks, show that the INDIA models are on a par with the high-quality WWW models and those obtained from recent high-quality MD simulations using the modified

Stillinger-Weber and machine-learning-driven potentials. The electronic densities of states, specifically the ones from 300- and 512-atom models, obtained from a local-basis density-functional code SIESTA using the generalized gradient approximation, show the presence of a pristine gap in the electronic spectrum in the vicinity of the Fermi level, with only a pair of coordination defects. The size of the electronic gaps from the INDIA models is found to be comparable with those from the corresponding WWW models. Furthermore, the estimated values of the heat of crystallization of the models closely compare with those obtained by Roorda *et al.* [117] and Donovan *et al.* [118] from differential scanning calorimetry measurements. In conclusion, the information-driven approach and its implementation presented here can successfully invert a set of diffraction data and structural constraints in conjunction with a total-energy functional by producing atomistic models of *a*-Si, which are significantly better than existing hybrid RMC models of *a*-Si and are on a par with the WWW models, as far as the structural, electronic, thermodynamic and vibrational properties of *a*-Si are concerned.

Chapter 4

DISORDER BY DESIGN: A DATA-DRIVEN APPROACH

The work presented in this chapter has been published in **Limbu, D. K., Elliott, S. R., Atta-Fynn, R. & Biswas, P. Disorder by design: A data-driven approach to amorphous semiconductors without total-energy functionals.** *Scientific Reports* **10,** 7742, (2020).

4.1 Introduction

Experimental information from scattering measurements, such as X-ray, electron and neutron diffraction, play an important role in the structural determination of ordered and disordered materials. [124, 125] Diffraction experiments typically provide scattering intensities from the constituent atoms in the wavevector space, which are related to the two-body correlation function between atoms in real space via the Fourier transform of the structure factor. For amorphous solids, the reconstruction of the correct three-dimensional real-space structure from scattering data is an archetypal example of inverse problems in computational modeling of materials. Since the lack of information from higher-order atomic-correlation functions cannot be remedied by any amount of computational/mathematical trickeries, it is absolutely necessary to supplement experimental data by additional information to determine a unique structural model of a material. Among earlier approaches to address the problem, the reverse Monte Carlo (RMC) method [81] is an elegant method that relies on the generation of Markov chains or random walks to optimize a suitable cost function in the state-vector or configurational space. While a variant of the RMC method was used by Strong and Kaplow [126, 127] as early as the 1960s to predict the structure of crystalline B_2O_3 [126] and vitreous selenium, [127] by refining X-ray diffraction data via random walks, it was McGreevy and co-workers [31, 81, 128] who first applied the method systematically to model the structure of disordered solids. [81] Since then, the method has been widely used to study a variety of complex disordered systems, including liquids, glasses, disordered alloys, and proteins. [31]

Despite significant efforts over the past decades, direct application of the RMC method to determine reliable structural solutions of disordered materials from their diffraction data has remained a challenging problem to date. The problem is particularly acute for amorphous tetrahedral semiconductors, such as amorphous silicon (a-Si) and germanium

(*a*-Ge). Although a number of RMC or RMC-derived studies [30–32, 34, 60, 81, 93, 99, 100, 128] on *a*-Si/*a*-Ge have been reported in the past, none of these could demonstrate the presence of a gap in the electronic spectrum and a low concentration of coordination defects ($\leq 1\%$), as observed in optical measurements [121, 129] and electron spin resonance (ESR) [94] experiments, respectively, for these materials. Thus, the problem of the structural determination of tetrahedral amorphous semiconductors from diffraction data *without* using a total-energy functional remains unsolved up until now. Since an ensemble of three-dimensional structures can lead to an identical two-body correlation function, additional information is required to uniquely determine the correct structure of a material by suitably reducing the volume of the solution space. While this reduction is generally achieved by imposing structural constraints during RMC simulations, the hierarchy and conflictive nature of the constraints render the resulting optimization problem very difficult, leading to poor structural solutions. To overcome this problem, a new breed of hybrid approaches have been developed in recent years [35–37, 61, 116], which can successfully address the uniqueness problem by simultaneously employing experimental data and a total-energy functional. However, these hybrid approaches crucially rely on the availability of suitable total-energy functionals and often, for many multinary systems, it is difficult to guide the hybrid solutions without resort to the use of expensive quantum-mechanical force fields. This considerably increases the computational complexity of the problem, which limits the applicability of *ab initio*-based hybrid approaches in addressing large disordered systems. This necessitates the development of purely data-driven information-based approaches to material simulations, which rely on experimental data and auxiliary structural information.

The principal aim of this chapter is to demonstrate conclusively that an accurate structural solution for tetrahedral amorphous semiconductors can be obtained *without* the need for a total-energy functional or atomic forces but using diffraction data only, assisted by a few structural constraints. By developing an efficient constraint optimization scheme, within the framework of Monte Carlo methods, which scales linearly with the system size, we show that tetrahedral models of *a*-Si can be constructed by the judicious use of local structural/chemical constraints and diffraction data. More importantly, we demonstrate that the data-driven information-based models are energetically stable in the sense that the models correspond to a stable local minimum of a quantum-mechanical total-energy functional and that the models produce a clean gap in the electronic spectrum. Furthermore, we show that the resulting models exhibit structural, electronic, and vibrational properties of *a*-Si that match excellently with the corresponding experimental data from X-ray, Raman spectroscopy, and inelastic neutron-diffraction measurements, as well as those obtained from using conventional simulation techniques, based on classical and quantum-mechanical force

fields. Finally, we discuss an extension of the scheme with a few examples to incorporate microstructural properties of realistic samples of *a*-Si and *a*-Ge as observed in experiments.

4.2 Materials and Methods

In our multi-objective constraint optimization approach, we begin with an objective function, $\chi^2(\mathbf{R})$, which includes information from experimental diffraction data and a set of structural constraints,

$$\chi^2(\mathbf{R}) = \sum_{i=1} \left[\frac{F_{ex}(q_i) - F_c(q_i;\mathbf{R})}{\sigma(q_i)} \right]^2 + \sum_{l=1}^{l_m} \lambda_l C_l(\mathbf{R}), \tag{4.1}$$

where $F_c(q;\mathbf{R})$ correspond to simulated diffraction data, either in wavevector space ($q = k$) or in real space ($q = r$), obtained from a distribution of atoms $\mathbf{R}$, $\sigma(q_i)$ is the error associated with experimental data, $F_{ex}(q_i)$, and C_ls are a set of l_m constraints, providing additional information on the structural properties of the solid. The coefficients λ_l are weights, which determine the relative strength of each constraint in Eq. (4.1). To incorporate constraint information, we prescribe a convex function, $C_l = (f_l(\mathbf{R}) - f_l^0)^2$, where f_l represents a structural variable, associated with a configuration $\mathbf{R}$, and f_l^0 corresponds to the same for a true but unknown solution $\mathbf{R}_0$. Our goal is to determine an accurate structural solution $\mathbf{R}_0'$, which is *sufficiently* close to $\mathbf{R}_0$, by simultaneously minimizing $C_l(\mathbf{R})$ and fitting the computed structure-factor or pair-correlation data with their experimental counterpart. Two structural configurations, $\mathbf{R}_0$ and $\mathbf{R}_0'$, are considered to be sufficiently close when a minimal number of physical observables, derived from these configurations, are found to be almost identical to each other and that these observables can be employed to define a structure uniquely. For amorphous tetrahedral semiconductors, the local chemistry suggests, $f_1 = \langle\theta\rangle$, $f_2 = \Delta\theta$, and $f_3 = c_4$, where $\langle\theta\rangle$, $\Delta\theta$ and c_4 represent the average bond angle, the root-mean-square (RMS) deviation of θ, and the percentage of four-fold-coordinated atoms in $\mathbf{R}$, respectively. The parameters λ play an important role in the optimization of the objective function, $\chi^2(\mathbf{R})$, which largely determine the evolution of an approximate solution, $\mathbf{R}_0'$, via important sampling of the objective function in high-dimensional space, using Monte Carlo simulations. One frequently chooses λ_l, by trial and error, so that both the objective function and its constraint components can be simultaneously optimized during the CMC runs. It may be noted that several pareto-optimal sets of λ_l exist, which suffice to generate good structural solutions. The intention here is not to find an optimal set of λ values, which is analogous to developing a three-body potential, but to obtain accurate structural solutions consistent with given data sets. To obtain a close structural solution, $\mathbf{R}_0'$, the inversion procedure was implemented by minimizing Eq. (4.1), using simulated annealing techniques. An initial

random configuration, consisting of N Si atoms in a cubical box of length L, was generated so that the density of the model corresponds to the experimental density, 2.25 g/cm^3, of a-Si, and no two atoms were at a distance less than 2 Å. The latter was enforced throughout the course of simulations to maintain an excluded volume of radius 1 Å surrounding each Si atom. By choosing $F_c(q;\mathbf{R})$ as the pair-correlation function, the Metropolis algorithm was employed to accept or reject a trial move, $\mathbf{R}_i \rightarrow \mathbf{R}_f$, following the Metropolis acceptance probability $P = \min\left[1, \exp(-\beta\Delta\chi^2)\right]$, where $\Delta\chi^2 = \chi^2(\mathbf{R}_f) - \chi^2(\mathbf{R}_i)$ and β $(= 1/k_BT)$ is an optimization parameter or the inverse temperature of the system. The system was initially equilibrated at a (hypothetical) temperature of 310 K for 10^5 Monte Carlo steps (MCS), which was followed by linear cooling of the system from 310 K to 10 K, in steps of 25 K, for every 10^5 MCS at each temperature. The procedure was then repeated, from 110 K to 1 K, for at least 5 or more cycles, until the RMS width of the bond-angle distribution and the concentration of coordination defects reduced to about 11° and 1%, respectively. The simulations were performed by moving one atom at a time and the maximum atomic displacement was restricted to 0.15–0.2 Å in order to keep the acceptance rate as high as possible.

The advantage of moving of one atom (or a few atoms) at a time is that it provides a means to move atoms in the specific regions of interest and to develop an order-N optimization algorithm for the computation of $\Delta\chi^2$, associated with the displacement of one atom (or a few atoms). [130] The linear scaling was achieved by updating an initially generated pair-correlation function and the list of nearest neighbors of a (few) selected atom(s) as the simulation proceeds as shown in Fig. 4.1. This was particularly necessary to address systems larger than 500 atoms. A detailed description of the order-N method will be presented elsewhere. Depending upon the temperature, the size of the system and the magnitude of the maximum possible displacement of an atom during MC simulations, the acceptance rate (of the MC moves) was found to vary from 25% to 50%. After several trial runs, we settled for two sets of λ values. For 1000-atom models, we used λ_1 = 2/3, λ_2 = 4/3, and λ_3 = 2/3, whereas the corresponding values for 216-atom, 300-atom, and 512-atom models are given by 1/3, 2/3, and 1/15, respectively. Given the pareto-optimal nature of the problem, it is possible to employ a different set of λ values in order to incorporate constraints with a varying strength. To conduct the configurational averaging of physical properties and to demonstrate the reproducibility of results from our method, ten independent configurations for each system size were generated and studied in our work. Since the results from simulated annealing techniques may often vary, depending upon the cooling protocol used in simulations, we also employed a second cooling scheme with an exponential decay of temperature to examine its possible effect on the quality of the final solutions. The results from the

exponential cooling scheme were found to be similar to those from the linear cooling scheme.

Having provided an ansatz for reconstructing the three-dimensional structure of tetrahedral amorphous semiconductors, without using a total-energy functional, via the inversion of experimental data in the presence of structural constraints, we now address the realistic modeling of microstructure of *a*-Si/*a*-Ge observed in experiments. The use of a minimal number of constraints leads to a natural solution as continuous random networks (CRN). However, it is widely acknowledged that a CRN model cannot provide a comprehensive description of *a*-Si/*a*-Ge, and the microstructure of *a*-Si/*a*-Ge from experiments may considerably vary from sample to sample, depending upon the method of preparation, history of the samples, preparation conditions, etc. Thus, while a CRN model provides for the most part a correct description of some key structural and electronic properties of *a*-Si, it cannot produce many important characteristics of laboratory-grown samples, such as the distributions of defects and microvoids, local inhomogeneities, and the presence of different topologically-connected regions, [19] observed in experiments. These microstructural properties are often addressed by introducing ad hoc structural measures or changes in CRN models. For example, the results from fluctuation electron microscopy (FEM) [19] are often explained either by including small grains of paracrystals [19] or nanometer-size voids, [105] density fluctuations by implanting vacancy-type defects, [39, 107, 131] and extended inhomogeneities by voids [132] in CRN models. Although these ad hoc measures are found to be largely successful in describing the microstructural properties of *a*-Si and *a*-Ge, associated with various methods of preparation and experimental conditions, they cannot nevertheless replace the need for a systematic data-driven method. While machine-learning (ML) approaches appear to be a promising route to address some of these issues, their success crucially depends upon the availability of suitable training data and the ability of the underlying ML model to obtain an optimal set of learning parameters, which involves solving an optimization program under a different guise. Likewise, the majority of conventional MD simulations tend to produce too many dangling-bond defects ($\geq 5\%$), which often render the MD models unsuitable without further treatment, as far as the defect density and electronic density of states (EDOS) are concerned.By contrast, the information-based approaches can be generalized by directly including appropriate microstructural constraints, guided by experimental information or data, to develop models with realistic microstructural properties as observed in experiments. For example, to generate *a*-Si models with a given void-volume density, or vacancy-type defects, one may include an additional term $g(\mathbf{r}, R_v)$

to $\chi^2(\mathbf{R})$ and write,

$$\chi'^2(\mathbf{R}) = \chi^2(\mathbf{R}) + \sum_k \gamma_k |g(\mathbf{r} - \mathbf{r_k}; R_v)|^2, \tag{4.2}$$

where $g(\mathbf{r} - \mathbf{r_k}; R_v)$ is a function that produces a void, or a vacancy, at $\mathbf{r} = \mathbf{r_k}$ of linear size R_v. Equation (4.2) can be viewed as a regularization of the original objective function in (4.1), which can be optimized for a suitable value of γ and $g(\mathbf{r}, R_v)$. The shape and size of the voids can be approximately controlled by choosing a suitable functional form of $g(\mathbf{r} - \mathbf{r_k}; R_v)$. For example, a spherical void or vacancy region can be constructed by using an inverse quadratic function or a Fermi function, characterized by an appropriate shape parameter, which determines the boundary region of a void/vacancy from the rest of the network. The efficacy of this approach to describe the microstructure of *a*-Si is illustrated by providing two examples involving voids and vacancy-type defects.

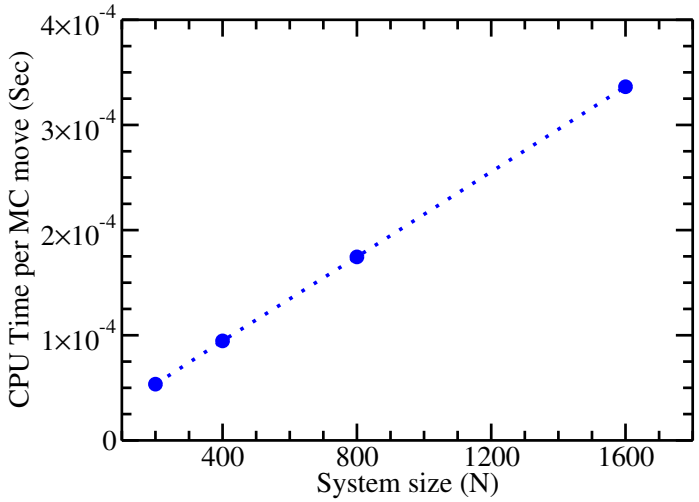

Figure 4.1: The variation of CPU time (in seconds) with system size N for a single MC move, associated with the evaluation of the objective function (see Eq. (4.1)). The CPU time is found to scale linearly with N.

4.3 Results and Discussion

In discussing our results, we first demonstrate the superior structural quality of the new models over existing RMC or RMC-like models. This is followed by an extensive comparison of the results from our models with those from conventional Monte Carlo and molecular-dynamics simulations, using classical, quantum-mechanical, and machine-learning-based potentials. We have placed great emphasis on the electronic structure of *a*-Si, as it is the electronic properties that are most difficult to produce accurately, not only in RMC/RMC-like methods but also in MD and MC simulations, and are often not discussed in the literature

Table 4.1: Comparison of results from various information-based approaches. N, $\langle\theta\rangle$, $\Delta\theta$, c_4 and E_g indicate the size of the system, the average bond angle, the RMS width of bond angles, the percentage of four-fold-coordinated atoms and the value of the electronic gap, respectively.

Model	N	$\langle\theta\rangle$	$\Delta\theta$	c_4	E_g (eV)
CMC19	216	109.08	10.95	100	1.18
CMC19	512	109.14	10.61	99.22	1.09
SOAP [§]	512	NA	NA	95	None
EX-INVERT [†]	216	NA	NA	94-97	NA
INVERT [‡]	512	NA	NA	92[§]	None
RMC04 [*]	500	109.01	12.5	88	None
RMC96 [⋆]	3000	109.4	8.5	52	None

[§] Estimated values from supplementary information in Ref. [100].
[†] From Ref. [133].
[‡] From Ref. [99].
[*] From Ref. [32].
[⋆] Results for *a*-Ge from Ref. [93].

with sufficient detail. We then proceed to compare our results with hybrid models that employ both total-energy functionals and experimental data. This is followed by new ideas that serve as natural corollaries of the current approach in an effort to address microstructural properties of experimentally obtained *a*-Si samples, which cannot be described using conventional continuous random network (CRN) models of *a*-Si. Since the multi-objective constraint optimization problem in the present study was handled by using constraint Monte Carlo (CMC) methods, we shall refer to our models as CMC19 hereafter.

4.3.1 Comparison with earlier RMC-derived models

To examine the accuracy of structural quantities and the novelty of the CMC19 approach, we begin by listing the characteristic properties of the CMC19 model in Table 4.1, along with those obtained from various RMC [32, 93] and RMC-derived [99, 100, 133] approaches. A salient feature of all these methods is that none of the methods uses any total-energy functionals during structural formation but only experimental data in conjunction with a few constraints. The results clearly indicate that the CMC19 models outperform all other models, as far as the values of $\Delta\theta$, c_4, and E_g in Table 4.1 are concerned. Although the lack of precise information on the bond-angle distribution from INVERT and SOAP models, in particular the root-mean-square (RMS) bond-angle width, $\Delta\theta$, makes it difficult to compare our results on a quantitative footing, it is evident that the INVERT and SOAP

models produce too many defects (about 5–8%) to open a gap in the respective electronic spectrum. It may be noted that the structural and electronic quality of a model *a*-Si network is primarily determined by – apart from the structure factor or its real space counterpart – a trinity of three quantities: a) the width of the bond-angle distribution ($\Delta\theta$); b) the concentration of four-fold-coordinated atoms (c_4) in a tetrahedral environment; and c) the value of the electronic gap (E_g). It is therefore crucial for a realistic model of *a*-Si to exhibit a small value of $\Delta\theta$ (of about 9–12°) and a large value of c_4 (typically $\geq 98\%$). While an extension of the INVERT approach, EX-INVERT, [133] is reported to have produced highly four-fold-coordinated networks with c_4 values of up to 97%, the author provided no data on the width of the bond-angle distribution and the statistics of atomic coordination in Ref. [133]. Given the multi-objective nature of the problem, it is possible to construct a network with a low concentration of coordination defects at the expense of a high value of $\Delta\theta$, and vice versa. However, such networks may not represent a stable physical solution upon total-energy relaxation. Thus, a structural model from a data-driven information-based approach must satisfy the aforementioned criteria simultaneously in order to be compliant with experimental data from Raman and optical measurements, and electron spin resonance experiments. By contrast, the CMC19 models obtained in the present study clearly and unambiguously satisfied all these criteria. It is remarkable that the 216-atom CMC19 model produces a 100% four-fold-coordinated network with an RMS width of bond angles of about 10.95° and an electronic gap of magnitude 1.18 eV. We emphasize that this is the first ever data-driven information-based model that produces no defects and a clean electronic gap, without using a total-energy functional during structural formation. This constitutes one of the major outcomes of the present study. In the following section, we shall demonstrate that even the unrelaxed CMC19 models of *a*-Si are capable of producing a gap in the electronic spectrum and that the structural properties of the models are energetically stable, i.e., almost independent of *ab initio* total-energy relaxations.

4.3.2 Comparison with total-energy-based models

In order to demonstrate the efficacy of the data-driven CMC19 approach over conventional approaches, using total-energy and forces, we now compare the results with an array of models from molecular dynamics and Monte Carlo simulations. While there exist a plethora of such models in the literature, we confine ourselves to few high-quality *a*-Si models that can produce accurate structural, electronic, and vibrational properties of *a*-Si. To this end, we chose four representative models for comparison: 1) a classical molecular-dynamics (MD) model [24] based on the modified Stillinger-Weber potential [57]; 2) an MD model based

on machine-learning (ML) potential [25]; c) an *ab initio* MD model [58]; and d) a model obtained from using the Wooten-Winer-Weaire (W3) [22] algorithm, modified by Barkema and Mousseau (BMW3). [23] The latter can produce large 100% defect-free configurations of *a*-Si, and it is often considered as the benchmark for high-quality *a*-Si models from simulations. These four models will be collectively referred to as *total-energy-based* (TEB) models.

Table 4.2 presents an overview of structural properties of the TEB models, along with the CMC19 models of size from 216 to 1000 atoms before and after *ab initio* relaxations. It is apparent that the structural quality of the CMC19 models is on a par with the BMW3 model, and that the former are considerably better than those derived from AIMD and MLMD models, as far as the four-fold coordination of the models are concerned. This observation equally applies to the electronic quality of the models, which is reflected in the size of the electronic gap. Considering the long simulation time ($\geq$ 20 ns) needed to produce the SWMD models and the complexity associated with generating a machine-learning potential for *a*-Si, it is evident that the CMC19 approach produces *a*-Si models par excellence, using diffraction data and constraints only. Not only do the CMC19 models show the presence of an essentially clean gap in the electronic spectrum, but also the size of the gap, E_g, matches closely with the value obtained from the BMW3 model. A relatively small value of E_g for the 1000-atom CMC19 model can be attributed to the presence of 0.9% coordination defects and a somewhat larger value of $\Delta\theta$, compared to its BMW3 counterpart, which affect the band-edge states.

Figure 4.2(a) presents the structure factor of *a*-Si obtained from a 512-atom CMC19 model. For comparison, the corresponding structure factor from a BMW3 model of identical size and from experiments [115] are also included in Fig. 4.2(a). Owing to the form of the objective function in Eq. (4.1), it is not surprising that the structure factor from the CMC19 model matches closely with the same quantity from the BMW3 model and the experimental data from as-deposited samples in Ref. [115]. Likewise, the bond-angle distribution in Fig. 4.2(b), with an RMS bond-angle width of 10.61°, is also found to match very well with its BMW3 counterpart, which is characterized by a root-mean-square (RMS) width, $\Delta\theta$, of 10.36°. Assuming that the bond-angle distribution can be approximated by a Gaussian function, this value corresponds to a full width at half maximum (FWHM) of 23–25°, which closely matches with the measured value of the FWHM of about 22-23°, from Raman spectroscopy. [2] It is notable that none of the CMC19 models has any 60° bond angles, and the vast majority of the bond angles are narrowly distributed, between 90° and 135°, as shown in Fig. 4.2(b). Together with the structure factor, the bond-angle distribution and its RMS width play an important role in determining the structural quality of tetrahedral

Table 4.2: Comparison of CMC19 models with the best available models (of *a*-Si) in the literature. Symbols have the same meaning as in Table 4.1. E_g and bond angles are expressed in the unit of electron-volt (eV) and degree, respectively.

Unrelaxed CMC19 models								
Model	N	$\langle\theta\rangle$	$\Delta\theta$	c_4	c_2	c_3	c_5	E_g
CMC19	216	109.12	10.68	99.07	0	0.93	0	1.14
CMC19	300	109.14	10.56	99.33	0	0.67	0	1.06
CMC19	512	109.19	10.70	98.44	0	1.56	0	0.88
CMC19	1000	109.13	11.15	99.10	0.30	0.60	0	0.56
Ab-initio-relaxed CMC19 models								
Model	N	$\langle\theta\rangle$	$\Delta\theta$	c_4	c_2	c_3	c_5	E_g
CMC19	216	109.08	10.95	100	0	0	0	1.18
CMC19	300	109.16	10.19	99.33	0	0.67	0	1.39
CMC19	512	109.14	10.61	99.22	0	0.78	0	1.09
CMC19	1000	109.08	11.43	99.10	0.30	0.40	0.20	0.76
Total-energy-based models								
Model	N	$\langle\theta\rangle$	$\Delta\theta$	c_4	c_2	c_3	c_5	E_g
BMW3 [§]	512	109.14	10.36	100	0	0	0	1.32
SWMD	512	109.27	9.12	99.22	0	0.39	0.39	1.01
MLMD [†]	512	109.19	9.69	98.44	0	0.78	0.78	NA
AIMD [‡]	64	108.32	15.5	96.60	0	0.20	3.20	NA

[§] From Ref. [23].
[†] From Ref. [25].
[‡] From Ref. [58].

amorphous semiconducting networks.

Further characterization of the models is possible by examining the local degree of tetrahedrality of the amorphous networks. While the average bond angle, $\langle\theta\rangle$, and its width, $\Delta\theta$, provide an overall measure of the tetrahedral character of a network, the tetrahedral order parameter (TOP), Q_i, at a site i, and its distribution, $T(Q_i)$, gives a precise local measure of the tetrahedral order. The local TOP can be written as, [134]

$$Q_i = 1 - \frac{3}{8}\sum_{\{jik\}}\left(\cos\theta_{jik} + \frac{1}{3}\right)^2, \ \langle Q\rangle = \frac{1}{N}\sum_i Q_i, \tag{4.3}$$

where the symbol $\{jik\}$ stands for the sum over all possible nearest-neighbor angles subtended at the site i. It has been observed that the electronic quality of a model depends on $T(Q_i)$, $\Delta\theta$, and the concentration of coordination defects. [24] In particular, the local TOP is sensitive to the presence of floating bonds (i.e., 5-fold-coordinated atoms), and the existence of dangling bonds (i.e., 3-fold-coordinated atoms) is readily reflected in the electronic

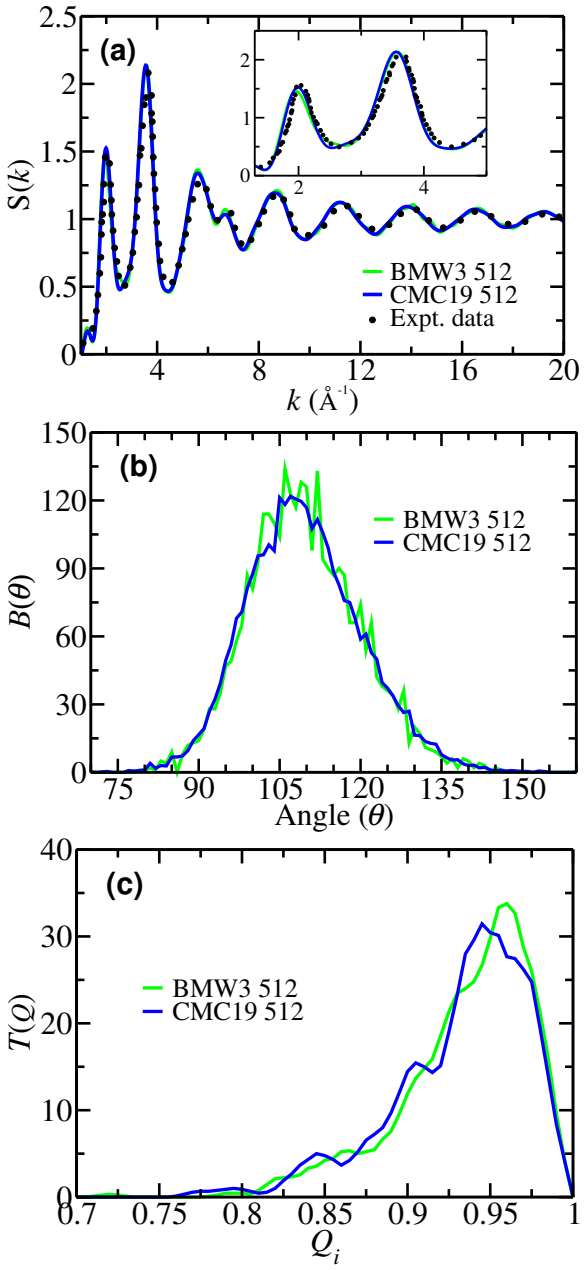

Figure 4.2: Structural properties of *a*-Si from CMC19 models. (a) The structure factor of a 512-atom CMC19 model (blue) and a 512-atom BMW3 model (green). Experimental data (black) correspond to as-deposited samples from Laaziri *et al.* . An enlarged view of the first two peaks is shown in the inset. (b) The bond-angle distribution, $B(\theta)$, for a CMC19 model (blue) and a BMW3 model (green) of identical size. (c) The distribution, $T(Q_i)$, of the local tetrahedral order parameter, Q_i, for a CMC19 model, along with its BMW3 counterpart of identical size. The results presented here in (a)-(c) are all averaged over five (5) independent configurations.

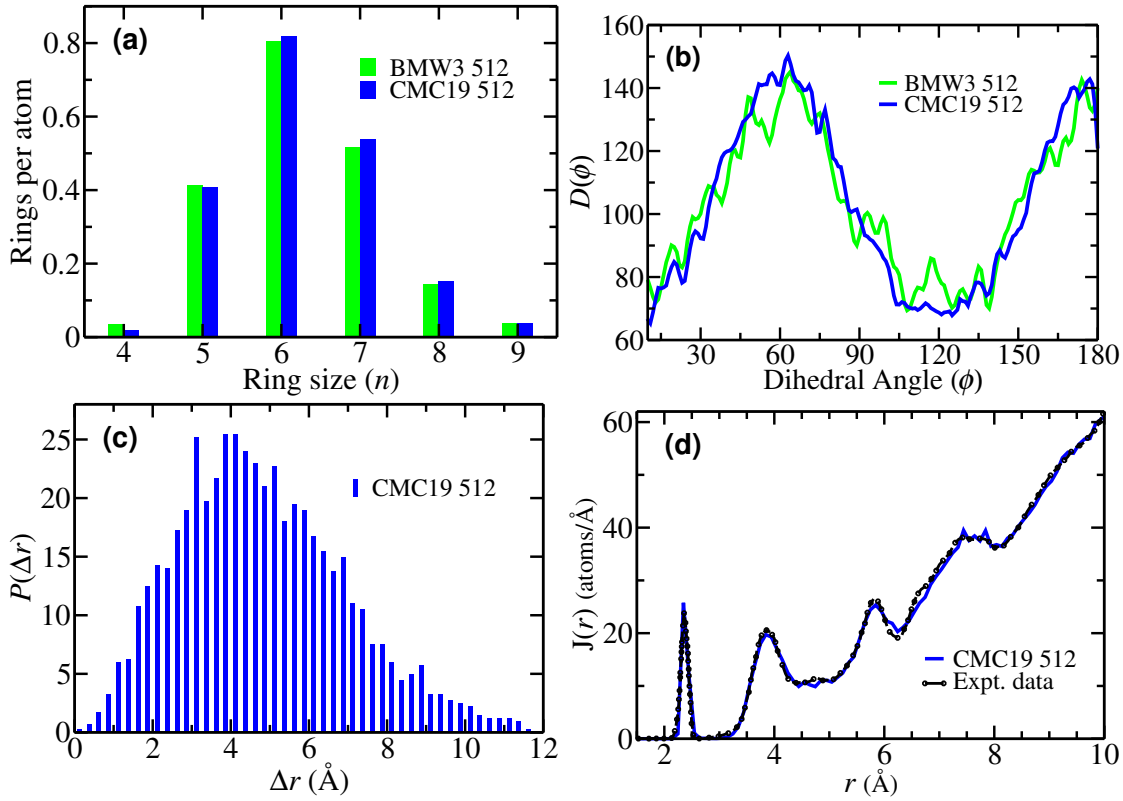

Figure 4.3: (a) The statistics of irreducible rings for CMC19 and BMW3 models. (b) The dihedral-angle distribution, $D(\phi)$, from a CMC19 model and its BMW3 counterpart, showing the characteristic dihedral peaks for tetrahedral ordering near 60° and 180°, and dip at 120°. (c) The distribution of the resultant displacements of atoms during CMC19 simulations for a 512-atom model. See text for details. (d) The radial distribution function, (RDF), J(r), for the 512-atom CMC19 model and experimental data obtained from as-deposited samples of *a*-Si reported by Laaziri *et al.* .

density of states near the Fermi level as defect states. A comparison of $T(Q_i)$ in Fig. 4.2(c) clearly establishes the similarities between an CMC19 model and a BMW3 model, as far as the degree of local tetrahedrality is concerned. This observation is consistent with the statistics of n-fold coordination numbers, c_n, given in Table 4.2. The marked similarities between the CMC19 and BMW3 models, obtained from two distinctly different approaches, are indeed remarkable in view of the fact that the former do not include any information from a total-energy functional.

Having discussed the local structural properties of the models, we shall now address to what extent the atomistic structures on the medium-range length scale resemble or differ from those of the BMW3 models. This is particularly relevant for CMC19 models, as the constraint functions in Eq. (4.1) do not carry any information beyond the first nearest-neighbor

distance, and the experimental two-body correlation data, $F_{ex}(r;\mathbf{R})$, may not be sufficient to include the characteristic structural properties associated with higher-order correlation functions. We address this by examining the topological connectivity of the networks, which involves irreducible rings of various sizes and the dihedral-angle distribution. Intuitively speaking, given the local tetrahedral character of the network, the distribution of n-member rings ($n \geq 4$) provides some information about the atomistic structure on the medium-range length scale, whereas the dihedral-angle distribution should exhibit some characteristic features of a (reduced) four-body correlation function. Figure 4.3(a) shows the distribution of irreducible rings, of sizes from $n = 4$ to $n = 9$, from an CMC19 model and a BMW3 model of equal size. It is apparent that, despite the absence of a total-energy functional, the CMC19 models exhibit similar topological connectivity as that for the BMW3 models. Likewise, the dihedral angles, involving a chain of four consecutive nearest neighbors, are also found to be distributed in a similar way for the CMC19 and BMW3 models in Fig. 4.3(b). These results collectively suggest that the two models are atomistically similar as far as the topological connectivity and the dihedral angles, involving the first few neighbors on the length scale of 3–6 Å, are concerned. In this context, it is appropriate to note that, during CMC19 simulations, structural formation takes place via the rearrangement of the great majority of atoms (about 92%) within the first four neighboring shells, over a radial distance of up to 8 Å. This is evident from Fig. 4.3(c), where the distribution, $P(\Delta r)$, of the resultant atomic displacements, Δr, is plotted. Here, $\Delta r = |\mathbf{r}_f - \mathbf{r}_i|$ and $\mathbf{r}_i$ and $\mathbf{r}_f$ indicate the initial and final positions of an atom at the beginning and end of simulations, respectively. In other words, Δr indicates the magnitude of the resultant displacement of an atom during the entire course of an CMC19 run. Figure 4.3(c) indicates that a considerable number of atoms moved from their initial position at the beginning of the simulation to the final position at the end of the simulation via total atomic displacements as high as 10 Å. Since the resultant displacements associated with the accepted MC moves are mostly governed by the objective function in Eq. (4.1), it is not surprising that the radial atomic correlation can develop up to a distance of the maximum displacement (i.e., ≈ 10 Å) of the atoms. This observation is indeed reflected in the radial distribution function (RDF), as seen Fig. 4.3(d), where the radial correlations between atomic pairs have been found to extend up to a distance of 10 Å or more.

4.3.3 Electronic properties of amorphous silicon from CMC19

While structural properties of model networks provide a wealth of atomistic information, the most compelling evidence of the accuracy and the reliability of a purely information-driven method, and the resulting structures therefrom, come from its ability to produce

the correct electronic properties, obtained without the use of any total-energy functionals during structural formation. For predictive simulations of complex disordered materials using experimental data and information only, it is of crucial importance to establish the 'thermodynamic' stability of the models. An effective inverse approach must thus be able to produce structural configurations that sit close to a stable local minimum of an appropriate total-energy functional. However, these primal issues were ignored in earlier RMC studies by overemphasizing the importance of pair-correlation or structure-factor data, and the resulting effects on the three-dimensional structure associated with these one-dimensional data. Although a few RMC studies [32, 99, 100, 116] on *a*-Si/*a*-Ge did report a narrow bond-angle distribution or a high concentration of four-fold atomic coordination, those results were obtained at the expense of one or the other. Consequently and unsurprisingly, none of the models from previous studies could produce a gap in the electronic spectrum, either due to a high concentration of coordination defects or due to the presence of considerable disorder in the bond-angle distribution of atoms, leading to either a gapless electronic spectrum or a spectrum with a pseudo-gap. It is therefore necessary to examine the electronic density of states (EDOS) of the unrelaxed CMC19 models in order to establish that the models are indeed stable prior to structural relaxation and that they exhibit an electronic gap in the spectrum (see Table 4.2).

Figure 4.4(a) show the EDOS of a 512-atom CMC19 model near the band-gap region before (upper panel) and after (lower panel) *ab initio* structural relaxation. Here, we employed the first-principles density-functional code SIESTA, [80] using double-zeta basis functions and the generalized-gradient approximation (GGA). [79] It is evident that the unrelaxed CMC19 model can produce the correct electronic density of states in the vicinity of the electronic-gap region. Aside from a few defect states, indicated as vertical red lines in Figs. 4.4(a) and 4.4(b), the CMC19 model produces a clean spectral gap that constitutes a major outcome of this study, previously unreported in the literature. A typical defect state (at -3.472 eV) near the Fermi level is shown in Fig. 4.4(c). The state is primarily originated from two dangling bonds (DBs) in real space, which are shown in Fig. 4.4(d) in red color. A few neighboring atoms with secondary contribution are also indicated in green color. A few defect states that appeared in the band-gap region can be readily passivated by adding a minute amount of hydrogen. This is illustrated in Fig. 4.4(b). The lower panel of Fig. 4.4(b) depicts the hydrogen-passivated EDOS for the unrelaxed, i.e., *static* 512-atom CMC19 model, obtained by placing eight (8) H atoms near Si dangling bonds. Hydrogen atoms were so added that the local tetrahedral arrangement of the DBs was minimally perturbed and the silicon-hydrogen bond length was restricted to a distance of 1.55 ± 0.05 Å. The passivation of the Si DBs by H atoms in the static 512-atom CMC19 model yields a clean electronic

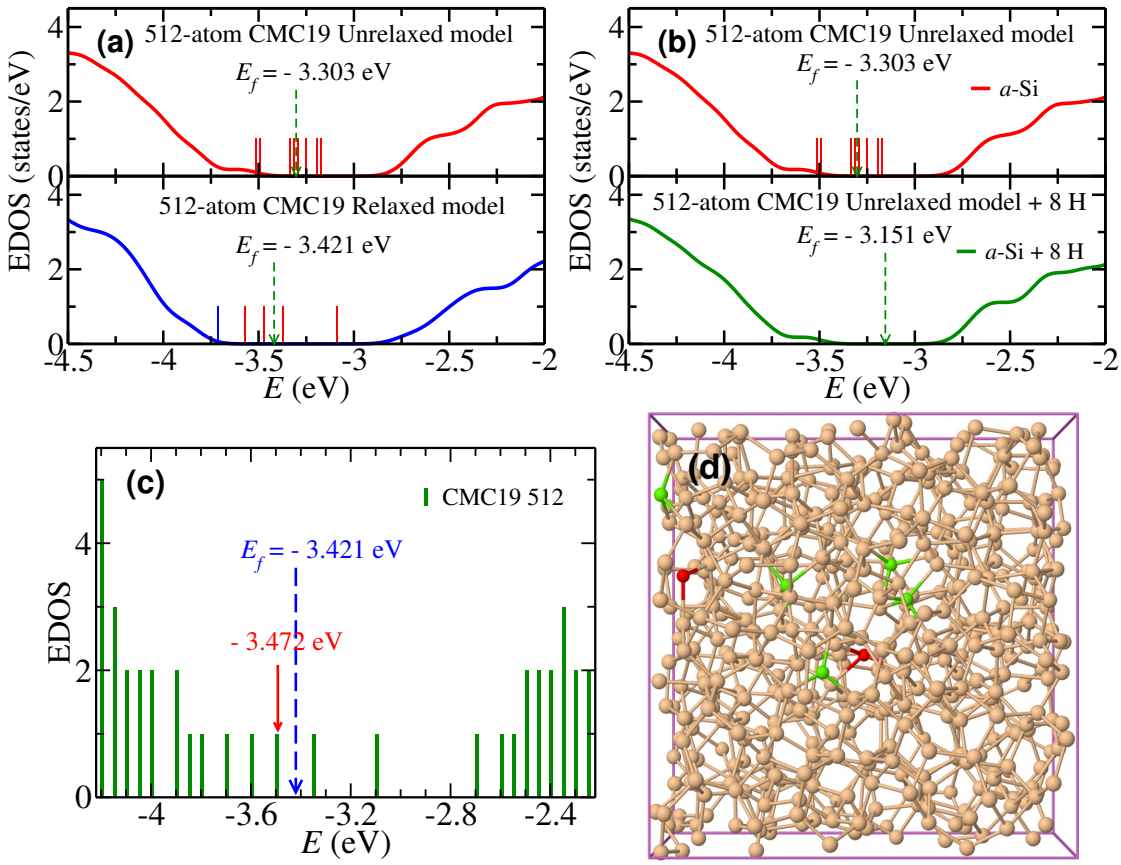

Figure 4.4: Electronic density of states (EDOS) of *a*-Si near the band gap. (a) The EDOS of *a*-Si before (upper panel) and after (lower panel) *ab initio* relaxation of the CMC19 model. A few defect states (red) and a band-edge state (blue) are shown as vertical lines in the gap region. (b) The formation of a clean electronic gap in the unrelaxed 512-atom CMC19 model via hydrogenation. The upper and lower panels correspond to the EDOS before and after H passivation, respectively. (c) A defect state at -3.472 eV and (d) the associated dangling bonds (i.e., 3-fold-coordinated sites) (red) in real space. The other contributing sites, with 4-fold coordination, are indicated in green color.

gap of size 0.85 eV, without *ab initio* total-energy relaxations, which leads to a high-quality model of *a*-Si:H with 1.54 at. % of hydrogen. This procedure can be readily generalized to obtain device-quality models of *a*-Si:H, with a varying concentration of hydrogen. Thus, the CMC19 approach presented in this chapter is equally effective in producing models of hydrogenated amorphous silicon.

Since the EDOS near the valence and conduction bands is highly susceptible to disorder and the presence of coordination defects, particularly dangling bonds and the RMS width of bond angles, the presence of a clean gap in the electronic spectrum is often considered as the most stringent test of the electronic quality of a model. Until recently, with the exception

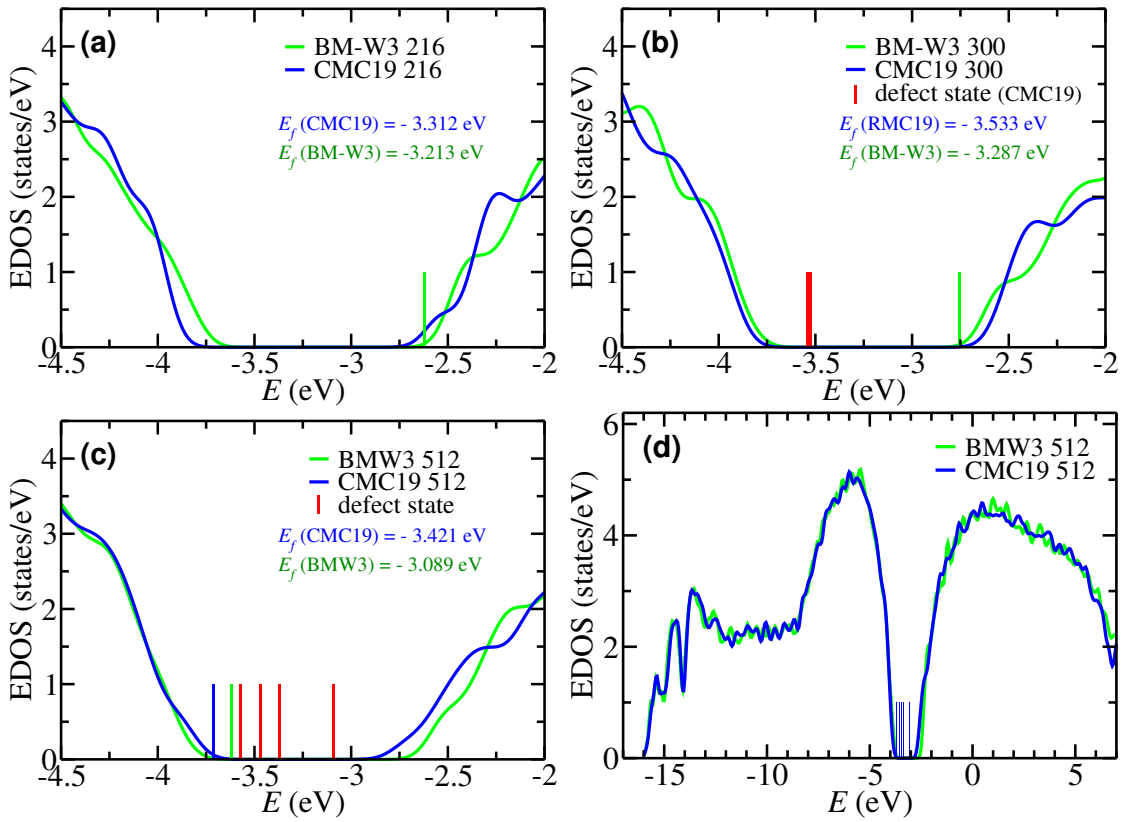

Figure 4.5: Electronic densities of states for *a*-Si from CMC19 models. (a) A 216-atom CMC19 model and its BMW3 counterpart. (b) A 300-atom CMC19 model and BMW3 model, along with a few defect states (red) from the CMC19 model, whereas the green vertical lines correspond to the edge states for the BMW3 model. (c) A 512-atom CMC19 model and BMW3 model, along with a few defect states (red) and band-edge states (blue and green). (d) The full EDOS of *a*-Si for a 512-atom CMC19 model and a BMW3 model. The vertical lines (blue) in the gap region indicate defect states.

of the BMW3 models, there exist no models that can exhibit a clean spectral gap in the electronic density of states. It is remarkable that the information-driven CMC19 models with 216 atoms and 300 atoms exhibit a pristine gap, and those with 512 atoms and 1000 atoms yield a nearly clean gap, in the EDOS (see Figs. 4.5(a)-(d) and Table 4.2), even though no total-energy functional was employed during the course of minimization of the objective function. A comparison of E_g values in Table 4.2, obtained before and after total-energy relaxation of the CMC19 models, firmly establishes that the data-driven CMC19 models are energetically stable and the latter indeed represent the correct structural solution that one strives to obtain from *ab initio* MD simulations of *a*-Si.

The full EDOS for the 512-atom CMC19 model is presented in Fig. 4.5(d), along with the results from the corresponding BMW3 model. The EDOS from these two models

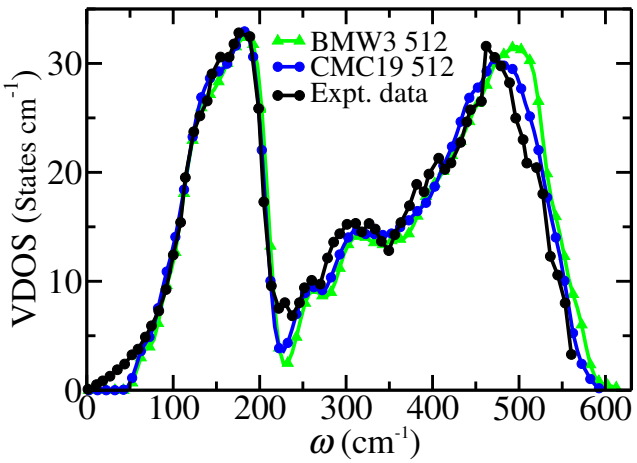

Figure 4.6: Vibrational densities of states from a 512-atom CMC19 and a 512-atom BMW3 model. Experimental data (black) shown here are from inelastic neutron-scattering measurements.

practically matches point-by-point, except for a few points near the conduction-band edge, as shown in Fig. 4.5(d). This minor deviation can be partly attributed to a slightly higher value of $\Delta\theta$ for the 512-atom CMC19 model compared to its BMW3 counterpart. The value of the electronic gap, E_g, reported in Table 4.2, was computed by ignoring the defect states in the electronic spectrum. This was achieved by examining each of the states in the vicinity of the gap region and determining whether it originated from coordination defects in real space or not. Similarly, the vibrational excitations from a 512-atom CMC19 model, which crucially depend on the local atomic structure, have been found to agree well with those from a BMW3 model of equivalent size and experiments. This is evident from Fig. 4.6, where the vibrational density of states (VDOS) for a 512-atom CMC19 model, a 512-atom BMW3 model, and experimental data from inelastic neutron-scattering measurements from Ref.[123] are presented for comparison. The computed values of the VDOS, obtained from the harmonic approximation of dynamical matrices, match very well with those from experiments and the BMW3 model. A small deviation below 50 cm^{-1} can be attributed to finite-size effects. Assuming a linear dispersion relation, which (generally) holds in the limit $k \to 0$, one may expect that the normal-mode frequencies below a characteristic frequency ($\omega_c \propto k_c$) would be absent in finite-size models, owing to the presence of a lower wavevector cutoff ($k_c \approx \frac{4\pi}{L}$). Additional minor deviations from experimental data near 225 cm^{-1} may have originated from the application of the harmonic approximation in the computation of the VDOS.

4.3.4 Microstructure of realistic samples of *a*-Si: Modeling vacancies and voids via CMC19

In the preceding sections, we have discussed the structural, electronic and vibrational properties of *a*-Si, obtained from almost idealized CRN models. As discussed in the Method section, the microstructure of realistic samples of *a*-Si prepared in laboratories can be rather complex, depending upon the growth conditions, the method of preparation, and the history of the samples, and may not be described adequately using the simplistic CRN model of *a*-Si. However, unlike conventional MD and MC methods, the CMC19 approach presented here can effectively address a number of microstructural properties of *a*-Si, such as voids and vacancy defects. We now discuss these properties by analyzing *a*-Si models, which are characterized by the presence of voids and vacancy-type defects observed in laboratory-grown samples of *a*-Si.

The results for 300-atom and 512-atom models using the modified objective function in (4.2) confirm that the approach is very useful to describe microstructural properties of *a*-Si, starting from a random configuration. Figures 4.7(a) and 4.7(b) show the network structure of a 300-atom CMC19 model with a single void of radius of 4 Å before and after *ab initio* total-energy relaxation, respectively. The silicon atoms on the surface of the void, between radii 4 Å and 6 Å, are shown in red color for visual clarity. The structural stability of the void is reflected in Fig. 4.7(b), which is found to remain intact during total-energy relaxations. This observation demonstrates that one may include voids of varying sizes in the amorphous matrix of *a*-Si/*a*-Ge so that the void-volume density is consistent with the experimentally observed value of 0.02–0.3%, depending upon the method of preparation and conditions.

The vacancy-type defects can also be incorporated in a similar manner by producing an array of microvoids of radius 3–4 Å. This is illustrated in Figs. 4.7(c)-(d) by adding two isolated monovacancies in a 512-atom CMC19 model during the course of the CMC19 simulations. The vacancy regions are shown in Fig. 4.7(c) by light blue (left) and green (right) atoms, which are at distance of up to 4 Å from the center of the respective vacancy. The vacancy centers are indicated in Fig.4.7(c) by two small (hypothetical) red spheres, which are separated by a distance of 9 Å. The fact that these regions truly represent monovacancies, and not microvoids, can be readily verified by placing a silicon atom at the center of each vacancy and relaxing the resulting (512+2)-atom model using *ab initio* total-energy functionals. It is evident from Fig. 4.7(d) that the addition of two Si atoms passivated the pair of vacancies by restructuring the local regions at or near the vacancy sites, which led to the formation of a defect-free four-fold-coordinated local network. The atoms within a

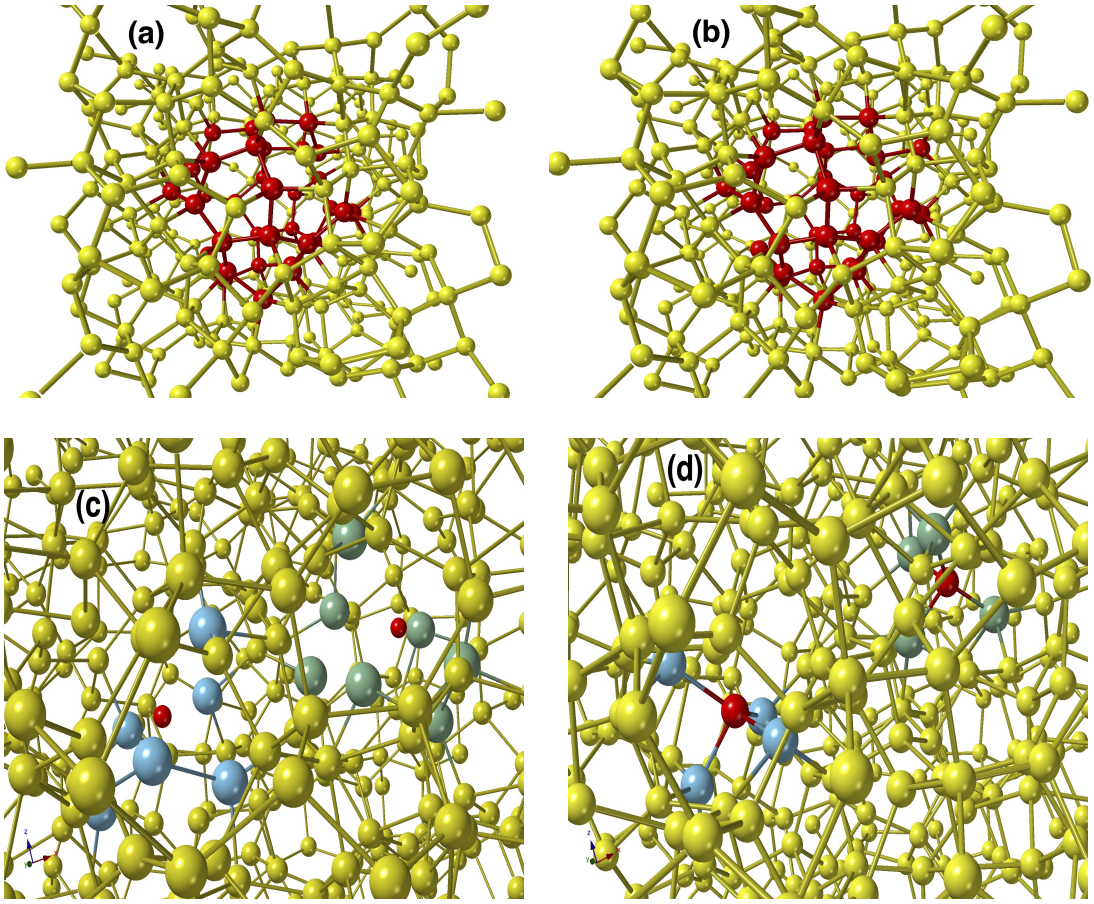

Figure 4.7: Formation of vacancies and voids in *a*-Si via CMC19. (a) A 300-atom CMC19 model with a void of radius 4 Å at the center. The atoms on the void surface (of width 2 Å) are shown in red color. (b) The same model after *ab initio* total-energy relaxation, showing the structural stability of the void. (c) A 512-atom CMC19 model with two monovacancies, separated by a distance of 9 Å. The blue (left) and green (right) colors indicate the atoms within the region of 4 Å from the center of the respective vacancy, which is indicated by a small red sphere. (d) The *ab-initio*-relaxed 514-atom model obtained by adding a silicon atom (red) at the center of each vacancy in Fig. 4.7(c). The formation of a local 4-fold-coordinated network at/near the vacancy sites establishes that the vacancy region corresponds to a monovacancy site. The missing Si atoms are shown in red color.

radial distance of 3.2 Å from the vacancy centers, are shown as light blue and green atoms. Thus, the pair of isolated vacancies in Fig. 4.7(c) can be viewed as originating from the missing two Si atoms, shown in Fig. 4.7(d) in red color, which are separated by a distance of 9.17 Å in the *ab initio*-relaxed model. The electronic density of states of the 300-atom CMC19 model with a void at its center is shown in Fig. 4.8. It may be noted that the presence of such 1–2% vacancy-type defects in annealed samples of *a*-Si was suggested in Ref. [115] in order to explain the observed value of the average coordination number

of 3.88 from X-ray diffraction.The presence of too many coordination defects in MD or other models is often justified by quoting the average coordination number of 3.88, obtained from the RDF of annealed *a*-Si samples in Ref. [115]. However, a direct comparison with results from finite-size models would be incorrect as it leads to an isolated dangling-bond density of about 12%, which is neither compatible with ESR and IR measurements nor with the observed electronic density of states of *a*-Si. A more plausible explanation is the presence of vacancy-type defects and few microvoids in *a*-Si, which leads to an average coordination number of 3.88 in annealed samples. In summary, using an augmented form of the objective function, the data-driven CMC19 methodology not only provides a means to generate accurate structural models of *a*-Si/*a*-Ge but also to include microstructural properties of the materials observed in experiments without employing any total-energy functionals and forces.

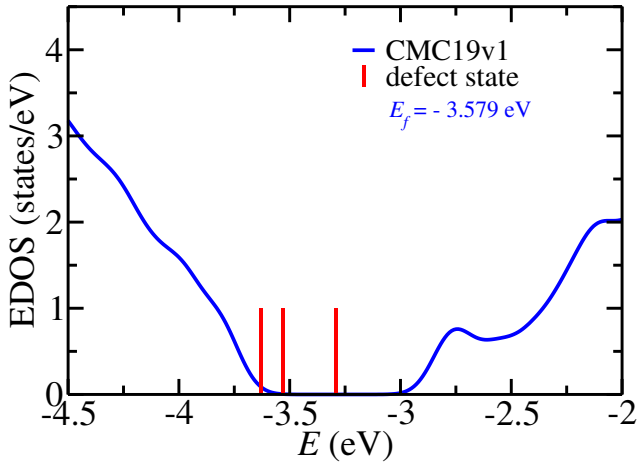

Figure 4.8: The EDOS of a 300-atom CMC19 model with a central void of radius 4 Å (see Fig. 4.7(b). The defect states, shown as vertical lines (red), in the gap region originated from three dangling bonds present in the ab initio-relaxed model. The Fermi level is located at -3.579 eV.

4.4 Conclusions

In this chapter, we present a purely data-driven constraint Monte Carlo (CMC19) approach that can produce accurate structural models of tetrahedral amorphous semiconductors without employing a total-energy functional but using diffraction data and local structural information only. By posing the material-structure determination as an inferential problem and addressing the problem as an optimization program, we have shown that the problem can be solved by inverting diffraction data to generate a three-dimensional structural solution,

using Monte Carlo methods. Owing to its dependence on local information, the approach can be implemented efficiently using an order-N algorithm for the evaluation of the cost function of a system consisting of N atoms. An examination of the unrelaxed CMC19 models and their *ab-initio*-relaxed counterparts shows that the former sits very close to a stable local minimum of a quantum-mechanical total-energy functional, indicating the thermodynamic stability of the information-driven CMC19 models. The hallmark of this new constraint-driven order-N approach is that it has the ability to produce 100% defect-free model configurations of amorphous silicon, as exemplified by a 216-atom model. Comparisons of structural, topological, electronic, and vibrational properties of the models with those from experiments revealed that the CMC19 models are structurally, topologically, and electronically accurate. The salient features of the models include a narrow bond-angle distribution, with an RMS deviation of 9–11.5°, and an ultra-low defect concentration below 1%, which enables the models to exhibit a clean electronic gap of size 0.8–1.4 eV. To our knowledge, none of the RMC or RMC-derived inverse and hybrid models in the literature so far, which employ diffraction data and a total-energy functional, can produce the aforementioned structural and electronic properties as accurately as the CMC19 models. The information-based CMC19 approach presented here not only can produce overall structural and electronic properties but also the microstructural properties of realistic samples of a-Si from experiments, such as voids and vacancy-type defects, which cannot be addressed directly using currently available computational methods. This observation heralds the resolution of the long-standing problem of uniqueness in the structural determination of tetrahedral amorphous semiconductors via inversion of diffraction data, in particular a-Si, without employing a total-energy functional. The study demonstrates that information-driven inverse approaches not only can enhance existing methodologies for modeling disordered materials, but also offer a directional step change in materials computation and radically different approaches to the structural determination of disordered materials, based on an information paradigm.

Chapter 5

AB INITIO HYDROGEN DYNAMICS AND MORPHOLOGY OF VOIDS

The work presented in this chapter has been published in **Biswas, P. & Limbu, D. K.** *Ab Initio* **Hydrogen Dynamics and the Morphology of Voids in Amorphous Silicon** *physica status solidi (b)*, 2000494 (2021).

5.1 Introduction

Hydrogen plays an important role in the electronic and optical properties of amorphous silicon (*a*-Si) [13]. While the addition of a small amount (about 6–12 at. %) of hydrogen in *a*-Si is particularly beneficial for producing device-grade samples of *a*-Si:H, via passivation of coordinating defects (e.g., 3-fold-coordinated Si atoms or dangling bonds), the presence of too much hydrogen in *a*-Si can be detrimental to the electronic and optical properties of *a*-Si:H-based devices. Thin films of *a*-Si:H are often employed for surface passivation of crystalline silicon, which is useful for the generation of high open-circuit voltages in silicon-heterojunction solar cells [135]. A relatively high hydrogen content, in void-rich environment of *a*-Si:H, is preferred for this purpose to achieve high-quality *a*-Si:H/*c*-Si interfaces [136], indicating the benevolent role of H in *a*-Si. By contrast, the structure of *a*-Si:H is altered by the light-induced creation of metastable defect states, known as the Staebler-Wronski effect (SWE) [137], which adversely affects the performance of *a*-Si:H-based solar cells. Nuclear magnetic resonance (NMR) studies [138] on *a*-Si:H samples have indicated that the motion of H atoms, which are produced by the light-induced breaking of Si-H bonds, plays an important part in recovering the photovoltaic stability of the affected *a*-Si:H samples upon annealing at 350°–400° C [139]. Thus, an understanding of the motion of H atoms in *a*-Si in the presence of inhomogeneities is of crucial importance to address the photovoltaic stability of *a*-Si:H upon light irradiation.

While a number of earlier theoretical/computational studies on the microstructure of hydrogen distributions in *a*-Si:H [33, 61, 107, 109, 140, 141] have focused on the silicon-hydrogen bonding configurations in the bulk network environment of *a*-Si and their effects on structural, electronic, and optical properties of the material, there exist only a few computational studies that directly address the role of non-bonded hydrogen (NBH) and

voids on the network structure of *a*-Si:H [106, 109, 142]. Sekimoto et al. [42] have recently shown experimentally that the presence of large amount of non-bonded hydrogen (e.g., H_2 molecules inside voids) can broaden the vacancy-size distribution and enhance the size of the optical gap [143] in *a*-Si. The density of *a*-Si:H has been also found to be somewhat dependent on the number of NBH, and hence on the distribution of hydrogen inside nanometer-size voids. Following our recent studies on the temperature-induced nanostructural evolution of voids in *a*-Si [141], and its effect on the intensity of small-angle X-ray scattering (SAXS) [132], the present study focuses on accurate calculations of the atomistic dynamics of hydrogen inside voids obtained from the density-functional theory. The emphasis here is on the dynamical aspects of hydrogen motion inside voids on the time scale of several picoseconds at low and high temperature in the environment of a varying concentration of H atoms. The formation and dissociation of Si–H bonds on the surface of voids are discussed from a kinetic point of view. The movement of H atoms inside nanometer-size voids and its resulting effects on the hydrogen microstructure and the reconstruction of the void surfaces are also addressed in this study.

The presence of voids in the amorphous matrix suggests that, for an accurate determination of the motion of H atoms within a void, one must take into account the inhomogeneities in the electronic charge distribution in the vicinity of void surfaces. The standard protocol in density-functional calculations advises us to address the problem by computing the self-consistent-field (SCF) solution of the Kohn-Sham (KS) equation, and the presence of voids suggests that the generalized-gradient approximation (GGA) should be employed in order to deal with the atomic density fluctuations near the void surfaces. We shall therefore address the problem using the GGA and compare the results with those from the local density approximation (LDA). The presence of weak dispersion forces, which are often included via the Van der Waals corrections, are not taken into account in this study owing to the computational complexity of the problem and the somewhat limited accuracy of local basis functions that we have used in this study.

The rest of the chapter is organized as follows. Section 5.2 provides a short description of the method for generating *a*-Si models with hydrogenated voids, using the Wooten-Winer-Weaire (WWW) method and *ab initio* molecular dynamics simulations (AIMD). The results are discussed in sec. 5.3, with an emphasis on the dynamics of H atoms inside voids in sec. 5.3.1, kinetics of Si–H bond formation and dissociation in sec. 5.3.2, and the microstructure of the hydrogen distribution for a varying number of hydrogen atoms in sec. 5.3.3. A brief discussion on the shape of the voids is also provided in sec. 5.3.3. This is followed by the conclusions of the study in sec. 5.4.

5.2 Method

For AIMD simulations of hydrogen dynamics inside voids in *a*-Si, we started with four independent 1000-atom models of *a*-Si, obtained from the WWW method [22, 23]. A spherical void of radius 5 Å was created at the center of each model and the geometry of the resulting structure was thoroughly relaxed, using the first-principles density-functional code SIESTA [80]. A number of models with a hydrogenated void were then produced by adding 10, 20, and 30 H atoms inside the central cavity so that the mass density of the final models is about 2.22 g.cm^{-3}. A single void of radius 5 Å corresponds to a number density of 4.82×10^{19} voids.cm^{-3} and a void-volume fraction of 2.52 at. %, which are close to the values reported in experiments [48, 144]. The H atoms were initially distributed in such a way that they were at a distance of at least 2 Å from Si atoms and 1 Å from each other. The silicon atoms within the spherical region of radius between 5 Å and 8 Å from the center of the voids are labeled as the void-surface atoms for the analysis of the void surface upon annealing and total-energy optimization of the systems. Figure 5.1 shows a schematic diagram of a void embedded in a two-dimensional amorphous network of *a*-Si. A gray circular region of radius $R_v = 5$ Å is a void region that is surrounded by a layer of Si atoms (green) with a thickness d. Silicon atoms in the layer constitute the surface/wall of the void, which we shall refer to as the void-surface atoms. The remaining Si atoms, within the cubic box of length L, will be referred to as bulk Si atoms and are indicated as yellow circles. The effective width of the void surface is chosen to be about $d = 3$ Å. This is based

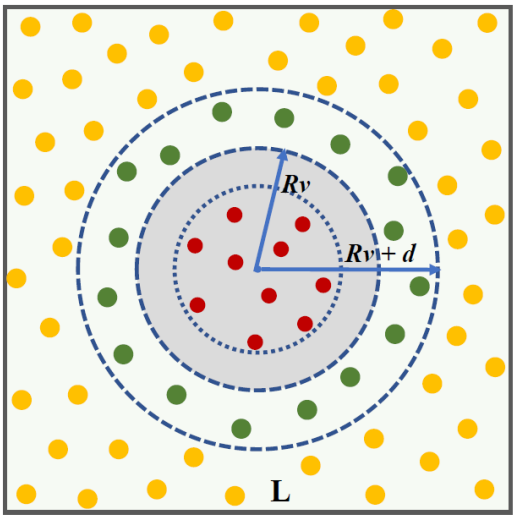

Figure 5.1: A schematic representation of a void (gray region) in two dimensions. The annular region with Si atoms (green) indicates the void boundary, with a few H atoms (red circles) inside the void. The rest yellow atoms are the bulk Si atoms.

on the results from the test calculations at 700 K, which show that the majority of silicon atoms near the void surface can move up to a distance of 2.5–3.0 Å. This distance is roughly equal to the first nearest-neighbor distance between Si atoms in the amorphous environment. For structural analysis of voids, we thus use a void-surface region of 8 Å.

To study hydrogen diffusion and the microstructure of hydrogen distribution on the void surfaces, AIMD simulations were performed at 400 and 700 K to examine the temperature dependence of H dynamics and the resulting effects on the morphological structure of the void surfaces, using the density-functional code SIESTA. SIESTA employs local basis functions, based on numerical pseudoatomic orbitals [145], and the norm-conserving Troullier-Martins pseudopotentials [114] in order to obtain the self-consistent-field (SCF) solution of the Kohn-Sham equation in the density-functional theory. Electronic and exchange correlations between electrons were taken into account via the LDA and the GGA, by using the Perdew-Zunger [77] and the PBE [79] parameterizations for the LDA and the GGA, respectively. Owing to the computational complexity of the problem involving a large number of atoms and the necessity for simulating a reasonably long-time dynamics for studying the equilibrium distribution of H atoms, using the SCF solution of the KS equation, the AIMD simulations were conducted using the single-zeta (SZ) basis functions for Si atoms and the double-zeta-polarized (DZP) basis functions for H atoms. The high computational cost associated with the calculation of total energy and forces restricts us to use SZ basis functions for Si atoms during the course of AIMD simulations. The subsequent total-energy optimizations, however, were conducted using the double-zeta (DZ) basis functions for Si atoms until the total force on each atom was less than or equal to 5×10^{-3} eV.Å^{-1}. During AIMD simulations, the temperature of the system was controlled in NVT ensembles by using the Nosé thermostat [146], and a time step of 0.8 fs was used to ensure that the movement of light H atoms can be described accurately at the high temperature of 700 K. The evolution of the system was monitored and recorded for a total time of 20 ps. The simulation procedure was repeated for each of the four independent models with a void at the center, indicated by M1 to M4 hereafter, for a hydrogen load of 10, 20, and 30 H atoms per void. In each case, we have used a different random distribution of H atoms within the void in order to gather as much as statistics as possible. The final results were obtained by averaging over four independent configurations.

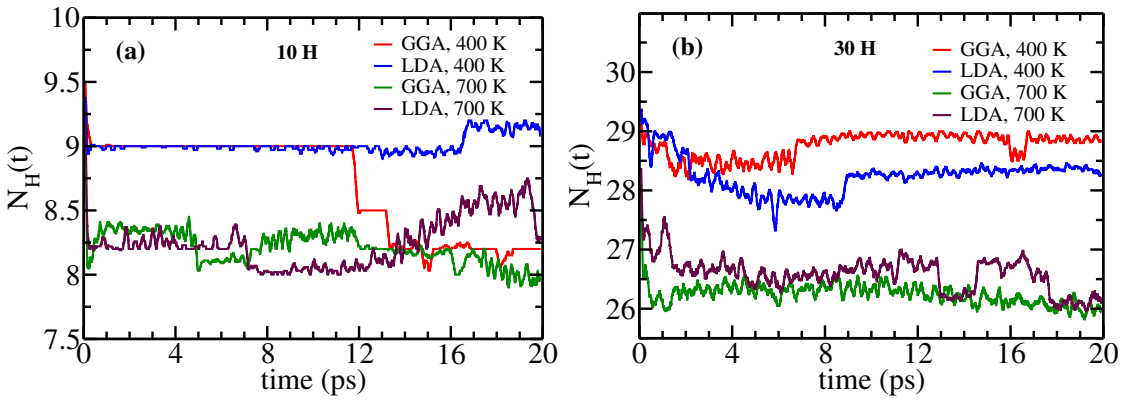

Figure 5.2: The time evolution of the average number of H atoms (including H_2 molecules) within a void at 400 and 700 K. The results correspond to a hydrogen load of: (a) 10 H atoms per void; (b) 30 H atoms per void. The average is taken over 4 voids for each temperature from independent simulations.

5.3 Results and Discussion

5.3.1 Hydrogen dynamics inside voids in *a*-Si

In this section, we discuss the results from the density-functional calculations for studying the dynamics of H atoms/molecules inside voids in *a*-Si. To this end, we mostly focus on those H atoms/molecules which are within the cavity during the entire course of simulations at a low and high temperature of 400 and 700 K, respectively. Figure 5.2 shows the time evolution of the average number of H atoms (molecules included) within a void-surface region of radius 8 Å at 400 and 700 K. The results correspond to two different values of the hydrogen load, 10 and 30 H atoms per void, and are obtained by averaging over 4 independent voids/models using the LDA and GGA. At 400 K, the great majority of H atoms stayed within the void, with the exception of one or two H atoms that left the void-surface region of radius 8 Å. The LDA and GGA dynamics exhibit a more or less similar behavior at a given temperature, although the GGA tends to knock out one or two more H atoms outside the cavity for high H loads at 700 K (see Fig. 5.2b). Despite limited statistics, it would not be inappropriate to conclude that, on average, the LDA and GGA do not differentiate much as far as the (average) number of H atoms leaving the voids at 400 K is concerned.

To study the effect of the hydrogen load on the mean-square displacement (MSD) of H atoms at the low and high temperature of 400 and 700 K, respectively, we have examined the variation of the MSD with time for 10, 20, and 30 H atoms per void using the GGA. Once again, the results were obtained by averaging over 4 independent voids and are presented in Fig. 5.3. The results (in Fig. 5.3) lead to the following observations. Firstly, the MSD of H

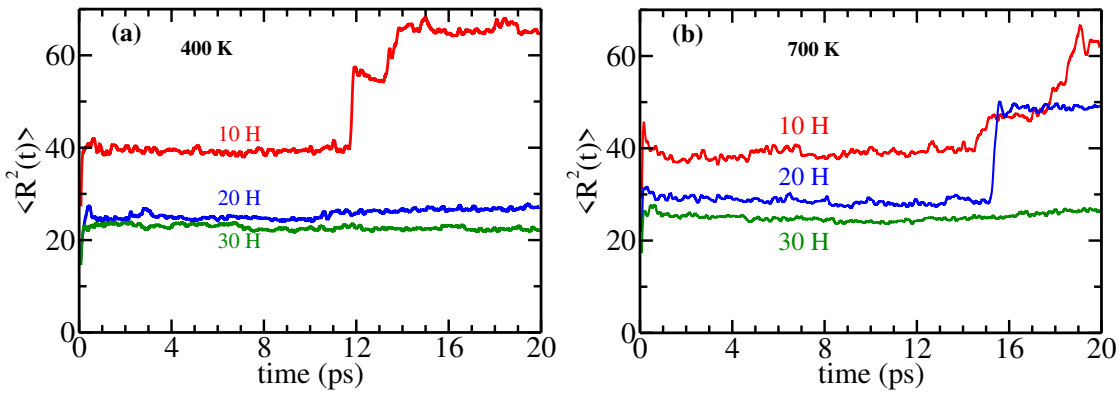

Figure 5.3: The variation of the mean-square displacement (MSD) of H atoms, averaged over *all hydrogen* in four models, with time for three different hydrogen loads as indicated: (a) 400 K; (b) 700 K. The results were obtained from the self-consistent-field calculations with the GGA, and averaged over 4 independent voids for each H load and temperature.

atoms decreases with an increasing presence H atoms within the voids. This is particularly so as the hydrogen load increases from 10 H atoms per void to 30 H atoms per void. This reduction in the MSD is due to the decrease of the average distance between any two H atoms within the cavity for an increasing presence of hydrogen within the same volume. Secondly, the sharp rise of the MSD for a hydrogen load of 10 H atoms per void near 12 ps at 400 K can be attributed to a hydrogen atom leaving the void. For a hydrogen load of 10 H atoms per void, H atoms can move somewhat more freely than those with a load of 20 or 30 H atoms per void. This makes it possible for few H atoms to diffuse rapidly in the vicinity of the void surface, and eventually to escape the void region – and the simulation cell in one or two cases – depending upon the temperature of the system. In contrast, the presence of too many H atoms for a high value of H load can impede the diffusion process and thus reduces the MSD at a given temperature. Thirdly, the motion of H atoms are affected by the temperature of the system as well. This is evident in Fig. 5.3(b), where the MSD for a load of 20 H atoms per void was observed to increase at 700 K during 15 to 16 ps and it continued to remain so until the end of the simulation at 20 ps. This observation contrasts with the case of 30 H atoms per void at the same temperature, where none of the H atoms was found to leave the void but remained within a root-mean-square (RMS) distance of 5 Å from the center of the void. Finally, one may note that the available statistics do not permit us to comment on the dynamical behavior of few H atoms that diffuse out of the cavity at an earlier time (e.g., the H atom in Fig. 5.3(a) for a hydrogen load of 10 atoms per void), based on the results from 4 configurations. The movement of H atoms is driven by a combination of factors, such as the concentration of H atoms in a void, temperature, and the disorder in

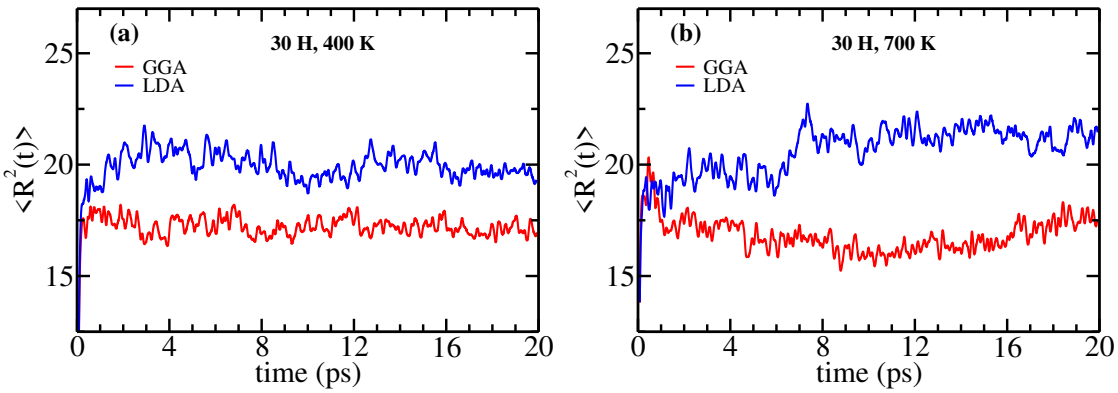

Figure 5.4: The time evolution of the MSD of H atoms *within* voids for a hydrogen load of 30 H atoms per void in the LDA (blue) and the GGA (red). The results for 400 and 700 K are shown in (a) and (b), respectively.

the atomic distribution on the void surfaces. Since we are not particularly interested in the dynamical behavior of few H atoms that escape the void-surface region of 8 Å, we will not discuss this further.

Having discussed the variation of the MSD with respect to the hydrogen load, we now address to what extent the exchange-correlation (XC) approximation may affect the motion of H atoms inside the voids as far as the MSD is concerned. Figure 5.4 shows the evolution of the MSD with time for a hydrogen load of 30 H atoms per void at 400 and 700 K. Since we are interested in the dynamics of H atoms inside the void, and the resulting hydrogen microstructure of the void surface, the MSD was computed using only those H atoms that were *inside* the void region of radius 8 Å for the entire duration of simulation. The plots in Fig. 5.4 suggest that the LDA slightly overestimates the MSD (of H atoms) compared to the value obtained from the generalized-gradient approximation (GGA). The RMS values of the displacement of H atoms inside the voids in the LDA and the GGA at 400 K have been found to be about 4.5 Å and 4.15 Å, respectively. A more or less similar observation applies to the high-temperature dynamics at 700 K, as shown in Fig. 5.4(b). It thus appears that the MSD of the H atoms within the void is not particularly strongly affected by the XC approximation at 400 and 700 K. This is due to the fact that the majority of H atoms within a void reside as bonded hydrogen (to Si atoms) on the void surface, mostly in the form of Si–H configurations, and few Si–H_2 configurations, along with a few H_2 molecules within the cavity. Since the calculation of the MSD excludes a few mobile H atoms that have already left the void region, the remaining bonded H atoms (on the void-surface) show a more or less converged value of the MSD during the course of simulations. Thus, in a sense, a more or less converged value of the MSD (in Fig. 5.4) is reflective of the distribution of bonded H

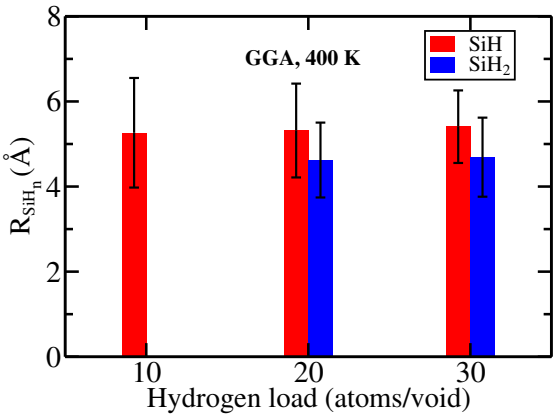

Figure 5.5: The average (radial) distances of SiH and SiH_2 bonds on the void surface from the center of the void. The dihydride SiH_2 bonds have been found to form on the walls of the voids at a distance which is closer to the center of the void than their SiH counterpart.

atoms on the walls of the void. We shall see later that a slightly larger value of the MSD of H atoms that we observe here for the LDA case (see Fig. 5.4) results from a minor expansion of the void surface in the LDA calculations. Following Sekimoto et al. [42], one may conclude that the expansion originates from the stress on the void surface due to the presence of a significant number of Si–H bonds in the LDA calculations. Finally, it may be mentioned that the dihydride Si–H_2 configurations are found on the void surface at a distance, which is closer to the center of the void than their monohydride (Si–H) counterpart. Figure 5.5 shows the average distances of the Si–H_2 and Si–H bonding configurations, which are located on the walls of the voids, from the center of the voids for the GGA at 400 K. This observation is consistent with the results reported by Kageyama et al. [121] from dielectric measurements.

We now briefly discuss the diffusion of a few highly mobile H atoms. Earlier in this section, we have seen that the MSD of H atoms can increase occasionally very rapidly for a hydrogen load of 10 and 20 H atoms per void. This behavior of the MSD has been attributed to the movement of few H atoms out of the void region, defined by a sphere of radius 8 Å. It has been observed that such a steep rise of the MSD (e.g., see Fig. 5.3(a) at 12 ps) originates from the high mobility of few H atoms inside the hydrogenated voids. Figure 5.6 shows the plot of the instantaneous kinetic energy (KE) of H atoms at 400 K, obtained from using the GGA for a period 20 ps. The distribution of the KE values along the *y* axis for a given H atom indicates the range and the frequency of the kinetic energy of the atom during the course of AIMD simulations. An analysis of the real-space trajectory of the H atoms in the vicinity of the void region in models M2 and M3, and the results from Fig. 5.6 revealed that a few highly mobile H atoms, such as H7 in Fig. 5.6(a) and H17 in Fig. 5.6(b), left the void region sometime during the course of simulations. This observation was found to be true for

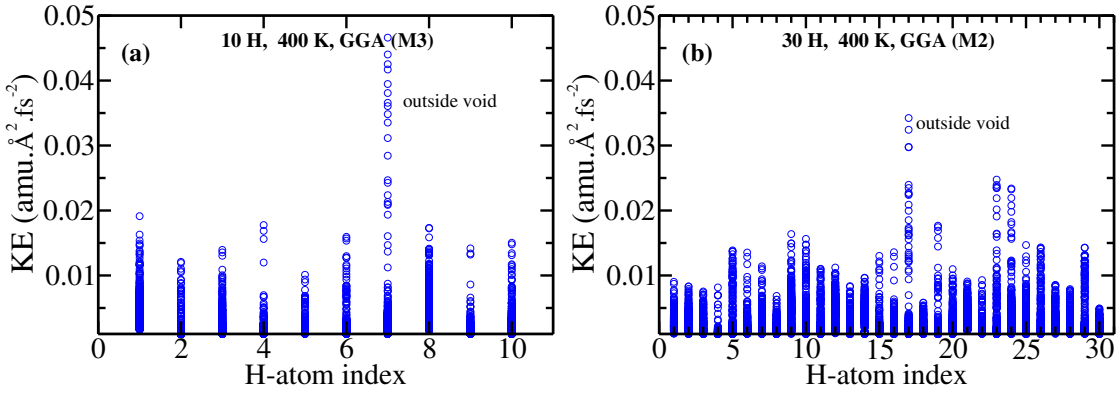

Figure 5.6: The instantaneous kinetic energy (KE) of H atoms in two voids (in models M2 and M3) at 400 K, obtained from the GGA. The results for the void with a hydrogen load of (a) 10 H atoms per void, and (b) 30 H atoms per void. The atoms with the largest KE, H7 (left panel) and H17 (right panel), are found to diffuse out of the void region. The range and the frequency of KE values are indicated by the numbers and shading (of blue circles) along the *y* axis, respectively.

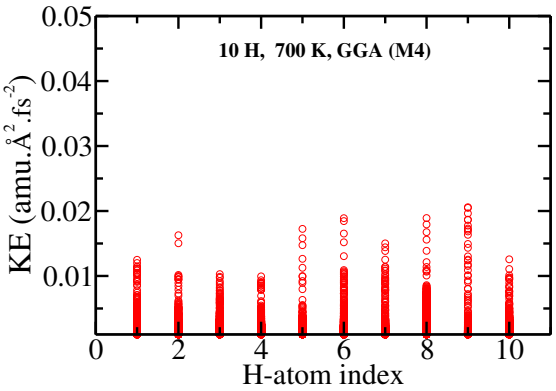

Figure 5.7: The distribution of kinetic energy (KE) along the *y* axis for H atoms inside a void (in model M4) at 700 K. The range and the frequency of KE values are indicated by the numbers and shading (of red circles) along the *y* axis, respectively.

other voids as well, where H atoms were observed to leave the void region due to their high kinetic energies. Conversely, we have noticed that all the H atoms in model M4 remained inside the void throughout the course of simulation even at the high temperature of 700 K. The results obtained from M4 are shown in Fig. 5.7, where the KE values of the H atoms are found to be considerably lower than those presented in Fig. 5.6.

5.3.2 Kinetics of Si–H bond formation and dissociation on the surface of voids

We now address a question of considerable importance concerning the kinetics of Si–H bond formation and dissociation on the surface of voids in *a*-Si. While a complete understanding

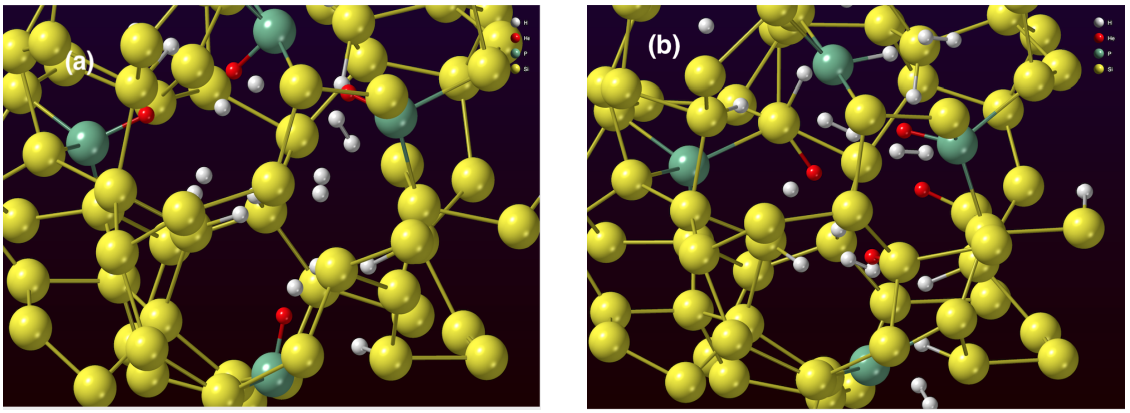

Figure 5.8: The kinetics of Si–H bond formation and dissociation at 700 K for a hydrogen load of 30 H atoms per void obtained from the GGA in model M4. (a) The Si–H bonds that dissociated during AIMD simulations are shown as green-red pairs at 3 ps. (b) The H atoms (red) resulted from the dissociation of SiH bonds diffused through the void-surface region to form new Si–H bonds, which are indicated as yellow-red pairs at 18 ps. The presence of a green-red pair suggests that the Si–H bond broke and formed again, but with another (dissociated) H atom.

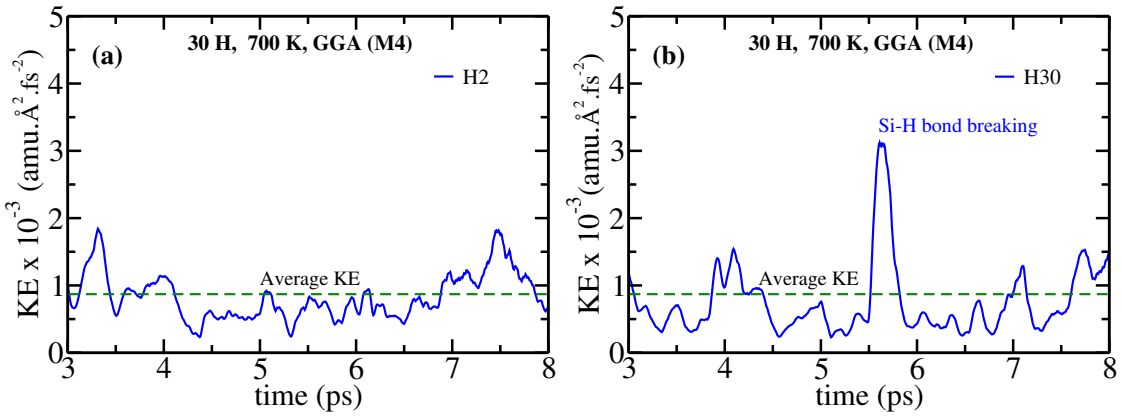

Figure 5.9: The evolution of the kinetic energy (KE) of two H atoms, H2 and H30, in monohydride Si–H bonds at 700 K. (a) The KE of H2 atom is found to stay below the average KE at 700 K for most of the simulation time. (b) The Si–H bond involving the high-energy H30 atom dissociates near 5.5 ps and forms a new Si–H bond shortly thereafter. The average KE of H atoms at 700 K is indicated as a dashed horizontal line (green). The KE values correspond to a (central) moving average over a window of 100 fs.

of these events requires the computation of bond formation and dissociation energies, and the knowledge of the potential-energy surface associated with Si–H bonding configurations, the problem can be addressed approximately by considering the kinetic energy of H atoms in AIMD simulations.

Earlier, in Fig. 5.4, we have seen that the mean-square displacement (MSD) of H atoms

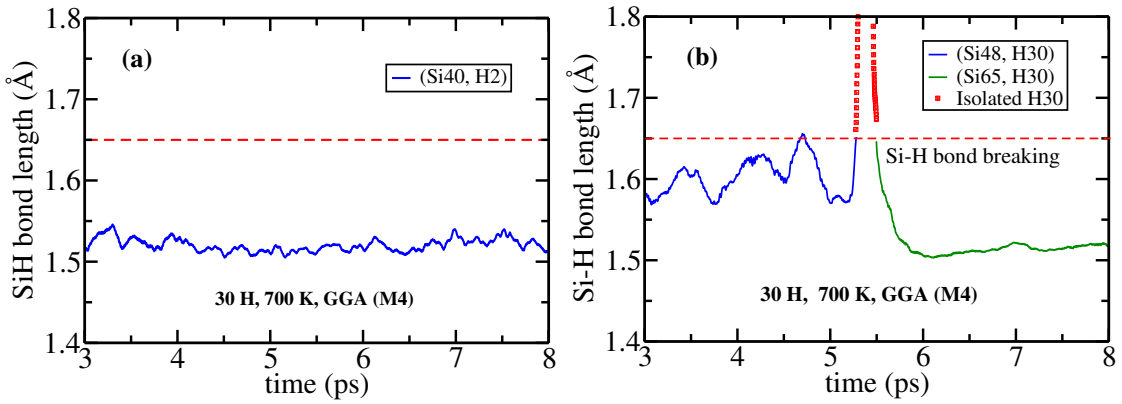

Figure 5.10: (a) The variation of the bond length of a stable monohydride pair (Si40, H2) with time. (b) The dissociation of a monohydride Si–H bond during MD simulations. The Si–H bond associated with the pair (Si48, H30) breaks at 5.35 ps, which is followed by the formation of a new pair (Si65, H30) at 5.56 ps. The isolated state of H30 atom is indicated by red squares, where the 'bond length' refers to the distance between H30 and the nearest Si atom. The cutoff value of the Si–H bond length, 1.65 Å, is indicated by a dashed horizontal line (red).

inside the voids fluctuates within the range of 17–22 Å^2, depending upon the LDA or GGA. The MSD values are indicative of the fact that the great majority of H atoms stay bonded to Si atoms on the void surface as the time evolution of the system continues. However, it has been observed that a few H atoms in Si–H bonds can break free of the surface and move through the cavity to form new Si–H bonds at nearby active Si sites. This behavior is particularly pronounced at 700 K for a hydrogen load of 30 H atoms per void, where the presence of few H atoms with high kinetic energy makes it possible to dissociate an existing Si–H bond and form a new Si–H bond in the vicinity of the void surface. This is illustrated in Fig. 5.8, which shows the snapshots of two silicon-hydrogen bonding configurations in the vicinity of the void in M4, obtained from the GGA at 3 ps and 18 ps. Figure 5.8(a) shows a set of four Si–H bonds, involving H12, H16, H24, and H30, indicated as green-red pairs, at 3 ps, which are found to dissociate later during simulation. The breaking of Si–H bonds is reflected in Fig. 5.8(b), which shows that the H atoms (red) resulted from the dissociation of four Si–H bonds moved through the void and formed new Si–H bonds. The latter are shown as yellow-red pairs, with the exception of one where a dissociated H atom (red) is found to be bonded with an active Si site (green). The dissociation of Si–H bonds at 700 K can be understood from a kinetic point of view. Figure 5.9 shows the time evolution of the kinetic energy (KE) of two H atoms, H2 and H30, bonded to silicon atoms, Si40 and Si48, respectively, as monohydride Si–H bonds. As the simulation proceeds, the KE values fluctuate around the average translational KE value of $3k_B$T/2 at temperature T, where k_B

is the Boltzmann constant. However, the large kinetic energy of H30 atom at around 5.5 ps, which is about three times larger than the average KE at 700 K, leads to a rupture of the Si–H bond and subsequent formation of a new Si–H bond with a silicon atom in the vicinity of the void. By contrast, H2 forms a stable Si–H bond due its low kinetic energy during time evolution of the system. We have verified that the remaining three H atoms – H12, H16, and H24 – exhibit a similar behavior as H30 as far as the KE values are concerned.

The dissociation of Si–H bonds due to high KE values of H atoms can be observed by tracking the Si–H bond length of a dissociated pair with time. Figure 5.10 shows the evolution of Si–H bond lengths associated with the pairs (Si40, H2) and (Si48, H30). The pair (Si48, H30) breaks at 5.35 ps, which is followed by the formation of a new pair (Si65, H30) at 5.56 ps, but the low-energy pair (Si40, H2) continues to stay bonded during its evolution. The variation of the bond length of the (dissociated) pair before and after dissociation are shown in Fig. 5.10(b). The transient isolated state of H30, between 5.35 ps and 5.56 ps, is shown as red squares, where the 'bond length' corresponds to the distance between H30 and the nearest Si atom in the void region. It goes without saying that the dissociation and subsequent formation of Si–H bonds on the void surface do not affect the MSD values of the H atoms as long as the H atoms stay within the cavity through the formation of new bonding configurations.

5.3.3 Hydrogen microstructure and morphology of voids in *a*-Si

The discussion in the preceding sections so far is mostly confined to the dynamics of H atoms inside the voids and to what extent the motion of H atoms is affected by the exchange-correlation approximation and the hydrogen load inside the voids, as far as the MSD of H atoms is concerned. We now examine the microstructure of hydrogen distributions on void surfaces and the morphological character of the voids, which result from the movement of hydrogen and silicon atoms in the vicinity of the voids for a varying hydrogen load. In particular, we discuss the formation of various bonded hydrogens (BH) and non-bonded hydrogens (NBH), as well as the restructuring of the void surfaces during annealing at 400 and 700 K, with an increasing concentration of H atoms within voids, and the dependence of hydrogen microstructure on the LDA and GGA. The BH and NBH play an important role in characterizing the structural and optical properties of *a*-Si:H [42, 107, 143]. These properties can be studied experimentally using an array of experiments, such as positron-annihilation lifetime (PAL) spectroscopy [42], Rutherford backscattering spectrometry (RBS) [143], hydrogen-effusion measurements [147, 148], and Fourier-transform infrared spectroscopy-attenuated total reflections (FTIR-ATR) [149].

Table 5.1: Statistics of bonded and non-bonded hydrogens inside voids for varying hydrogen loads. The tabulated values indicate the amount of H atoms (in per cent of total H) that resides in voids as isolated hydrogen (H_{iso}), H_2 molecules, and SiH/SiH_2 bonds. Hydrogen atoms outside the void region are listed as Ex_H. Asterisks denote the actual number of isolated H atoms.

H load	XC	H_{iso}	H_2	SiH	SiH_2	Ex_H
			400 K			
10	GGA	0	15.0	67.50	0	17.50
	LDA	0	10.0	82.50	0	7.50
20	GGA	0	32.50	47.50	10.0	10.0
	LDA	0	25.0	62.75	5.0	7.50
30	GGA	0	45.0	40.0	11.67	3.33
	LDA	0	28.33	47.50	18.33	5.83
			700 K			
10	GGA	0	25.0	55.0	0	20.0
	LDA	0	0	77.50	5.0	17.50
20	GGA	0	27.50	45.0	12.50	15.0
	LDA	0	17.50	66.25	2.50	13.75
30	GGA	0.83 (1*)	35.56	41.11	8.89	13.33
	LDA	1.65 (2*)	16.67	56.67	11.67	13.33

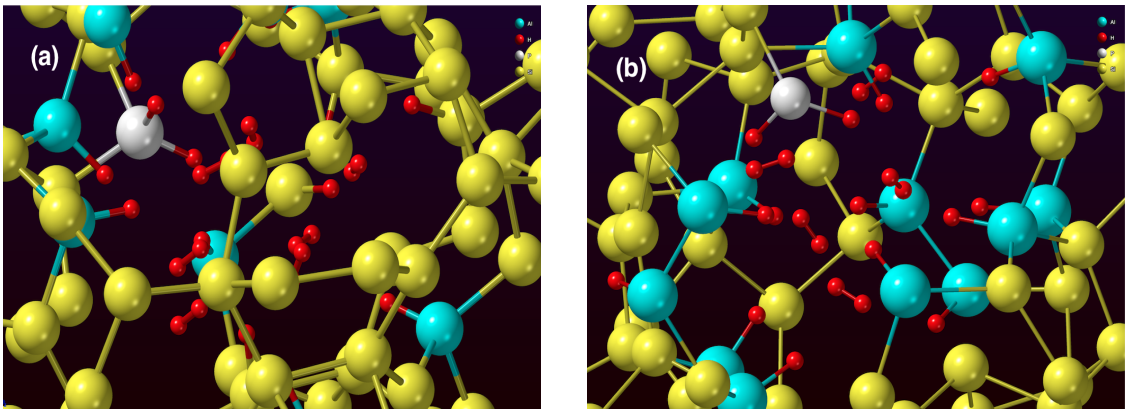

Figure 5.11: Hydrogen-bonding configurations, including H_2 molecules, in a void-surface region of radius 8 Å for a hydrogen load of 30 H atoms per void at (a) 400 K and (b) 700 K from the GGA in model M4. Silicon atoms associated with monohydride (SiH) and dihydride (SiH_2) configurations are shown in cyan and white colors, respectively, whereas bonded H atoms and molecules are shown in red color.

Table 5.1 lists the statistics of various silicon-hydrogen bonding configurations and non-bonded hydrogens, e.g., H_2 molecules and one or two isolated H atoms, near the void,

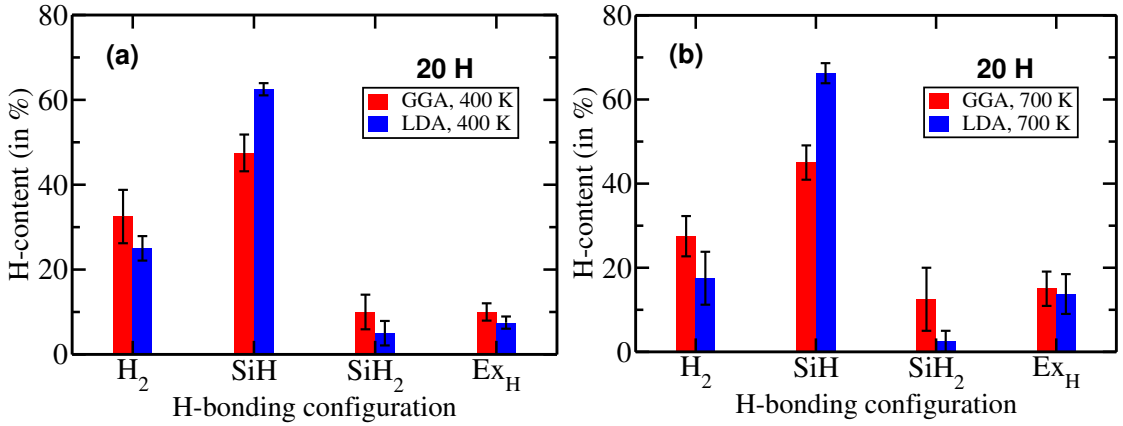

Figure 5.12: Histograms showing the content of H atoms (in at. %) in bonded and non-bonded hydrogens in the vicinity of voids in *a*-Si for a hydrogen load of 20 H atoms per void at 400 and 700 K. The results are obtained by averaging over all models.

defined by a spherical region of radius 8 Å. The presence of isolated H atoms in the network is an artifact (of simulations), which arises from our choice of the cutoff value of 1.65 Å for Si–H bonds. It has been observed that the isolated H atoms at 700 K, listed in Table 5.1, are at a distance of 1.66 Å from the nearest Si atom (for the GGA) and at distances of 1.67 Å and 1.7 Å from the neighboring Si atoms (for the LDA). The results from Table 5.1 and an analysis of the void surfaces for the hydrogen load of 10, 20, and 30 H atoms per void show that the surface of the voids is mostly decorated with monohydride Si–H bonds. A few dihydride Si–H_2 bonds are also spotted for a hydrogen load of 20 and 30 H atoms per void, and a notable amount of hydrogen can be seen to appear inside the voids as H_2 molecules, especially for hydrogen loads of 20 and 30 H atoms per void. It is also evident from Table 5.1 that, in comparison with the GGA, the LDA overestimates the number of SiH bonds but underestimates the count of H_2 molecules. The presence of few SiH_2 bonding configurations makes it difficult to comment on the dependence of SiH_2 configurations on the XC approximation from the available data. Figure 5.11 shows a three-dimensional rendering of Si–H and Si–H_2 bonds in the vicinity of the void surface in M4, along with a few H_2 molecules for a hydrogen load of 30 H atoms per void at 400 and 700 K.

Experimental studies using infrared measurements by Chabal and Patel [52] suggest that the number density of H_2 molecules in nanometer-size voids in *a*-Si is of the order of 10^{21} cm^{-3}. This observation is found to be consistent with the values listed in Table 5.1, which can be roughly translated into 3–13 $\times$ 10^{21} cm^{-3} for the GGA and 2–8 $\times$ 10^{21} cm^{-3} for the LDA at 400 K, assuming a spherical void of radius 5–8 Å and a hydrogen load of 30 H atoms per void. None of the AIMD runs in this study showed any isolated H atoms within

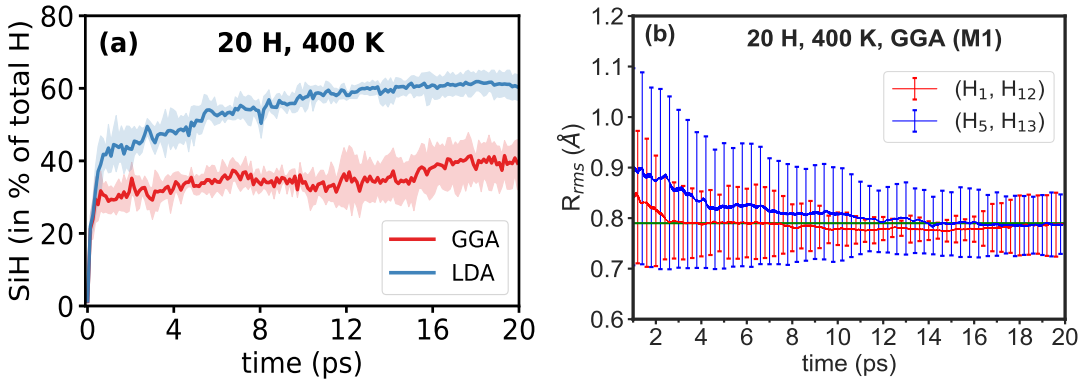

Figure 5.13: (a) The evolution of monohydride Si–H bonds at 400 K in the GGA and the LDA for a hydrogen load of 20 H atoms per void. The y axis indicates the amount of hydrogen atoms (in per cent of total H atoms) that resides in Si–H bonds. (b) The formation of H_2 molecules within a void at 400 K in the GGA for a hydrogen load of 20 H atoms per void. The RMS distance and its standard deviation between two pairs of H atoms, averaged over a moving window of width 200 fs, are shown against time.

the voids, except one or two at 700 K, which are statistically insignificant. As discussed earlier, a few highly mobile H atoms are found to diffuse out of the void region due to high KE values of these atoms. The number of such atoms are listed as Ex_H in Table 5.1. Figure 5.12 summarizes the results from Table 5.1, by showing the number of Si–H, Si–H_2, and H_2 molecules for a hydrogen load of 20 H atoms per void at 400 and 700 K.

Since the restructuring of void surfaces is largely characterized by Si–H bonds on the walls of the voids, it is instructive to examine the formation of these bonds during the course of simulation. Figure 5.13(a) shows the time evolution of the hydrogen content of SiH bonds (in per cent of total H) for a hydrogen load of 20 H atoms per void in the GGA and the LDA at 400 K. The formation of Si–H bonds begins very rapidly within the first few picoseconds and then it gradually converges by 18 ps. The LDA seems to overestimate the number of SiH bonds by about 32%, compared with the same from the GGA (cf. Table 5.1). This notable difference between the LDA and the GGA results indicates the need for choosing an accurate XC functional and a long simulation time for studying the microstructure of SiH and SiH_2 on the walls of the voids. Likewise, the formation of H–H pairs, or H_2 molecules, during annealing is illustrated in Fig. 5.13(b), by plotting the evolution of the RMS distance between two pairs of H atoms at 400 K in the GGA for a hydrogen load of 20 H atoms per void in M1. The first H_2 molecule, consists of (H1, H12), was formed within the first 3 ps, whereas the second one, (H5, H13), was formed at around 14 ps. The RMS distance between the pair of H atoms and the corresponding standard deviation are obtained by averaging over a moving time window of width 200 fs.

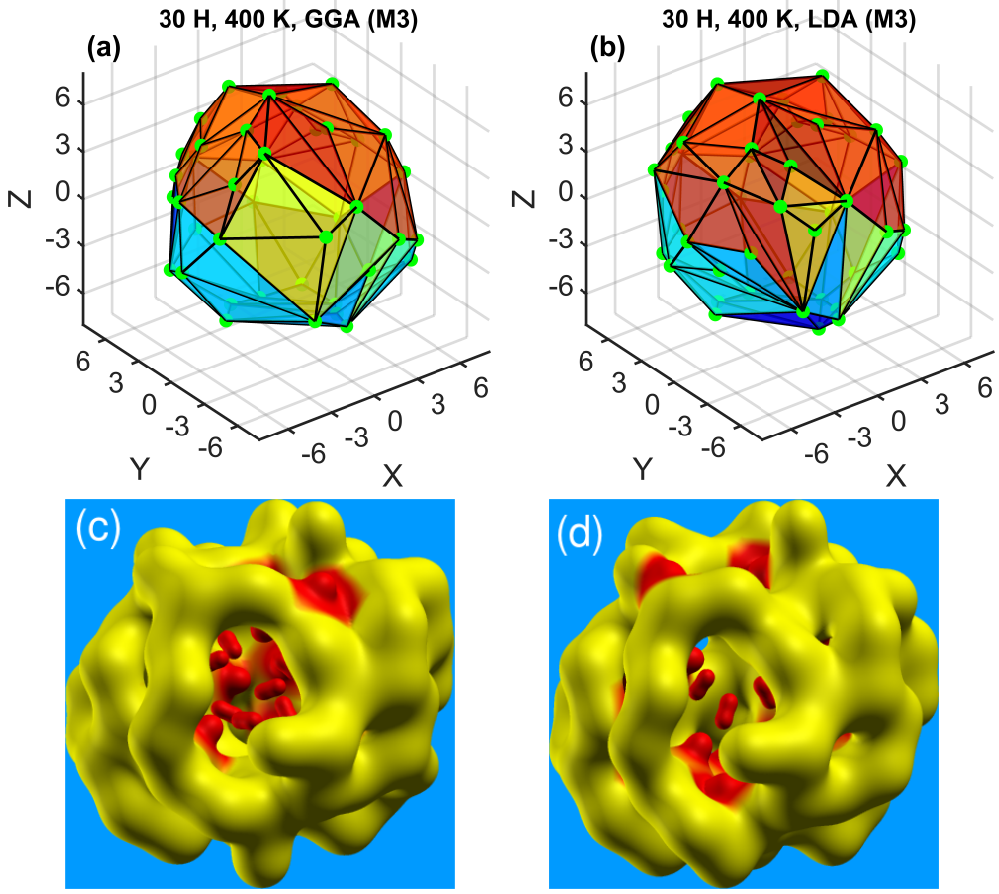

Figure 5.14: The reconstruction of a three-dimensional shape of a void (in M3) from two sets of void-surface atoms at 400 K for a hydrogen load of 30 H atoms per void. The convex polyhedra obtained from the void-surface atoms in (a) the GGA and (b) the LDA, using the convex-hull approximation. The corresponding non-convex surfaces using the same set of void-surface atoms are shown in (c) and (d), respectively. Silicon-hydrogen bonds and H_2 molecules are shown in yellow-red and red-red colors, respectively.

We conclude this section by making the following observation on the linear size and the shape of the voids obtained from annealing and total-energy relaxations in the presence of H atoms. While the linear size of a void can be estimated from the radius of gyration of a set of atoms, which define the void surface, the reconstruction of a three-dimensional shape of a void from a finite set of atomic positions is a nontrivial problem. A somewhat crude but simple and useful approach is to approximate the void shape by constructing the minimal convex polyhedron, or a convex hull, formed by the set of void-surface atoms. The approach assumes that any restructuring of the void surface – caused by the movement of the void-surface atoms – would be reflected in the shape of the convex hull, which is associated with the void region. However, it has been observed [111] that the actual shape of voids can

Table 5.2: Linear (Å) and volumetric (Å^3) measures of the voids, reconstructed from the convex-hull approximation. R_G, R_H, and V_H indicate the radius of gyration, the convex-hull radius, and the volume of the hull, respectively. S and N_H represent the sphericity and the number of atoms on the convex hull, respectively.

H load	XC	R_G	R_H	V_H	S	N_H
			400 K			
10	GGA	6.392	7.162	1275.04	0.884	41
	LDA	6.517	7.205	1305.45	0.888	41
20	GGA	6.416	7.204	1295.95	0.883	41
	LDA	6.566	7.218	1316.80	0.890	42
30	GGA	6.489	7.231	1318.42	0.885	42
	LDA	6.541	7.263	1332.45	0.887	42
			700 K			
10	GGA	6.192	7.102	1242.36	0.883	40
	LDA	6.347	7.175	1287.78	0.887	41
20	GGA	6.365	7.242	1299.63	0.880	39
	LDA	6.461	7.274	1323.15	0.879	39
30	GGA	6.430	7.202	1319.43	0.892	42
	LDA	6.475	7.238	1317.39	0.882	41

be rather complex and non-convex in nature, and it may not be represented accurately by a convex polyhedron. An approximate non-convex surface can be constructed via convolution of the position of the void-surface atoms using three-dimensional Gaussian basis functions and choosing a suitable value of the isosurface parameter for the atomic pseudo-surface of Si and H atoms. The XCRYSDEN [150] package can generate such pseudo-surfaces. A more general discussion on the reconstruction of such non-convex void shapes can be found in Refs. [111, 141].

Figure 5.14 shows the approximate shape of a void with a hydrogen load of 30 H atoms per void (in model M3) obtained from annealing at 400 K, followed by total-energy optimization. The convex polyhedra shown in Figs. 5.14(a) and 5.14(b) correspond to the set of void-surface atoms obtained from the GGA and the LDA, respectively. The respective non-convex shapes of the void, obtained via the convolution of the same set of void-surface atoms using the Gaussian functions centered at the atomic sites, are shown in Figs. 5.14(c) and 5.14(d). Although the polyhedra in Figs. 5.14(a)-(b) appear different, the difference is not particularly noteworthy as far as the hull radius, the convex-hull volume, and the sphericity of the polyhedra are concerned. These values are listed in Table 5.2. The sphericity, S, of an object is defined as the ratio of the surface area of a sphere, A_s, to that of

the object, A, both having an identical volume V. This definition leads to [151],

$$S = \frac{A_s}{A} = \frac{\pi^{\frac{1}{3}}(6V)^{\frac{2}{3}}}{A}.$$

Here, we have used the volume and the corresponding surface area of the convex hull of a void surface to estimate V and A, respectively. A review of S and other values in Table 5.2 suggests that the LDA marginally overestimates the volume of the void, which is evident from the gyrational and hull radii, and the hull volume of the voids for all hydrogen loads and temperatures. This observation is also consistent with the somewhat smaller values of the MSD of H atoms (within voids) that we have observed for the GGA calculations in Figs. 5.4(a)-(b).

5.4 Conclusions

In this chapter, we have studied *ab initio* dynamics of hydrogen atoms inside voids in *a*-Si with an emphasis on hydrogen diffusion and the resulting structure of the void surfaces with respect to a varying concentration of hydrogen at 400 and 700 K. A comparison of the results obtained from the LDA and the GGA reveals that the former considerably overestimates the number of monohydride Si–H bonds but underestimates the presence of H_2 molecules inside the cavities, irrespective of the annealing temperature and the concentration of hydrogen. The surfaces of the voids are found to be primarily passivated with monohydride Si–H bonds and a few dihydride SiH_2 bonds at high concentration of hydrogen. Neither the LDA nor the GGA shows any presence of SiH_3 configurations even for a high concentration/load of 30 H atoms per void. The number densities of the bonded and non-bonded hydrogens observed in this study are found to be consistent with those from the infrared and Rutherford back scattering (RBS) measurements. The study reveals that the kinetics of Si–H bond formation and dissociation during AIMD simulations can be approximately described and understood by considering the (translational) kinetic energy of H atoms inside the voids. Hydrogen atoms with KE values significantly higher than the average KE of the system at a given temperature are found to dissociate from Si–H bonds on the surface of the voids. The resulting isolated H atoms then diffuse through the void region to form new bonds with nearby active Si atoms within a fraction of a picosecond in our simulations. The results also show that a somewhat higher value of the mean-square displacement of the H atoms within voids in the LDA can be attributed to the reconstruction of the void surface through the formation of Si–H bonds. This is also reflected in the linear size of the voids obtained from the convex-hull approximation.

Chapter 6

TRANSITON-METAL CLUSTERS VIA FORCE-BIASED MONTE CARLO AND *AB INITIO* CALCULATIONS

The work presented in this chapter has been published in (i) **Limbu, D. K. & Biswas, P. Structure of transition metal clusters: A force-biased Monte Carlo approach.** *Journal of Physics: Conference Series* **921,** 012010 (2017), (ii) **Limbu, D. K., Atta-Fynn, R., Drabold, D. A., Elliott, S. R. & Biswas, P. Structural properties of transition-metal clusters via force-biased Monte Carlo and** *ab initio* **calculations: A comparative study.** *Physical Review B* **96,** 174208 (2017), and (iii) **Limbu, D. K., Madueke, M. U., Atta-Fynn, R., Drabold, D. A. & Biswas, P.** *Ab initio* **density-functional studies of 13-atom Cu and Ag clusters.** *Journal of Physics: Conference Series* **1252,** 012009 (2019).

6.1 Introduction

In recent years, there has been rapid progress in the development of global optimization techniques, which encompass state-of-the-art evolutionary computing [152] to the population-based swarm intelligence and differential-evolution approaches. [153, 154] Despite this development, Monte Carlo (MC) methods, based on simple Metropolis and related algorithms, continue to play a major role in addressing optimization problems in science and technology. In the context of structural modeling of amorphous solids [31, 32, 130] on the atomistic length scale, the Monte Carlo procedure is particularly useful for optimization of a total-energy functional without any knowledge of atomic forces or local gradients of the energy functional. Since calculations of local gradients are computationally more complex than the evaluation of the total energy of a system, MC methods are often preferred in many optimization problems where local gradients are either not available (e.g., for a discrete or non-smooth optimization problem) or computationally too prohibitive to compute. However, the computational advantage of the MC methods is often offset by their slow convergence behavior, which requires a longer simulation time to produce results with the desired accuracy when compared to the Newton-like and Conjugate-Direction methods. Recent works on structural modeling of amorphous materials using Reverse Monte Carlo (RMC) simulations have indicated that atomic forces can be profitably used in RMC simulations to improve the structural quality of amorphous configurations and the efficiency

of the resultant methods.[36, 98, 116] Toward that end, the main purpose of this chapter is to explore the usefulness of employing local gradients (of a potential) or atomic forces in Monte Carlo simulations and to apply the method in determining the most stable structure of transition-metal (TM) clusters containing several tens of atoms. In this chapter, we present a modified version of the gradient-based Monte Carlo method, originally introduced by Rossky *et al.* ,[67, 155] to optimize transition-metal clusters and compare the results with the putative global minima of the clusters reported in the recent literature.[156–158] In particular, we compare the total energy and structures of the transition-metal clusters of Fe, Ni, and Cu from a force-biased Monte Carlo (FMC) method with those from the Cambridge Cluster Database. The latter provides the structures of the putative global minima of a number of transition-metal clusters obtained by Doye and Wales.[159] These authors employed an improved version of the basin-hopping algorithm of Li and Scheraga [160] to obtain the global minima of a number of transition-metal clusters using Monte Carlo simulations, coupled with Conjugate-Gradient optimizations. In the following, we refer to these clusters as CCD clusters and use them as a benchmark for a comparison of the total energy and structures of Fe, Ni, and Cu clusters obtained from the force-biased Monte Carlo (FMC) simulations presented here. We also examine the stability of the classical FMC structures by perturbing and relaxing the clusters using a first-principles total-energy functional within the framework of the density-functional theory (DFT).

The plan of the chapter is as follows. In Section 6.2, we briefly review the results on the structure of the transition-metal clusters of Fe, Ni, and Cu from classical, semi-classical, and *ab initio* density-functional calculations. Section 6.3 presents the computational method associated with the implementation of atomic forces in Monte Carlo simulations used in this work. The first-principles total-energy relaxation of the structures, using the density-functional code NWChem, [161] is also described in this section. In Section 6.4, we discuss the results from the classical FMC and *ab initio* simulations with particular emphasis on the total energy, the two- and three-body correlation functions, the atomic-coordination numbers, the bond-orientational order parameter, and the three-dimensional distribution of the atoms in the FMC and CCD clusters. This is followed by the conclusion of the work in Section 6.5.

6.2 Structure of transition-metal clusters: An overview

Transition-metal clusters have been studied extensively from computational [157–160, 162–181] and experimental [182–187] points of view. They have potential applications in catalysis,[188–190] magnetic-recording materials,[191] carbon nanotubes, [156, 192] and

biological applications involving genetic sequencing.[193, 194] Theoretical efforts to study transition-metal clusters range from Genetic Algorithms [195–199] and Monte Carlo and molecular-dynamics simulations, using classical [200–205] and semi-classical [162, 206–208] potentials, to *ab initio* density-functional calculations. [167–179, 181] Of particular interest is the structure of Fe clusters obtained from the Finnis-Sinclair (FS) potential,[209, 210] and that of Ni, Cu and clusters bound by the Sutton-Chen (SC) potential.[211] Similarly, the Gupta potential [166] has been extensively used to study the stable isomers and the corresponding geometry of a number of transition-metal clusters in several studies.[201, 205, 212, 213] The putative global minima of Ni and Cu clusters have been studied extensively by Doye and Wales [158] using the Sutton-Chen potential. Likewise, Elliott *et al.* [157] have addressed the computation of the global minima of Fe clusters using the Finnis-Sinclair potential. Transition-metal clusters have been also studied using tight-binding molecular-dynamics (TBMD) simulations.[162, 206–208] Lathiotakis *et al.* [162] studied Ni_n clusters (n=11–55) using TBMD simulations to study the relative stability of the icosahedral and FCC structures and found that the relaxed icosahedral structure was more stable than the cuboctahedral structure for 13-atom and 55-atom clusters. This observation is consistent with the tight-binding studies of Ni and Cu clusters by other researchers, [207, 208] where the most stable structure of M_{13} (M=Ni, Cu) was found to be an icosahedron. An extensive analysis of the results from numerous classical and semi-classical studies appears to indicate a general trend that, at small sizes, the icosahedral motif is the preferred ground-state structure, whereas large clusters tend to adopt the structure of a truncated octahedron and a truncated decahedral structure follows in the intermediate range.[182] This observed trend has been found to be consistent with the thermodynamics of small systems and the shell structure of atoms in clusters, which take into account the internal strain, symmetries or the lack thereof, and the volume and surface dependence of the binding energy of clusters in the formation of stable structures. [182]

While classical and semi-classical approaches can approximately address the evolution of the most stable structure with varying cluster sizes, any electronic effects that arise from the outer shell (valence) electrons of the atoms cannot be treated within these approaches. This is particularly relevant for the transition-metal clusters, where the presence of localized d orbitals can add further complication. For example, recent *ab initio* studies on small Au clusters have shown that the hybridization between $6s$ and $5d$ orbitals, due to strong relativistic effects, can play a significant role in determining the degree of planarity (of a structure), stability, and energetics of Au nanocluster formation.[214, 215]

Ab initio density-functional methods have been used extensively to study transition-metal clusters, especially 13-atom clusters of $3d/4d$ series, in the last two decades. [167–181]

However, the DFT results vary considerably among research groups depending upon the type of the basis functions and the nature of the exchange-correlation (XC) functional employed in the calculations, and the method used to sample candidate structures from the potential-energy surface (PES) during simulations. While a number of low-energy structures have been proposed as possible ground-state structures for 13-atom TM clusters, there is still no consensus among the researchers in the community. Using density-functional calculations, Oviedo and Palmer [169] reported the presence of a number of 'amorphous' low-energy isomers of M_{13} (M = Cu, Ag, and Au) with a total energy difference of 0–1 eV from each other. The authors noted that the cuboctahedral structure was more stable than the icosahedral structure for the ground-state structure of Ag_{13} – an observation which is at variance with the results from recent *ab initio* studies. [174–176, 179] Chang and Chou [170] studied 13-atom clusters of early and late transition-metal series using the plane-wave density-functional code VASP.[216] The results suggest that a buckled bi-planar (BBP) structure is more stable than the icosahedral structure when the *d* shell is more than half-filled. A buckled bi-planar (BBP) structure consists of two planes: a hexagonal plane with a central atom and a square with two flanking atoms between the hexagonal layer and the square. In a hexagonal bilayer (HBL) structure, the square with two flanking atoms is replaced by an additional hexagonal plane. Depending on the total energy of the structures, the hexagon(s) and the square can be distorted with a varying degree of buckling of the planes. The BBP structure was found to be the most stable structure for 13-atom Ag and Cu clusters in their study, which were 0.84 eV and 0.53 eV lower than the corresponding icosahedral structure, respectively. While this observation is supported by the DFT studies of Longo and Gallego [172] and Wang and Johnson, [174] a number of Gaussian-orbital and plane-wave based DFT studies [175, 176, 179] reported different structures for Ag_{13} and Cu_{13} clusters. A similar observation applies to the Ni_{13} structure. Pseudoatomic-orbital based DFT studies [172, 177] suggest that the icosahedral structure is the most stable for Ni_{13}, but a number of researchers dispute this observation by proposing new structures based on plane-wave based DFT calculations.[175, 179–181]

In summary, while empirical and semi-empirical studies can predict some trends in cluster morphology with increasing cluster sizes, it is difficult to predict accurately the ground-state structure of many transition-metal clusters without taking into account quantum-mechanical effects explicitly in the calculations. On the other hand, the density-functional approach can address the problem fairly accurately, but a few theoretical issues concerning the use of an appropriate XC functional and the need for the inclusion of the semi-core states in the pseudopotential for specific systems (e.g., V and Cr) continue to exist (see, for example, Refs. [178] and [217]).

6.3 Computational Method

The starting point of our method is to generate a random configuration such that no two atoms are at a distance closer than twice the diameter of the constituent atoms. The total energy of an atomic configuration can be calculated by using an appropriate classical potential. In particular, we employ the Finnis-Sinclair (FS) potential [209, 210] for Fe clusters and the Sutton-Chen (SC) potential [211] for Ni and Cu clusters. The Finnis-Sinclair potential, for a system consisting of N atoms, is written as:

$$E = \frac{1}{2}\sum_{i}^{N}\sum_{j\neq i}^{N} V\left(r_{ij}\right) - \varepsilon\sum_{i}^{N}\sqrt{\rho_i}. \tag{6.1}$$

The repulsive two-body interaction $V(r_{ij})$ and the attractive on-site energy ρ_i are given by,

$$V(r_{ij}) = \begin{cases} (r_{ij}-c)^2(c_o + c_1 r_{ij} + c_2 r_{ij}^2) & \text{for } r_{ij} \leq c \\ 0 & \text{for } r_{ij} > c \end{cases} \tag{6.2}$$

and

$$\rho_i = \sum_{j\neq i}^{N} \phi\left(r_{ij}\right), \tag{6.3}$$

respectively, where

$$\phi(r_{ij}) = \begin{cases} \left(r_{ij}-a\right)^2 + \gamma\frac{\left(r_{ij}-a\right)^3}{a} & \text{for } r_{ij} \leq a \\ 0 & \text{for } r_{ij} > a. \end{cases} \tag{6.4}$$

The Sutton-Chen potential is given by,

$$E = \varepsilon\sum_{i}^{N}\left[\frac{1}{2}\sum_{j\neq i}^{N}\left(\frac{a}{r_{ij}}\right)^n - c_o\sqrt{\rho_i}\right], \tag{6.5}$$

where

$$\rho_i = \sum_{j\neq i}^{N}\left(\frac{a}{r_{ij}}\right)^m. \tag{6.6}$$

In our approach, the initial random configuration was equilibrated at a temperature T=3000 K for 10^5 Monte Carlo steps (MCS). Subsequently, the temperature of the system was decreased sequentially by a factor of 0.99 and, at each temperature, the system was equilibrated for 10^5 MCS until the final temperature of the system reduced to 1 K. The total-energy relaxation was achieved in two steps: a) computing the total force on each atom

Table 6.1: Finnis-Sinclair and Sutton-Chen potential parameters

	n	m	a (Å)	ε (eV)	γ	c (Å)	c_o	c_1	c_2
Fe	–	–	3.569745	1.828905	1.8	3.40	1.2371147	-0.3592185	-0.0385607
Ni	9	6	3.52	0.015707	–	–	39.432	–	–
Cu	9	6	3.61	0.012382	–	–	39.432	–	–

($\mathbf{f_i^n}$) in the initial state **n**; b) displacing a randomly selected atom at site i from an initial state **n** to a proposed state **m** by,[155, 218]

$$\Delta\mathbf{r_i^{mn}} = \alpha\,\delta\mathbf{r_i^{mn}} + \beta\,A\,\mathbf{f_i^n}. \tag{6.7}$$

The parameters α and A in Eq. (6.7) determine the length of a random displacement ($\alpha\,\delta\mathbf{r_i^{mn}}$) and the contribution from the potential gradient (-$\mathbf{f_i^n}$) in generating a proposed configuration **m**, respectively. One may treat β as an optimization parameter without any reference to temperature or β can be simply set to $\frac{1}{k_BT}$, where k_B is the Boltzmann constant. The displacement $\delta\mathbf{r_i^{mn}}$ is generally, but not necessarily, drawn from a Gaussian distribution with a zero mean and a variance $2A$. It can be shown that the prescription stated in Eq. (6.7) is related to Brownian-dynamics simulations in the presence of an external force for an appropriate choice of $\alpha\,\delta\mathbf{r_i^{mn}}$ and A, where the motion of a particle is governed by the sum of the external force(s) and a random force reflecting the complex interaction between the particle and a noisy environment. Following Rossky *et al.* ,[155] and Allen and Tildesley,[67] one can show that a proposed MC move in Eq. (6.7) is accepted with the probability $P_{mn} = \min[1, \exp(-\beta\,\Delta E_i^{mn})]$, where

$$\begin{aligned}\Delta E_i^{mn} = \delta E^{mn} \quad &+ \quad \left[\frac{1}{2}(\mathbf{f_i^n} + \mathbf{f_i^m})\cdot\Delta\mathbf{r_i^{mn}} + \frac{\beta A}{4}\Big\{(\delta\mathbf{f_i^{mn}})^2\right. \\ &+ \quad \left. 2\mathbf{f_i^n}\cdot\delta\mathbf{f_i^{mn}}\Big\}\right],\end{aligned} \tag{6.8}$$

and

$$\delta E^{mn} = E^m - E^n, \quad \delta\mathbf{f_i^{mn}} = \mathbf{f_i^m} - \mathbf{f_i^n}.$$

In Eq. (6.8), E^n and E^m are the total energy of the system in the initial state and the proposed state, respectively. Likewise, $\mathbf{f_i^n}$ and $\mathbf{f_i^m}$ are the total force on an atom at site i before and after the displacement, respectively. An MC move is accepted or rejected using the conventional Metropolis algorithm. In this work, we chose to move one atom at a time but it is possible to move a group of atoms simultaneously by ensuring that the change of total energy, ΔE^{mn}, associated with multi-atom moves, is properly evaluated. To improve the acceptance rate,

we adjusted the step length by assuming a linear temperature dependence of α with a lower cutoff value of 0.001 Å at 1 K and an upper cutoff value of 0.05 Å at 3000 K. The value of A was chosen in such a way that βA was approximately 4–5 $\times 10^{-3}$ and $\delta \mathbf{r_i^{mn}}$ was a random number (between -1 and +1) taken from a uniform distribution. Our choice of δr_i^{mn} from a uniform random distribution eliminates the coupling between the terms in the right-hand side of Eq. (6.7), as mentioned in the context of Brownian dynamics simulations. However, this has no direct bearing on the present FMC simulations as the primary goal of our work is to minimize the total energy of the clusters. In this preliminary study, we made no attempts to optimize the values of α and A apart from what we have stated above. These parameters can be further adjusted during simulations to improve the efficiency of the method.

To examine the stability of the structure at the putative global minimum of a classical potential, namely the Finnis-Sinclair or the Sutton-Chen potential in the present study, we have carried out *ab initio* total-energy optimizations of the CCD clusters and those obtained from our FMC simulations. *Ab initio* calculations proceed within the framework of density-functional theory [71] using a plane-wave basis, as implemented in the DFT code NWChem.[161] For this purpose, a cluster was placed in a large cubic supercell such that the neighboring images of the cluster do not interact each other in order to prevent the system being treated as a bulk solid during *ab initio* relaxations. A cubic supercell of length 20 Å was found to be sufficient for the present calculations. The exchange-correlation energy was treated using the generalized gradient approximation (GGA) in the Perdew-Burke-Ernzerhof (PBE) formulation,[79] and the norm-conserving pseudopotentials, modified into a separable form due to Kleinman and Bylander,[219] were employed in this work. The Kohn-Sham eigenstates were expanded in a plane-wave basis with a kinetic-energy cutoff of 37 Hartrees (1006.8 eV). To verify the sufficiency of the energy cutoff, a few clusters were tested using a high-energy cutoff of 45 Hartrees (1224.5 eV), which yielded no significant changes in the geometry and the total-energy values of the clusters in comparison to the results obtained by using a cutoff value of 37 Hartrees. Throughout the work, the total-energy optimization of the clusters was carried out using the spin-polarized PBE-GGA functional until the total force on each atom of the clusters was found to be less than 0.01 eV/Å. In addition, Car-Parrinello molecular-dynamics (CPMD) [220] simulations and subsequent geometry relaxations were used to check the thermal stability of the 13-atom Cu/Ni/Fe clusters.

6.4 Results and Discussions

6.4.1 Global minima from the classical FMC simulations

We begin by addressing the total energy of the putative global minima of the clusters from the classical FMC simulations and then proceed to compare the results with the corresponding data from the Cambridge Cluster Database (CCD). For a list of putative global minima and the corresponding structure of a number of clusters, visit the Cambridge Cluster Database at http://www-wales.ch.cam.ac.uk/CCD.html. In Table 6.2, we have listed the total energy of 13-, 30-, and 55-atom clusters of Fe, Ni, and Cu from the classical FMC simulations along with the corresponding CCD values. A direct comparison of the total-energy values, from columns 2 and 3 in Table 6.2, suggests that the FMC values practically coincide with the CCD values except for Fe_{30}, where a deviation as small as 4.4 meV has been observed. This deviation is significantly smaller than the energy associated with the thermal fluctuations at 300 K. Notwithstanding the observation that the CCD energy values are consistently lower than the corresponding FMC values by about 0–5 meV, the FMC results are quite impressive considering the fact that no gradient optimization has been performed on the FMC structures. This reflects the simplicity and efficiency of the FMC method. The latter is apparent from Figs. 6.1(a) and 6.1(b), where the evolution of the total energy with the CPU time and the number of the MC steps are plotted, respectively. It is apparent from Fig. 6.1(a) that the total-energy decay in the FMC simulation is sufficiently faster than its MC counterpart despite the fact that computationally expensive local gradients or atomic forces have been evaluated during the FMC simulation. A similar observation follows from the evolution of the total energy with the MC steps in Fig. 6.1(b).

To examine the stability of the clusters at the putative global minimum of the FS and SC potentials, we have listed in Table 6.3 the total-energy values obtained from the first-principles relaxations of the classical FMC and CCD configurations using the density-functional code NWChem by perturbing the atomic positions by up to 15% of the average nearest-neighbor distance between the atoms. Table 6.3 suggests that the total-energy differences are quite small, with a deviation less than one tenth of an electron-volt, except for 55-atom clusters. A deviation of 0.1-0.16 eV has been observed for 55-atom clusters, which is partly due to the difficulty in optimizing large clusters using the computationally expensive CPMD method and in part to the spin-polarized nature of the calculations. It may be noted that the total-energy values of the 30-atom NWChem-relax FMC clusters for all but Cu_{13} are consistently lower than the corresponding CCD values, and vice versa for the clusters with 55 atoms. In view of this observed energy difference, it would be instructive to examine to what extent this small energy variation can affect the three-dimensional structure

Table 6.2: Total energy of Cu, Ni, and Fe clusters from the classical FMC simulation along with the corresponding value of the CCD clusters. Note that the values in column 4 are given in meV.

System	FMC (eV)	CCD (eV)	E_{fmc}-E_{ccd} (meV)
Fe_{13}	-40.2983	-40.2985	0.2
Fe_{30}	-101.4469	-101.4513	4.4
Fe_{55}	-194.6847	-194.6868	2.1
Ni_{13}	-44.1142	-44.1143	0.1
Ni_{30}	-108.4284	-108.4296	1.2
Ni_{55}	-207.6107	-207.6135	2.8
Cu_{13}	-34.7757	-34.7758	0.1
Cu_{30}	-85.4753	-85.4762	0.9
Cu_{55}	-163.6617	-163.6640	2.3

Table 6.3: Total energy of Fe, Ni, and Cu clusters from *ab initio* relaxation of the FMC and CCD structures. Note that the values of E_{fmc} - E_{ccd} in column 4 are given in electron-volt.

System	FMC (Hartree)	CCD (Hartree)[a]	E_{fmc}-E_{ccd} (eV)
Fe_{13}	-1575.6009	-1575.6018	0.0245
Fe_{30}	-3636.0472	-3636.0366	-0.288
Fe_{55}	-6666.4826	-6666.4886	0.163
Ni_{13}	-556.1933	-556.1940	0.019
Ni_{30}	-1283.9900	-1283.9883	-0.0463
Ni_{55}	-2354.5115	-2354.5154	0.106
Cu_{13}	-707.5190	-707.5205	0.041
Cu_{30}	-1633.1592	-1633.1603	0.032
Cu_{55}	-2994.5459	-2994.5497	0.103

of the clusters. We address this question in sections 6.4.4 and 6.4.5 with an emphasis on the two-, three- and higher-order correlation functions, and compare the real-space distribution of the atoms obtained from the NWChem-relax FMC and CCD clusters.

6.4.2 Part I: Structure of 13-atom Cu/Ni/Fe clusters from *ab initio* studies

Our discussion in section 6.2 suggests that the electronic effects arising from the *d*-electrons can play a significant role in the determination of the ground-state structure of a number of 13-atom TM clusters, such as Cu and Fe. The great majority of the simulation studies on TM clusters using classical potentials suggest that the icosahedral structure is the preferred

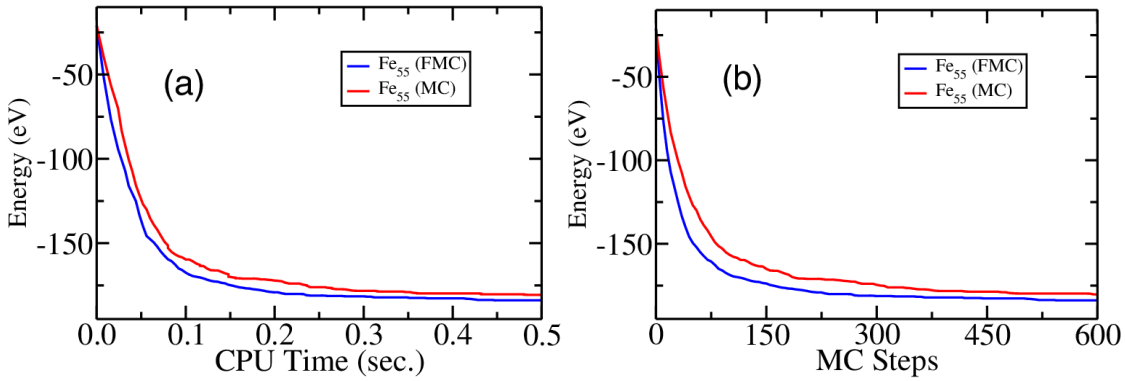

Figure 6.1: The evolution of the total energy of an Fe_{55} cluster in the classical FMC and MC simulations. a) Total energy versus CPU time, b) Total energy versus MCS steps.

minimum for the 13-atom clusters of Cu and Fe, but quite a few *ab initio* studies indicate that these systems adopt a bi-planar or platelet-like form, instead of a more symmetrical icosahedral structure. Even within the density-functional framework, the results vary considerably from one study to another. For example, the plane-wave-based DFT calculations, usingVASP, by Chang and Chou [170] suggest that a BBP structure of Ag_{13} and Cu_{13} is more stable than the corresponding icosahedral structure. However, the results from the Gaussian-orbital-based DFT calculations by Pereiro et al.[175] indicate that the icosahedral structure is the most stable structure of Ag_{13}. The results above contrast with those based on the plane-wave DFT studies, using VASP, by Hue *et al.* [176] and Piotrowski *et al.* ,[179] which reported new ground-state structures of Ag_{13}. Furthermore, recent *ab initio* studies on TM clusters by Jena *et al.* ,[221, 222] using VASP[216] and GAUSSIAN,[223] have indicated that the ground-state energy of 13-atom Cu/Ni/Fe clusters correspond to well-defined spin multiplicities, which need to be taken into account for accurate total-energy calculations of 13-atom Cu/Ni/Fe clusters. Thus, the structures of some of the 13-atom TM clusters are still very controversial and there is a need for accurate *ab initio* calculations for structural determination of small TM clusters. Since an in-depth study of 13-atom TM clusters is outside the scope of the present work, we specifically address here the credibility of the structures of a few 13-atom TM clusters, which are obtained from the classical FMC simulations followed by CPMD[220] and first-principles total-energy relaxation using the density-functional code NWChem. Here, we have used the values of spin multiplicities reported in Ref. [221].

In Table 6.4, we have listed the total-energy values of 13-atom Cu, Ni, and Fe clusters obtained from the joint FMC-NWChem simulations. Starting with the 13-atom icosahedral structure obtained from the classical FMC simulations, the total energy of each cluster was minimized using the density-functional code NWChem. Thereafter, finite-temperature

Table 6.4: *Ab initio* total-energy values of 13-atom transition-metal clusters from a joint FMC-NWChem simulation. For Cu_{13}, the energy difference $\Delta E = E - E_{\min}$ is expressed with respect to the lowest-energy configuration.

Cluster	Initial symmetry	Final symmetry	E (Hartree)	Δ E (eV)
Ni	ICO	ICO	-556.1921	
Fe	ICO	ICO	-1575.6020	
	BBP	bi-layer1	-707.5611	0.31
Cu	ICO	bi-layer2	-707.5723	0.0
	HBL	bi-layer3	-707.5653	0.19

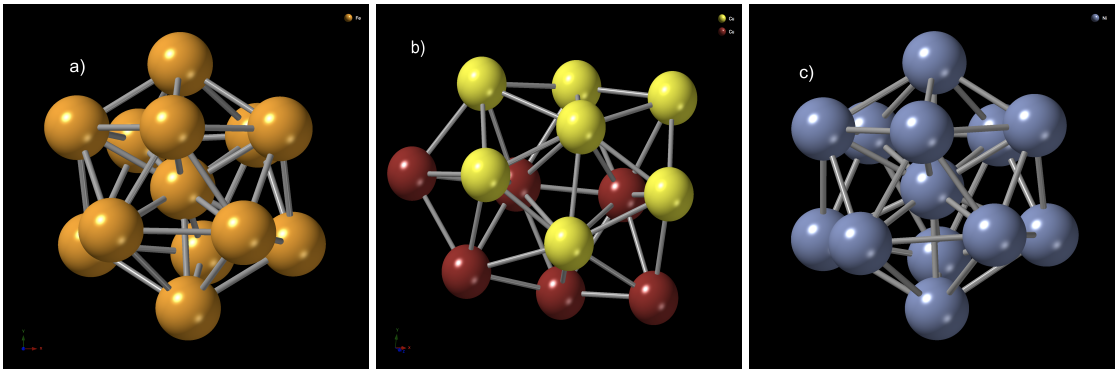

Figure 6.2: The putative ground-state structures of 13-atom transition-metal clusters from a joint FMC-NWChem simulation: a) Fe_{13} (icosahedron); b) Cu_{13} (bilayer2) with a buckled hexagonal layer (yellow); and c) Ni_{13} (icosahedron). See Table 6.4 for the ground-state energy of the structures and the possible low-energy isomers of Cu_{13}.

CPMD simulations were carried out at T = 300 K for 6–10 ps, with a time step of 0.12 fs, to explore the neighboring regions of the potential-energy surface, followed by total-energy relaxation to determine the equilibrium structure of the clusters. An examination of the final structures reveals that Ni_{13} and Fe_{13} continue to remain in the icosahedral structure, whereas Cu_{13} transforms from the icosahedral structure to a buckled bi-planar (BBP) structure during 10 ps of thermalization (at 300 K) and eventually adopts a low-energy bilayer structure upon post-CPMD total-energy relaxation. To further examine the stability of the bilayer structure of Cu_{13}, additional CPMD runs were conducted for 10 ps starting with a BBP structure and a hexagonal bilayer (HBL) structure. In both the cases, the simulations produced bilayer structures, which were energetically very close to each other but slightly different in structure. Table 6.4 lists the total energy of the clusters, the initial and final symmetries, and the energy difference (ΔE) between the bilayer structures of Cu_{13}. Figure 6.2 shows the minimum-energy structures of the 13-atom Cu, Ni, and Fe clusters, obtained from the

joint FMC-NWChem runs, of duration 6–10 ps, followed by total-energy relaxations. The presence of a buckled hexagonal layer with a central atom, shown in yellow color, is clearly visible in Fig. 6.2(b). The remaining atoms form a highly distorted layer to produce an approximate bilayer or platelet-like structure. On the other hand, the 13-atom Ni and Fe clusters are found to be stable in the icosahedral structure, as shown in Figs. 6.2(a) and 6.2(c), respectively. The transition of the Cu_{13} cluster from a 13-atom icosahedral structure to a BBP structure and then to a bilayer structure indicates that, for an exhaustive molecular-dynamical search for new structures on the PES, one must conduct rather long simulations lasting several tens of picoseconds at different temperatures.

6.4.3 Part II: Structure of 13-atom Cu/Ag clusters from *ab initio* studies

As discussed earlier, an ensemble of low-energy structural configurations, collected during the course of *ab initio* molecular-dynamics simulations and followed by subsequent relaxation, constitutes a set of candidate structures for determining the putative ground-state configuration of 13-atom Ag and Cu clusters. Further relaxation of these structures, using the plane-wave density-functional code VASP, provides the final structure for Ag_{13} and Cu_{13} clusters. The potential energy of the putative global minimum for Ag and Cu clusters is listed in Table 6.5, with respect to the potential energy of the corresponding icosahedral structure. The bilayer nature of these structures is evident from Fig. 6.3, where we have shown a three-dimensional ball-and-stick model of the structures. The results are consistent with the recent study by Chaves *et al.* [224], where similar bilayer structures of 13-atom Cu and Ag clusters were reported using DFT calculations. Other local minima structures for 13-atom Cu/Ag clusters are shown in Fig. 6.4 and Fig. 6.5, respectively.

Table 6.5: Total-energy differences (in eV) for 13-atom Cu and Ag clusters from their icosahedral counterpart, using SIESTA and VASP.

Symmetry	Cu_{13} : ΔE (eV)		Ag_{13} : ΔE (eV)	
	SIESTA	VASP	SIESTA	VASP
ICO	0.0	0.0	0.0	0.0
BBP	-0.460	-0.462	-0.514	-0.785
Bilayer	-0.926	-0.972	-0.934	-1.231
Bilayer*	-1.014		-1.300	

* Energy difference of lowest energy configuration observed by Chaves *et al.* [224].

We have computed the the average bond length ($\bar{d}_i$) and the effective coordination

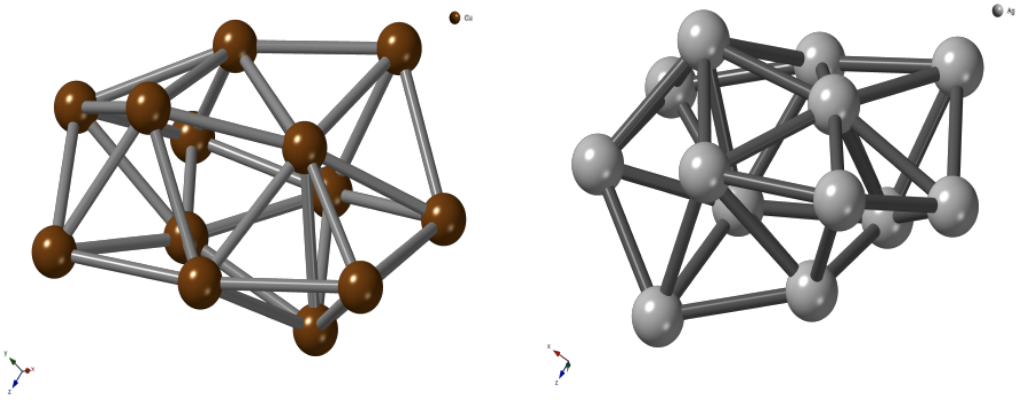

Figure 6.3: The structure of putative global minimum of a) 13-atom Cu cluster and b) 13-atom Ag cluster.

Table 6.6: Average bond length (d_{av}) and effective coordination number (C_{av}) for Cu and Ag clusters

System	Cu_{13}		Ag_{13}	
Symmetry	d_{av} (Å) SIESTA(VASP)	C_{av} SIESTA(VASP)	d_{av} (Å) SIESTA(VASP)	C_{av} SIESTA(VASP)
ICO	2.612 (2.500)	6.395 (6.396)	3.037 (2.894)	6.396 (6.396)
BBP	2.563 (2.454)	5.469 (5.463)	2.982 (2.838)	5.468 (5.460)
Bilayer	2.570 (2.460)	5.702 (5.701)	2.994 (2.845)	5.709 (5.647)
Bilayer[§]	2.459	5.699	2.835	5.654

[§] Corresponding values observed by Chaves *et al.* [224].

number (C_i) of an atom at site i. The average bond length of an atom at site i is given by,

$$\bar{d}_i = \sum_j d_{ij}\, p_{ij}, \quad p_{ij} = \frac{e^{f(d_{ij})}}{\sum_j e^{f(d_{ij})}}, \quad f(d_{ij}) = \left[1 - \left(\frac{d_{ij}}{\bar{d}_i}\right)^6\right], \tag{6.9}$$

where d_{ij} is the radial distance between two atoms at sites i and j. The site-average bond length (d_{av}) and the effective coordination number (C_{av}) are given by,

$$d_{av} = \frac{1}{N}\sum_{i=1}^{N} \bar{d}_i, \quad C_{av} = \frac{1}{N}\sum_{i=1}^{N} C_i, \quad C_i = \sum_{j=1}^{N} e^{f(d_{ij})} \tag{6.10}$$

Equations (6.9) and (6.10) permit us to calculate an effective coordination number and average bond length of a cluster without introducing any arbitrary cutoff distance in a self-consistent manner [180, 224, 225]. Starting with an approximate value of $\bar{d}_i$, one can use

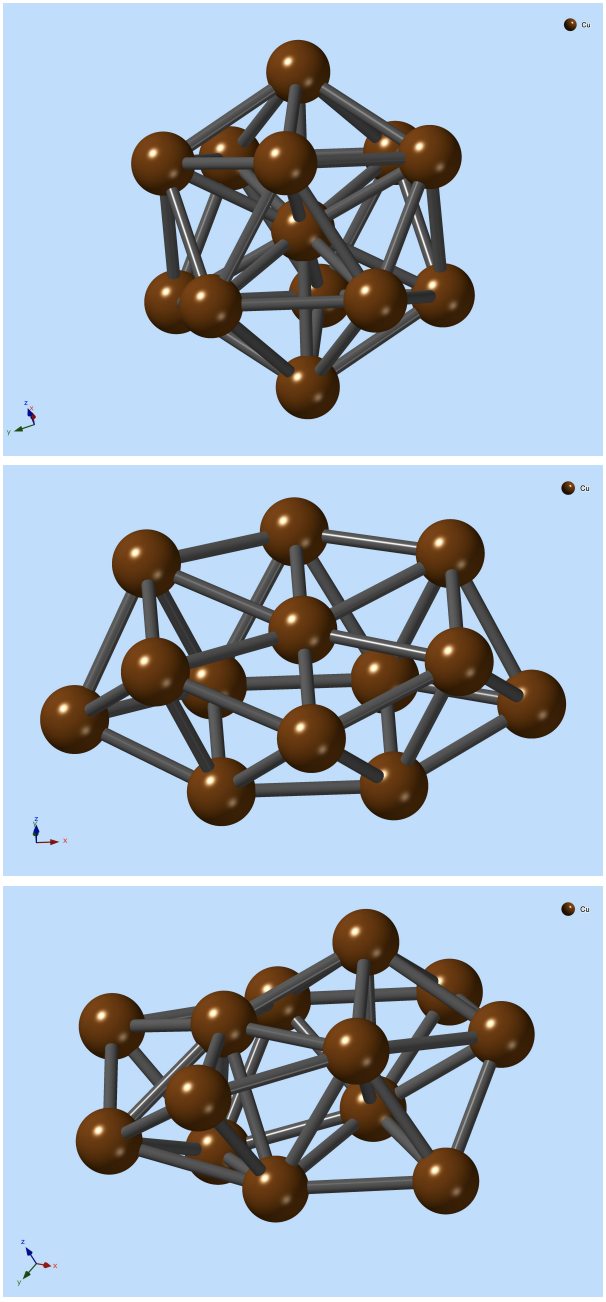

Figure 6.4: The structure of local minimum of 13-atom icosahedral, BBP and bilayer Cu cluster.

Eq. (6.9) to improve the estimate of $\bar{d}_i$ iteratively. Table 6.6 lists the average bond lengths and the effective coordination numbers for icosahedral, BBP and bilayer structures of 13-atoms Cu and Ag clusters obtained from SIESTA and VASP. The corresponding values computed by Chaves *et al.* [224] are also listed for a comparison. An examination of the results from Table 6.6 suggests that the total-energy values obtained from the pseudoatomic-orbital-based

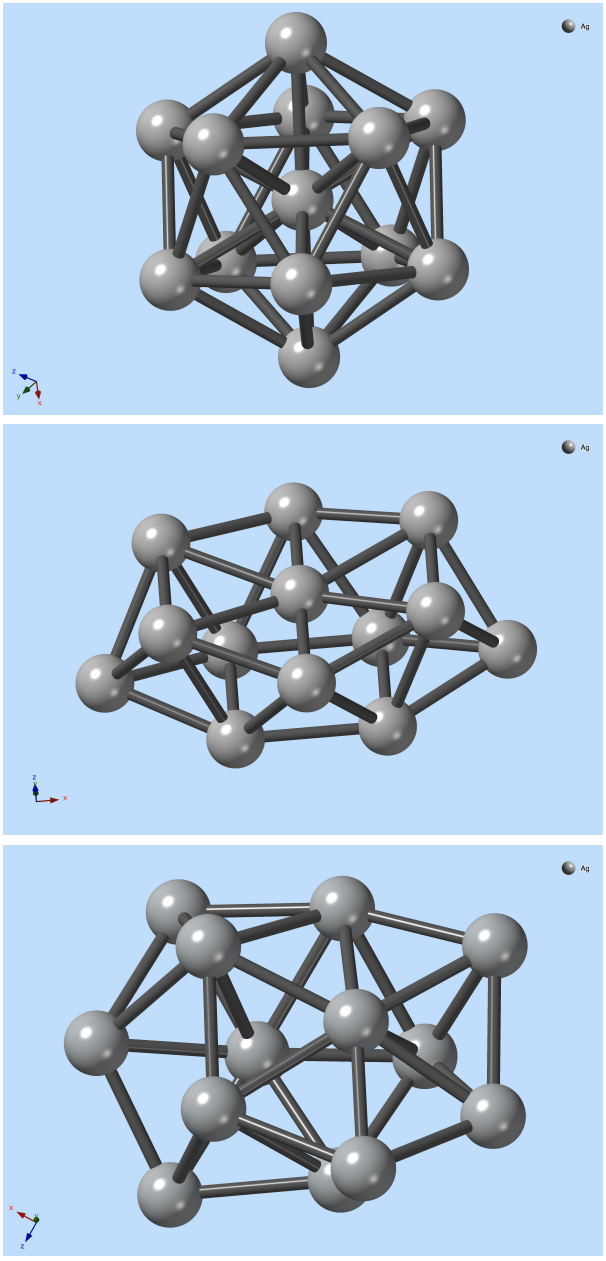

Figure 6.5: The structure of local minimum of 13-atom icosahedral, BBP and bilayer Ag cluster.

DFT code SIESTA slightly but consistently overestimates the value of total-energy than those obtained from the plane-wave-based VASP calculations. This is also reflected in the average bond-length of Ag and Cu atoms. The bond lengths obtained from VASP relaxations are approximately 4% shorter than the ones calculated from using SIESTA.

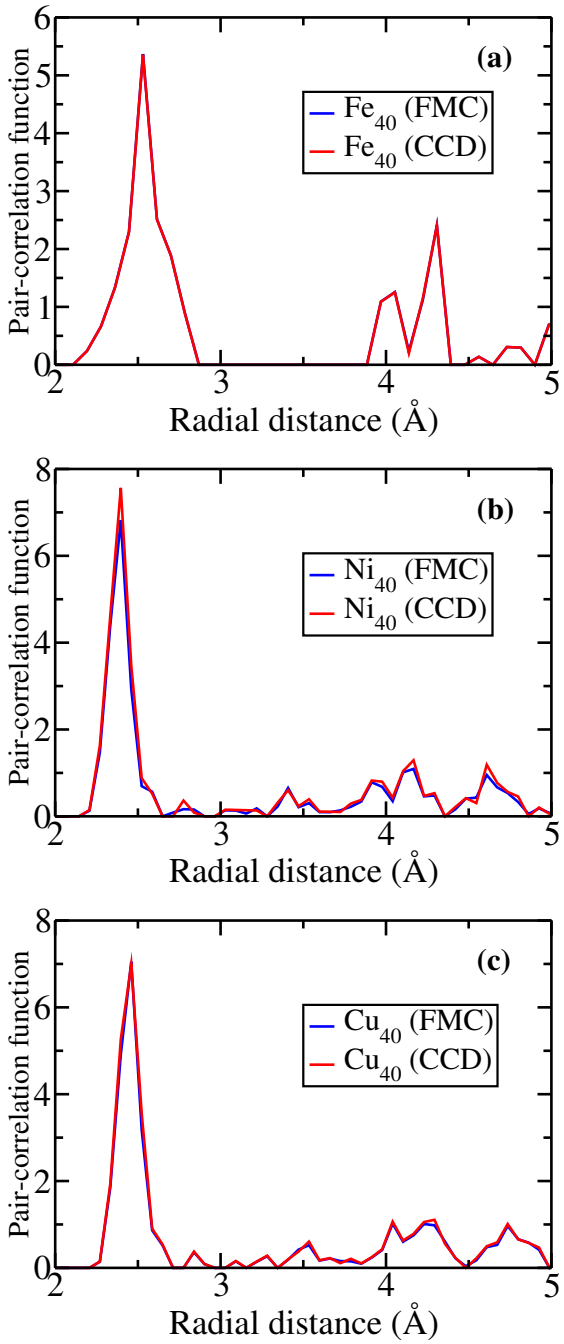

Figure 6.6: The pair-correlation functions for a) Fe, b) Ni, and c) Cu clusters from the FMC simulations. The corresponding pair-correlation functions for the CCD clusters are also shown for comparison.

6.4.4 Local atomic structure and bonding environment

Since the ground-state configuration a cluster must be independent of the optimization method for a given potential, it is appropriate to examine whether a small difference in

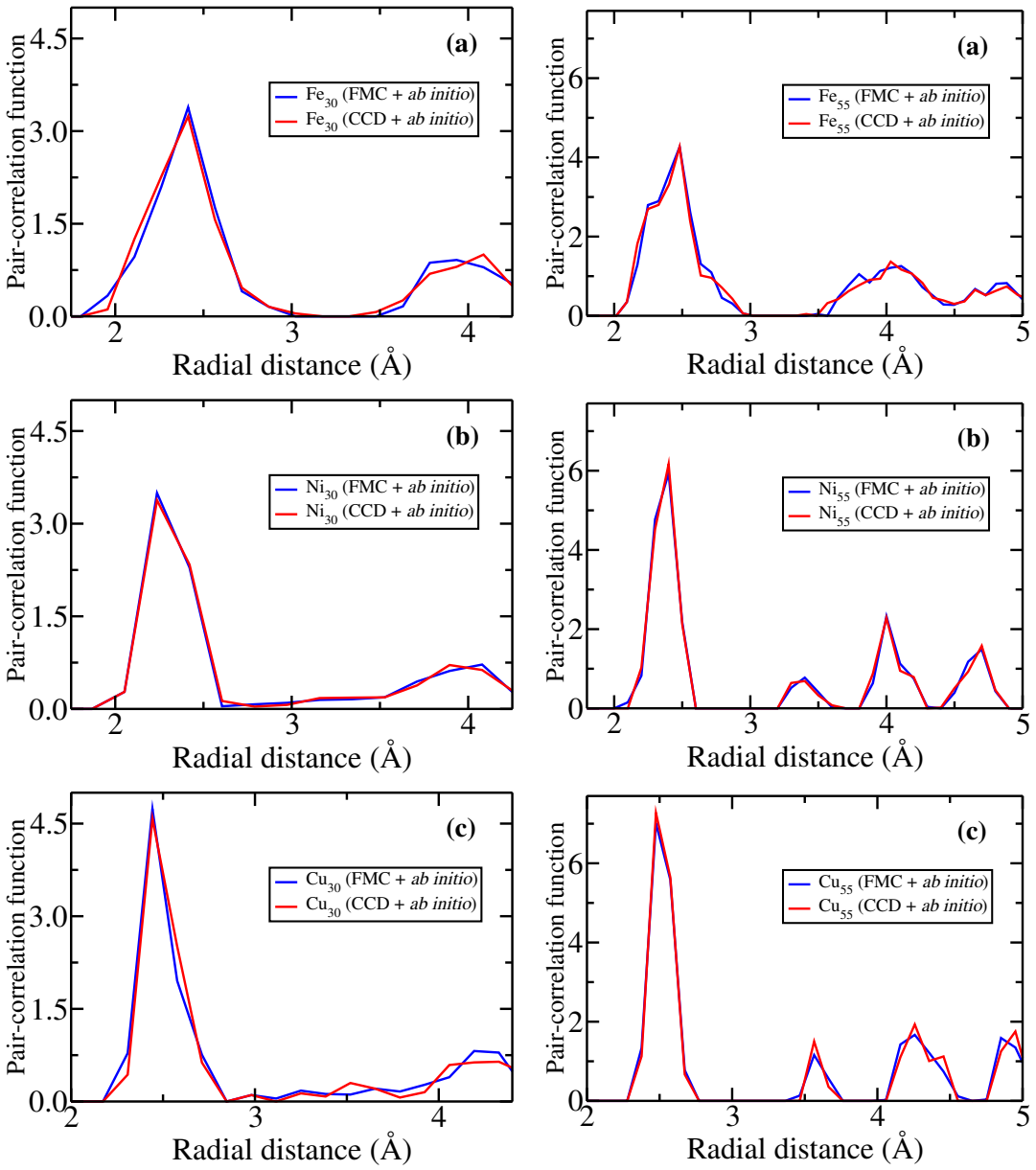

Figure 6.7: The pair-correlation functions of: a) Fe_{30}; b) Ni_{30}; and c) Cu_{30} clusters obtained from *ab initio* relaxations of FMC (blue) and CCD (red) structures using the density-functional code NWChem.

the total energy between a pair of clusters, mentioned in section 6.4.1, can have nontrivial effects on the three-dimensional distribution of the atoms. This is particularly relevant for large clusters due to the presence of a multitude of low-lying minima on the potential-energy surface. For large clusters, it is possible for the system to adopt a number of different structural configurations, which are either energetically degenerate or very close to each other (also known as an isomer). Thus, it is necessary to examine the structural similarities

and differences between the NWChem-relax FMC and CCD clusters by systematically addressing the atomic-correlation functions of increasing order. Since the number density of a cluster can vary with its size, we have assumed a suitable bounding box for the computation of the pair-correlation function of a cluster of given size. In computing the pair-correlation function of a cluster, using the conventional definition of the radial correlation between atoms, we have used a suitable bounding box to calculate the number density of the atoms. Since the number density is identical for both the FMC and CCD clusters, our results are not affected by any small variation or arbitrariness in the size of the bounding box. Figure 6.7 presents the pair-correlation functions (PCF) for a 30-atom cluster of Fe, Ni, and Cu, obtained from the NWChem-relax FMC and CCD configurations. It is apparent from Fig. 6.7 that, apart from a minute difference in the vicinity of 4 Å for Fe and Cu clusters, the PCFs of the FMC and CCD clusters effectively coincide with each other, reflecting the structural similarities as far as the radial correlation of the atoms is concerned. Similar conclusions can be reached from Fig. 6.8 and Fig. 6.9, where the distribution of the bond angles between the nearest-neighbor atoms are presented.

Further characterization of the clusters is possible by analyzing the distribution of the first-shell coordination numbers of the atoms. To this end, we define the nearest-neighbor distance between the atoms from the first minimum of the pair-correlation functions, as shown in Fig. 6.7. For Fe_{30}, Ni_{30}, and Cu_{30} clusters, these values correspond to 3.2 Å, 2.65 Å, and 2.9 Å, respectively. The values are consistent with the sum of the atomic radius of the constituent atoms in the clusters. Figure 6.10 shows the histograms of the first-shell atomic-coordination numbers of Fe_{30}, Ni_{30}, and Cu_{30} clusters, obtained from the NWChem-relax FMC and CCD configurations.

6.4.5 Bond-orientational order parameter

In the preceding section, we have shown that the radial and bond-angle distributions, as well as the atomic-coordination numbers of the NWChem-relax FMC and CCD clusters match closely with each other. However, this does not necessarily establish that the FMC and CCD clusters are identical with each other as far as the three-dimensional distribution of the atoms are concerned. For example, for a given set of atoms, it is possible to construct different local-bonding environments that can have identical radial, bond-angle and atomic-coordination number distributions. Thus, to obtain information on the orientation of a set of bonds (with respect to a fixed coordinate system in space) formed by a group of atoms, an appropriate bond-orientational order parameter (BOP) needs to be defined. To this end, we compute the BOP, introduced by Steinhardt *et al.* [119] in an effort to further establish

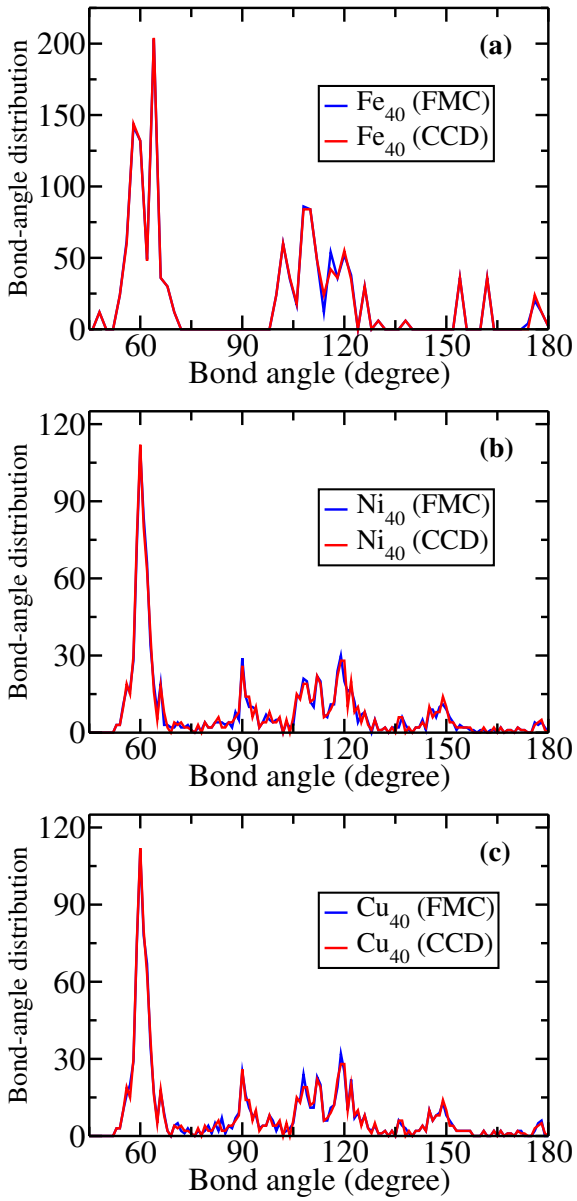

Figure 6.8: Bond-angle distributions for a) Fe, b) Ni, and c) Cu clusters from the FMC and CCD structures.

that the FMC and CCD clusters are nearly identical to each other. Since the BOP depends on the number of the nearest neighbors and the relative orientations of the neighbors with respect to the central atom, it incorporates some aspects of structural information from higher-order correlation functions of the clusters. The Steinhardt BOP often provides a simple and effective measure for determining the presence of micro- or para-crystalline structural units in solids. The local BOP, Q_l^i, reflects the bonding environment of an atom at site i, which is associated with the orientation of a set of bonds that originate from site i and

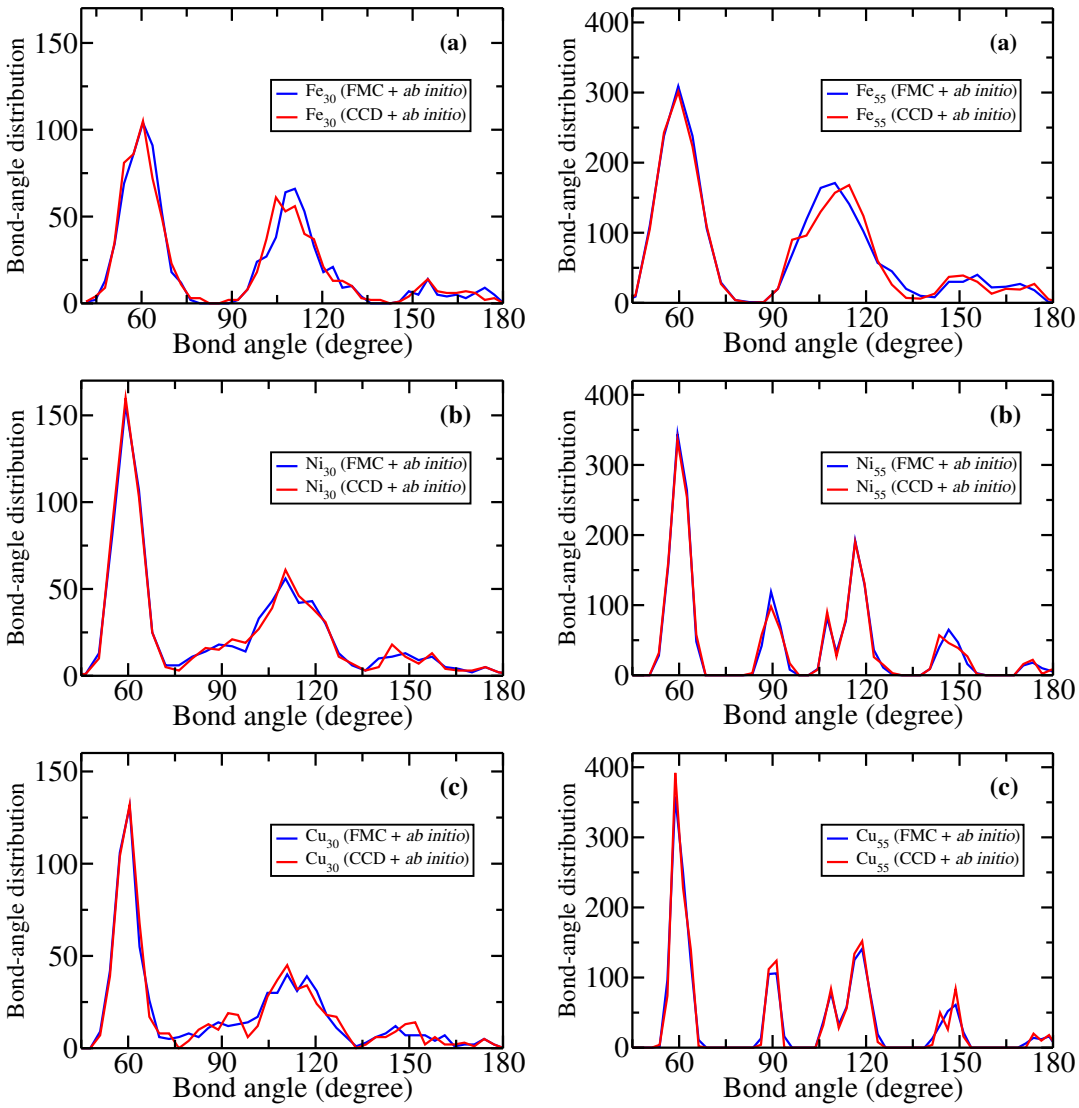

Figure 6.9: The distribution of the nearest-neighbor bond angles for: a) Fe_{30}; b) Ni_{30}; and c) Cu_{30} clusters. The results for the FMC and CCD structures, after relaxation using NWChem, are shown in blue and red colors, respectively.

terminate at its nearest neighbors. While Q_l^i is independent of the bond lengths, it depends on the number of the nearest neighbors of site i and their orientations with respect to a three-dimensional coordinate system with site i at its origin. In a spherical polar coordinate system, the local BOP Q_l^i is given by,

$$Q_l^i = \sqrt{\frac{4\pi}{2l+1}\sum_{m=-l}^{l}\left|\frac{1}{n_i}\sum_{j\in[n_i]}Y_l^m(\theta(\mathbf{r_{ij}}),\phi(\mathbf{r_{ij}}))\right|^2},$$

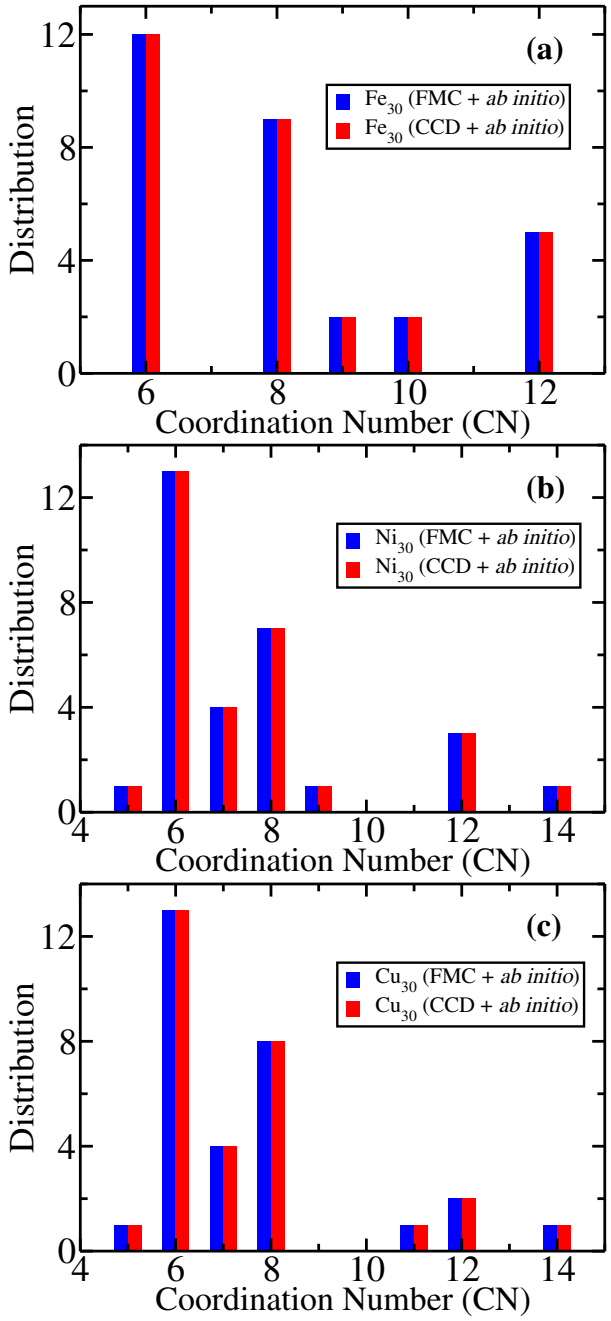

Figure 6.10: Histograms showing the coordination numbers of the first-shell atoms in: a) Fe_{30}; b) Ni_{30}; and c) Cu_{30} clusters. The FMC-NWChem and CCD-NWChem configurations are indicated in the plots.

and the global BOP, Q_l, follows from the sum of the individual value of Q_l^i at site i.

$$Q_l = \frac{1}{N}\sum_{i=1}^{N} Q_l^i.$$

Here n_i is the number of the nearest neighbors of atom i, N is the total number of atoms in the system, and θ and ϕ are the polar and azimuthal angles of the bond $\mathbf{r}_{ij}$, respectively. The symbol $[n_i]$ indicates the atomic indices of n_i nearest neighbors of atom i, and Q_l is the site-average value of Q_l^i over all atomic sites. Different values of l generally correspond to different crystalline structures; for example, Q_4 and Q_6 are often used in the literature to distinguish a cubic structure from a hexagonal one. Figure 6.11 shows the bond-orientational order parameter for two sets of Fe_{30}, Ni_{30}, and Cu_{30} clusters, obtained from *ab initio* relaxations of the FMC and CCD structures using NWChem. The results, for each set of the FMC and CCD clusters, are essentially identical except for a minor deviation for Fe_{30} owing to subtle differences in the bond-angle distribution of the FMC and CCD clusters near 110°, as observed in Fig. 6.9(a).

6.4.6 Geometry of transition-metal clusters

Having established that the two- and three-body correlation functions, as well as the local structure and the bonding environment of the atoms, of the FMC and CCD clusters practically match with each other, it seems intuitively valid to state that the clusters are essentially identical. However, a rigorous justification of this statement, based on the results so far discussed, turns out to be particularly delicate–owing to the hierarchy of the high-order correlation functions–and a more direct approach is needed to establish the identical nature of the FMC and CCD clusters. In an effort to achieve this, we therefore proceed to compare the structures atom-by-atom in this section. Toward that end, our approach is based on the following assertion: given two (nearly) identical configurations, it is possible to construct a series of transformations, involving translations and rotations in three dimensions, such that one configuration can be (approximately) mapped onto the other. We implement this ansatz by: a) translating the center of mass (CM) of each configuration to (0, 0, 0); b) subsequently, finding a unique direction vector for each configuration (e.g., the direction vector from the CM to the nearest atom); c) aligning these direction vectors with the z axis (0, 0, 1) using the axis-angle representation of vector rotation in three-dimensional space. Given two units vectors $\mathbf{P}$ and $\mathbf{Q}$ in three-dimensional space, $\mathbf{P}$ can be aligned with $\mathbf{Q}$ by constructing a rotation axis along $\mathbf{P} \times \mathbf{Q}$ and rotating $\mathbf{P}$ by an angle $\theta = \cos^{-1}(\mathbf{P} \cdot \mathbf{Q})$. This axis-angle representation of vector rotation in three dimensions can be translated into appropriate Euler rotation matrices. For small systems, it is often convenient to employ directly the Rodrigues' formula for rotation of a vector around a given axis in three dimensions. We emphasize that, in order for this ansatz to work satisfactorily, the configurations must be nearly identical to each other. Since the results in the preceding sections demonstrate unambiguously that this

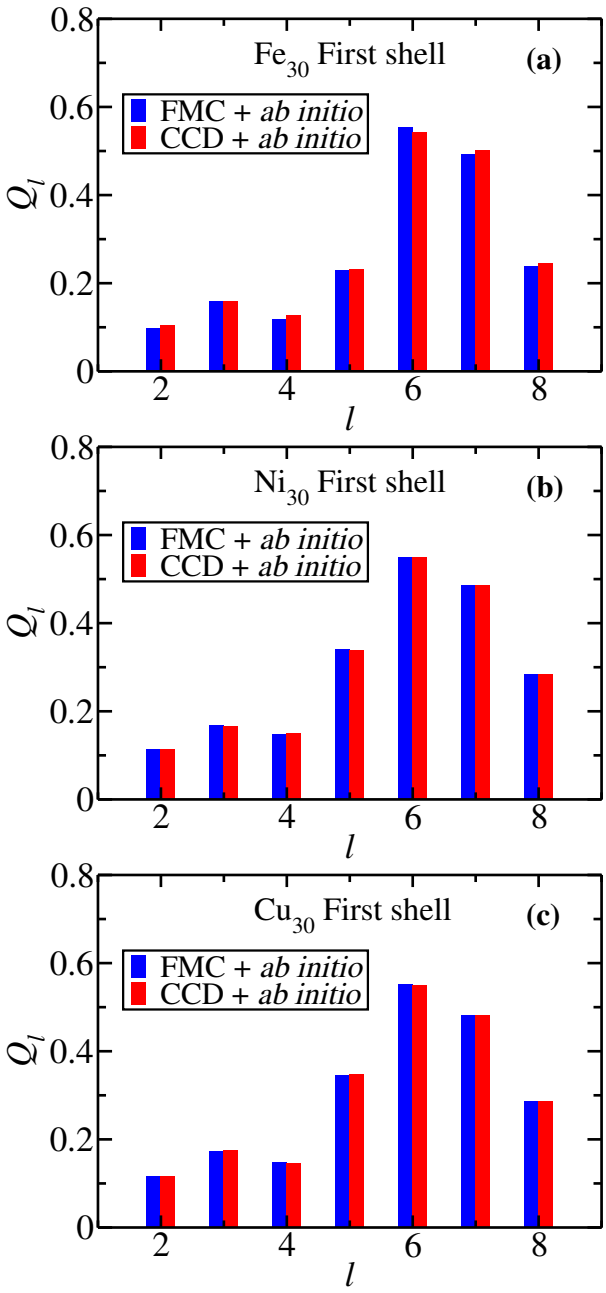

Figure 6.11: Bond-orientational order parameters (Q_l) for: a) Fe_{30}; b) Ni_{30}; and c) Cu_{30} clusters for several values of l. The results for the FMC-NWChem and CCD-NWChem structures are shown in blue and red colors, respectively.

condition is amply satisfied by the FMC and CCD clusters, we may expect that an appropriate transformation exists and that it can be employed for the purpose of superposition. Figures 6.12 and 6.13 show the geometry of 30-atom and 55-atom clusters, respectively, obtained from the joint FMC-NWChem relaxation. For the purpose of direct comparison with the CCD clusters, each of the FMC clusters was subjected to a translation and appropriate

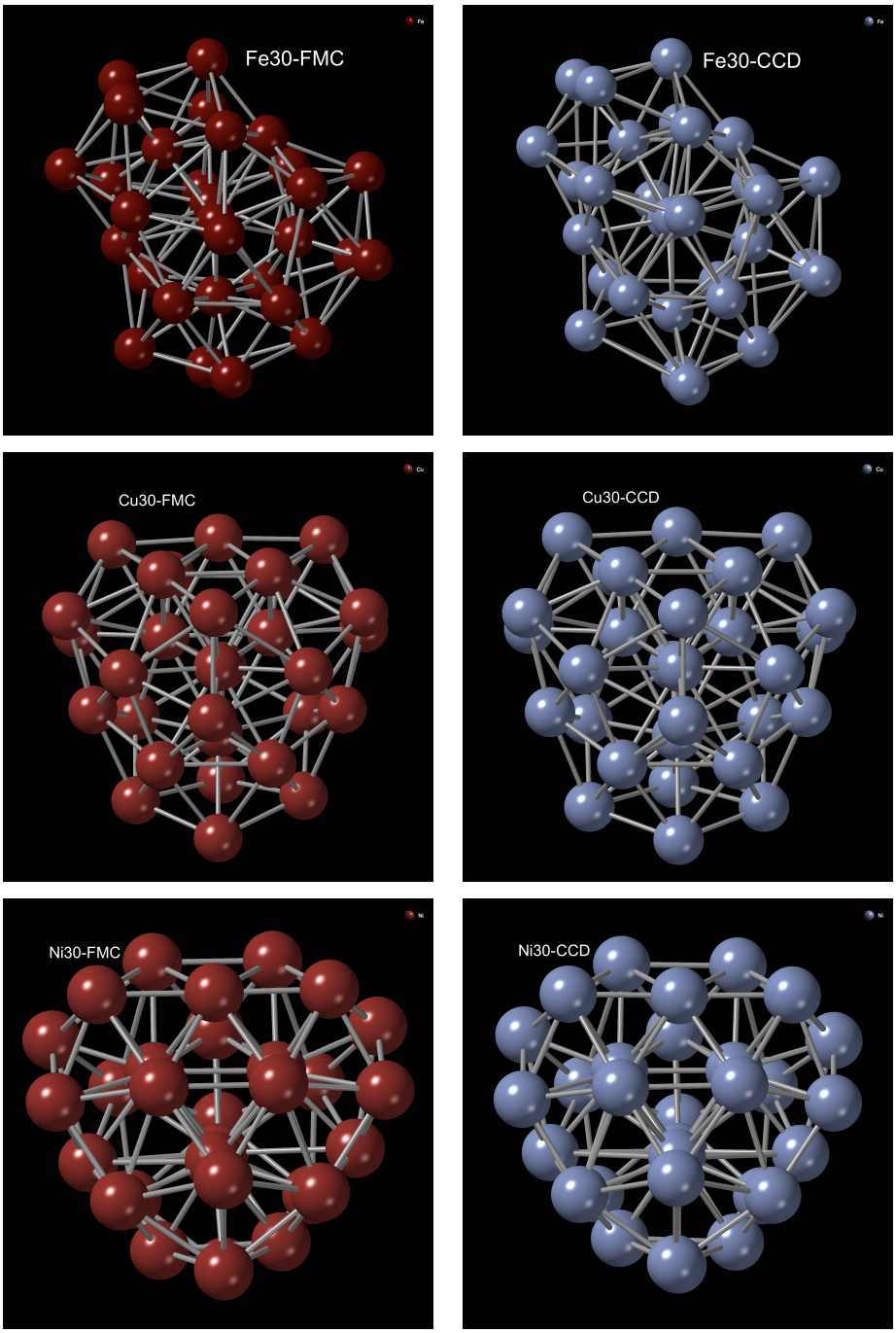

Figure 6.12: Geometry of Fe_{30}, Ni_{30}, and Cu_{30} clusters obtained from *ab initio* NWChem relaxations of the FMC (left panel) and CCD (right panel) clusters. For comparison, each configuration was subjected to a translation and appropriate rotations, as described in the text.

rotations. The resulting structures in Figs. 6.12 and 6.13 conclusively demonstrate that the FMC clusters are quite identical to their CCD counterparts. Finally, the electronic density of

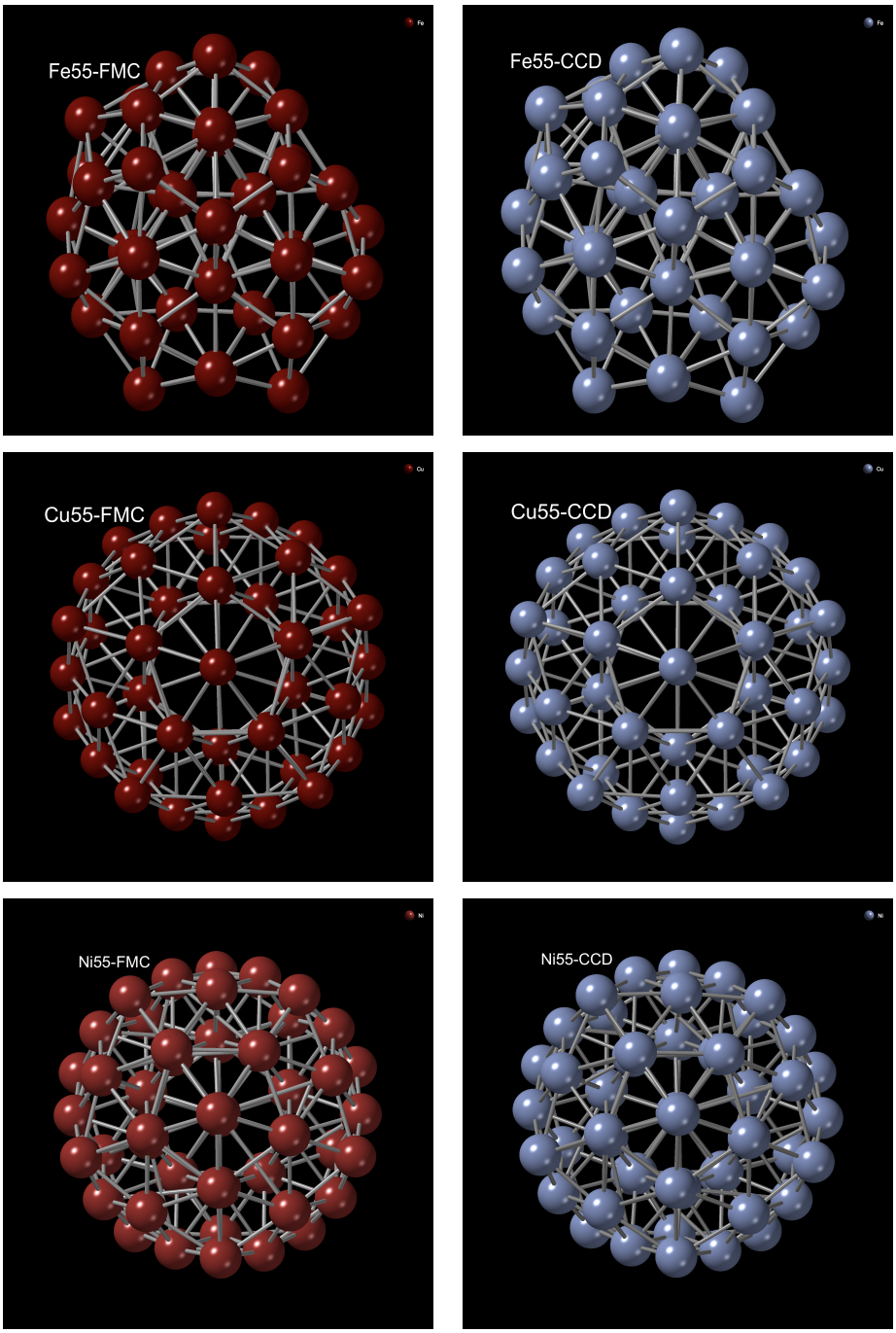

Figure 6.13: The structure of 55-atom Fe, Ni, and Cu clusters obtained from the *ab initio* NWChem relaxation starting from the FMC and CCD configurations. The FMC (left panel) and CCD (right panel) clusters are shown in dark red and light blue colors, respectively. Each configuration was subjected to a translation and rotations for comparison.

states (EDOS) of Fe_{30}, Ni_{30}, and Cu_{30} clusters from NWChem are plotted in Fig. 6.14. It is evident from the plots that both the FMC and CCD configurations produce almost identical

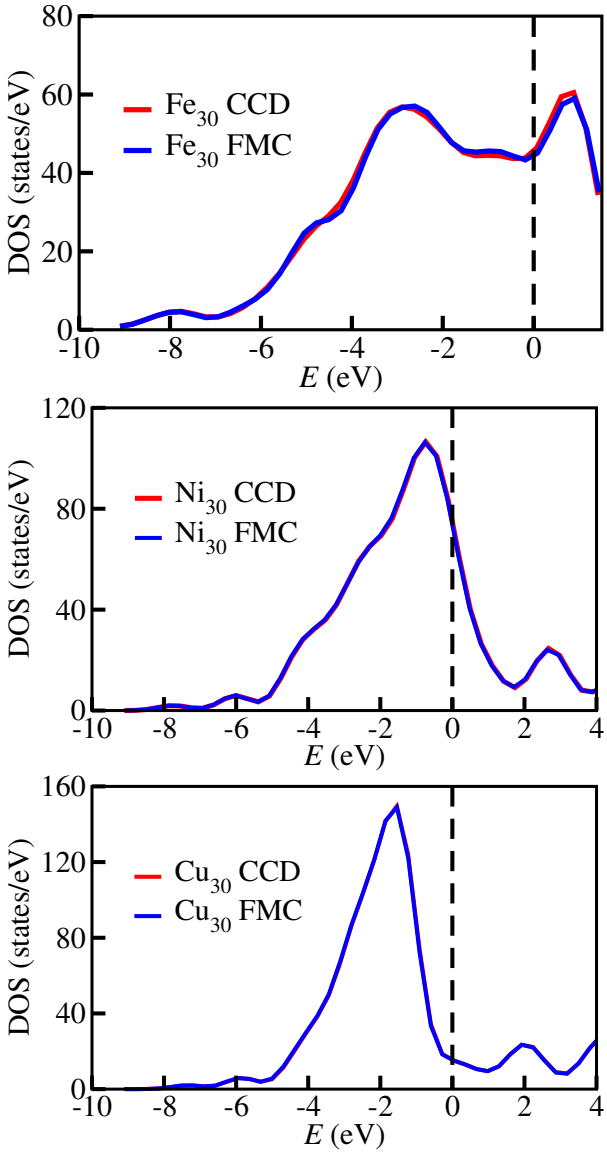

Figure 6.14: Electronic densities of states of 30-atom Fe, Ni, and Cu clusters. The results for the FMC and CCD clusters are shown in blue and red colors, respectively. The highest-occupied energy level is shown as a dashed vertical line (black) at 0 eV. For the purpose of comparison, we have broadened the eigenvalue distributions using a Gaussian function with a broadening parameter of 0.3 eV.

electronic densities of states throughout the energy spectrum. Thus, the electronic density of states of the clusters provide additional and independent corroboration that the clusters are (nearly) identical in nature.

6.5 Conclusions

In this chapter, we have studied the most stable structures of the transition-metal clusters of Fe, Ni, and Cu using classical simulations followed by quantum-mechanical total-energy relaxations using density-functional theory. Starting from a random structural configuration, the total energy of a cluster is computed using a force-biased Monte Carlo (FMC) approach, which efficiently explores the potential-energy landscape to determine the most likely configuration of the cluster at the putative global minimum and the low-energy isomers without employing any gradient-optimization techniques. Our method is illustrated using the Finnis-Sinclair potential for Fe clusters and the Sutton-Chen potential for Ni and Cu clusters, with sizes of up to 55 atoms for which the putative global minima and the corresponding geometry of the clusters are available in the literature from a number of sophisticated gradient-based optimization methods. In particular, we have compared our results from the classical FMC simulations with the corresponding structural data obtained from the Cambridge Cluster Database (CCD). The results suggest that the classical FMC method can produce structural configurations that are essentially identical to that of the CCD configurations as far as the total energy, the pair-correlation function, the bond-angle distribution, the atomic-coordination numbers, and the bond-orientational order parameter are concerned. Atom-by-atom comparisons between the FMC and CCD clusters are presented by mapping the former onto the latter using a transformation involving a translation and suitable Euler rotations. The stability of the classical FMC clusters is examined by perturbing the atomic positions and relaxing the perturbed configurations using the first-principles density-functional code NWChem. *Ab initio* total-energy relaxations of the FMC clusters indicate, with the exception of 13-atom Cu and Fe clusters, that the resulting relaxed structures are practically identical to the starting FMC structures as far as the pair-correlation distribution, the bond-angle distribution, and the first-shell coordination number of the atoms are concerned. For Fe_{13} and Ni_{13} clusters, we find that the icosahedral structure is the most stable structure, whereas Cu_{13} is found to adopt a bilayer or platelet-like structure in our study.

We conclude this chapter with the following observation. In this study, our *ab initio* search for new structures is by no means exhaustive as the primary goal of our work is to examine the effectiveness of the FMC approach in determining the ground-state structures of transition-metal clusters from classical potentials. Having achieved this goal, we have employed finite-temperature *ab initio* molecular-dynamics (AIMD) simulations to examine the credibility of the ground-state structure from classical potentials from the first-principles point of view. Since finite-temperature AIMD cannot adequately explore the potential-energy

surface in a limited simulation time of a few tens of picoseconds, as observed in numerous DFT studies on 13-atom transition-metal clusters (see section 6.3), alternative approaches to sample structures from the potential-energy surface of the clusters are necessary. In this chapter, we have offered such an approach and have shown unambiguously that the classical version of the approach can effectively determine the putative ground-state structures of a number of small transition-metal clusters. It is appropriate to expect that an *ab initio* version of the FMC algorithm would be highly suitable for an extensive search for the ground-state structure of transition-metal clusters using total energies and forces.

Chapter 7

SUMMARY

In this dissertation, we have demonstrated data-driven approaches for structural modeling of realistic atomistic models of complex amorphous solids. Experimental diffraction data play an important role in the structural characterizations of solids. While reverse Monte Carlo (RMC) and similar methods provide an elegant approach to (re)construct a three-dimensional model of non-crystalline solids, a satisfactory solution to the RMC problem is still not available. Based on a hybrid scheme and incorporating experimental diffraction data, a few structural constraints, and a total-energy functional, we presented an accurate structural solution of the inverse problem by developing a new information-driven inverse approach (INDIA) in Chapter 3. By introducing a subspace optimization technique, the difficulty associated with the optimization of the augmented objective function can be reduced considerably to determine optimal structural solutions, satisfying experiments, and a total-energy functional simultaneously. This method can produce nearly defect-free models of amorphous silicon which have structural, electronic, and vibrational properties fully consistent with experimental data. The realistic atomistic models of *a*-Si exhibit a clean gap around the Fermi level in the electronic spectrum.

In Chapter 4, we addressed a difficult inverse problem that involves the reconstruction of a three-dimensional model of tetrahedral amorphous semiconductors via inversion of diffraction data. We inverted the experimental data to reconstruct atomistic models of amorphous semiconductors even without using any total-energy functionals/forces. By posing the material-structure determination as a multi-objective optimization program, it has been shown that the problem can be solved accurately using experimental diffraction data and a few structural constraints which describe the local chemistry of amorphous networks. The information-based constraint RMC approach yields highly realistic models of *a*-Si, with no or only a few coordination defects ($\leq 1\%$), a narrow bond-angle distribution of width 9–11.5°, and an electronic gap of 0.8–1.4 eV. These data-driven information-based models have been found to produce electronic and vibrational properties of *a*-Si that match accurately with experimental data and rival that of the Wooten-Winer-Weaire (W3) models. This approach even can produce microstructural properties of realistic samples of a-Si from experiments, such as voids and vacancy-type defects, which cannot be addressed directly

using currently available computational methods. The study demonstrates that information-driven inverse approaches can enhance existing methodologies for modeling disordered materials based on an information paradigm. This brings a directional step-change in materials modeling computation.

After the success of material modeling, in Chapter 5, we studied an *ab initio* study of hydrogen dynamics inside nanometer-size voids in *a*-Si within the framework of the density-functional theory. Using the local density approximation and its generalized-gradient counterpart, the dynamics of hydrogen atoms inside the voids are examined with an emphasis on the diffusion of H atoms/molecules, and the resulting nanostructural changes of the void surfaces for a varying concentration of hydrogen load of 10 to 30 H atoms/void at the low and high temperature of 400 and 700 K, respectively. The microstructure of the hydrogen distribution on the void surfaces and the morphology of the voids are characterized by the presence of a significant number of monohydride Si–H bonds, along with a few dihydride Si–H_2 configurations. The study also reveals that a considerable number (about 10–45 at. %) of total H atoms inside voids can appear as H_2 molecules for a hydrogen load of 10–30 H atoms/void. By considering the translational kinetic energy of H atoms inside the voids, the kinetics of Si–H bond formation and dissociation during AIMD simulations can be approximately described and understood. Hydrogen atoms with significantly higher KE than average KE of the system are found to dissociate from Si–H bonds and the resulting isolated H atoms form new bonds with nearby active Si atoms by diffusing through the void region within a fraction of time.

We studied transitional-metal clusters (TMC) based on the Monte Carlo method in Chapter 6. We presented a force-biased Monte Carlo (FMC) method for structural modeling of the transition-metal clusters of Fe, Ni, and Cu of size 1–60 atoms. By employing the Finnis-Sinclair potential for Fe and the Sutton-Chen potential for Ni and Cu, the total energy of the clusters was minimized using the local gradient of the potentials in Monte Carlo simulations. Upon relaxation of the clusters using the first-principles density-functional code NWChemand, the structural configurations of the FMC clusters were analyzed and compared with the same from the Cambridge Cluster Database (CCD). The results show that the total-energy value and the structure of the FMC clusters are essentially identical to the corresponding value and the structure of the CCD clusters. The structural properties of the NWChem-relax FMC and CCD were compared from structural information of two- and three-body correlation functions, the local bonding environment of the atoms, and the geometry of the clusters. Further, we carried out *ab initio* molecular dynamics based on density functional theory to find the putative ground-state structures of 13-atom copper and silver clusters.

BIBLIOGRAPHY

[1] Elliott, S. R. *Physics of amorphous materials* (Longman Inc., New York, 1990), 2nd edn.

[2] Beeman, D., Tsu, R. & Thorpe, M. F. Structural information from the Raman spectrum of amorphous silicon. *Phys. Rev. B* **32**, 874–878 (1985).

[3] Branz, H. M. Hydrogen collision model: Quantitative description of metastability in amorphous silicon. *Phys. Rev. B* **59**, 5498–5512 (1999).

[4] Elliott, S. R. Medium-range structural order in covalent amorphous solids. *Nature* **354**, 445–452 (1991).

[5] Dahal, D., Warren, H. & Biswas, P. On the origin and structure of the first sharp diffraction peak of amorphous silicon. *physica status solidi (b)* 2000447 (2021).

[6] Sørensen, S. S., Biscio, C. A. N., Bauchy, M., Fajstrup, L. & Smedskjaer, M. M. Revealing hidden medium-range order in amorphous materials using topological data analysis. *Science Advances* **6** (2020).

[7] Morigaki, K. & Ogihara, C. Amorphous semiconductors: Structure, optical, and electrical properties. In Kasap, S. & Capper, P. (eds.) *Springer Handbook of Electronic and Photonic Materials* (Springer, Cham, 2017).

[8] Nemanich, R., Lucovsky, G., Pollard, W. & Joannopoulos, J. Spectroscopic evidence for bonding coordination defects in amorphous As. *Solid State Communications* **26**, 137–139 (1978).

[9] Street, R. *Technology and Applications of Amorphous Silicon* (Springer, Berlin, 2000).

[10] Taguchi, M. *et al.* Record efficiency hit solar cell on thin silicon wafer. *IEEE J. Photovoltaics* **4**, 96–99 (2014).

[11] Carlson, D. E. & Wronski, C. R. Amorphous silicon solar cell. *Appl. Phys. Lett.* **28**, 671–673 (1976).

[12] Powell, M. J. The physics of amorphous-silicon thin-film transistors. *IEEE Trans. Electron Devices* **36**, 2753–2763 (1989).

[13] Street, R. A. Thin-film transistors. *Adv. Materials* **21**, 2007–2022 (2009).

[14] Cui, L.-F., Ruffo, R., Chan, C. K., Peng, H. & Cui, Y. Crystalline-Amorphous CoreâĹŠShell Silicon Nanowires for High Capacity and High Current Battery Electrodes. *Nano Letters* **9**, 491–495 (2009).

[15] Key, B. *et al.* Real-time nmr investigations of structural changes in silicon electrodes for lithium-ion batteries. *J. Am. Chem. Soc.* **131**, 9239–9249 (2009).

[16] Veldhorst, M. *et al.* A two-qubit logic gate in silicon. *Nature* **526**, 410âĂŞ414 (2015).

[17] Khare, S. V., Nakhmanson, S. M., Voyles, P. M., Keblinski, P. & Abelson, J. R. Evidence from atomistic simulations of fluctuation electron microscopyfor preferred local orientations in amorphous silicon. *Appl. Phys. Lett.* **85**, 745–747 (2004).

[18] Gibson, J., Treacy, M. & Voyles, P. Atom pair persistence in disordered materials from fluctuation microscopy. *Ultramicroscopy* **83**, 169–178 (2000).

[19] Gibson, J. M., Treacy, M. M. J., Sun, T. & Zaluzec, N. J. Substantial Crystalline Topology in Amorphous Silicon. *Phys. Rev. Lett.* **105**, 125504 (2010).

[20] Bartenev, G. M. *The Structure and Mechanical Properties of Inorganic Glasses* (Wolters-Noordhoff, 1970).

[21] Zachariasen, W. H. The atomic arrangement in glass. *J. Am. Chem. Soc.* **54**, 3841–3851 (1932).

[22] Wooten, F., Winer, K. & Weaire, D. Computer generation of Structural Models of Amorphous Si and Ge. *Phys. Rev. Lett.* **54**, 1392–1395 (1985).

[23] Barkema, G. T. & Mousseau, N. High-quality continuous random networks. *Phys. Rev. B* **62**, 4985–4990 (2000).

[24] Atta-Fynn, R. & Biswas, P. Nearly defect-free dynamical models of disordered solids: The case of amorphous silicon. *J. Chem. Phys.* **148**, 204503 (2018).

[25] Deringer, V. L. *et al.* Realistic Atomistic Structure of Amorphous Silicon from Machine-Learning-Driven molecular dynamics. *J. Phys. Chem. Lett.* **9**, 2879–2885 (2018).

[26] Bernstein, N. *et al.* Quantifying Chemical Structure and Machine-Learned Atomic Energies in Amorphous and Liquid Silicon. *Angewandte Chemie International Edition* **58**, 7057–7061 (2019).

[27] Pedersen, A., Pizzagalli, L. & JÃşnsson, H. Optimal atomic structure of amorphous silicon obtained from density functional theory calculations. *New J. Phys.* **19**, 063018 (2017).

[28] Car, R. & Parrinello, M. Structural, Dymanical, and Electronic Properties of Amorphous Silicon: An *ab initio* Molecular-Dynamics Study. *Phys. Rev. Lett.* **60**, 204–207 (1988).

[29] Deringer, V. L. *et al.* Origins of structural and electronic transitions in disordered silicon. *Nature* **589**, 59–64 (2021).

[30] Gereben, O. & Pusztai, L. Structure of amorphous semiconductors: Reverse Monte Carlo studies on *a*-C, *a*-Si, and *a*-Ge. *Phys. Rev. B* **50**, 14136–14143 (1994).

[31] McGreevy, R. L. Reverse Monte Carlo modelling. *J. Phys.: Condens. Matter* **13**, R877 (2001).

[32] Biswas, P., Atta-Fynn, R. & Drabold, D. A. Reverse Monte Carlo modeling of amorphous silicon. *Phys. Rev. B* **69**, 195207 (2004).

[33] Limbu, D. K., Elliott, S. R., Atta-Fynn, R. & Biswas, P. Disorder by design: A data-driven approach to amorphous semiconductors without total-energy functionals. *Scientific Reports* **10**, 7742 (2020).

[34] Opletal, G., Petersen, T. C., Snook, I. K. & Russo, S. P. HRMC_2.0: Hybrid Reverse Monte Carlo method with silicon, carbon and germanium potentials. *Comp. Phys. Comm.* **184**, 1946 – 1957 (2013).

[35] Biswas, P., Tafen, D. N. & Drabold, D. A. Experimentally constrained molecular relaxation: The case of glassy $GeSe_2$. *Phys. Rev. B* **71**, 054204 (2005).

[36] Pandey, A., Biswas, P. & Drabold, D. A. Force-enhanced atomic refinement: Structural modeling with interatomic forces in a reverse Monte Carlo approach applied to amorphous Si and SiO_2. *Phys. Rev. B* **92**, 155205 (2015).

[37] Limbu, D. K., Atta-Fynn, R., Drabold, D. A., Elliott, S. R. & Biswas, P. Information-driven inverse approach to disordered solids: Applications to amorphous silicon. *Phys. Rev. Materials* **2**, 115602 (2018).

[38] Limbu, D. K., Atta-Fynn, R. & Biswas, P. Atomistic simulation of nearly defect-free models of amorphous silicon: An information-based approach. *MRS Advances* **4**, 87–93 (2019).

[39] Smets, A. H. M., Kessels, W. M. M. & van de Sanden, M. C. M. Vacancies and voids in hydrogenated amorphous silicon. *Appl. Phys. Lett.* **82**, 1547–1549 (2003).

[40] de Groot, F. High-Resolution X-ray Emission and X-ray Absorption Spectroscopy. *Chemical Reviews* **101**, 1779–1808 (2001).

[41] Treacy, M. M. J., Gibson, J. M., Fan, L., Paterson, D. J. & McNulty, I. Fluctuation microscopy: a probe of medium range order. *Reports on Progress in Physics* **68**, 2899–2944 (2005).

[42] Sekimoto, T., Matsumoto, M., Sagara, A., Hishida, M. & Terakawa, A. Changes in the vacancy size distribution induced by non-bonded hydrogens in hydrogenated amorphous silicon. *J. Non-Cryst. Solids* **447**, 207 – 211 (2016).

[43] Tabata, A., Fujii, S., Suzuoki, Y., Mizutani, T. & Ieda, M. X-ray photoelectron spectroscopy (XPS) of hydrogenated amorphous silicon carbide (a-Si_xC_{1-x}:H) prepared by the plasma CVD method. *J. Phys. D: Appl. Phys.* **23**, 316–320 (1990).

[44] Tersoff, J. & Hamann, D. R. Theory and Application for the Scanning Tunneling Microscope. *Phys. Rev. Lett.* **50**, 1998–2001 (1983).

[45] Park, Y., Choong, V., Gao, Y., Hsieh, B. R. & Tang, C. W. Work function of indium tin oxide transparent conductor measured by photoelectron spectroscopy. *Appl. Phys. Lett.* **68**, 2699–2701 (1996).

[46] Giessibl, F. J. Advances in atomic force microscopy. *Rev. Mod. Phys.* **75**, 949–983 (2003).

[47] Dang, Z. *et al.* In Situ Transmission Electron Microscopy Study of Electron Beam-Induced Transformations in Colloidal Cesium Lead Halide Perovskite Nanocrystals. *ACS Nano* **11**, 2124–2132 (2017).

[48] Young, D. L. *et al.* Nanostructure evolution in hydrogenated amorphous silicon during hydrogen effusion and crystallization. *Appl. Phys. Lett.* **90**, 081923 (2007).

[49] Lee, P. A., Citrin, P. H., Eisenberger, P. & Kincaid, B. M. Extended x-ray absorption fine structure—its strengths and limitations as a structural tool. *Rev. Mod. Phys.* **53**, 769–806 (1981).

[50] Muramatsu, S. *et al.* Small-angle X-ray scattering studies of a-$Si_{1-x}Ge_x$:H alloys. *J. Non-Cryst. Solids* **150**, 163–166 (1992).

[51] Khanna, R. K., Stranz, D. D. & Donn, B. A spectroscopic study of intermediates in the condensation of refractory smokes: Matrix isolation experiments of SiO. *J. Chem. Phys.* **74**, 2108–2115 (1981).

[52] Chabal, Y. J. & Patel, C. K. N. Infrared Absorption in a-Si:H: First Observation of Gaseous Molecular H_2 and Si−H Overtone. *Phys. Rev. Lett.* **53**, 210–213 (1984).

[53] von Keudell, A. & Abelson, J. R. Evidence for atomic H insertion into strained Si–Si bonds in the amorphous hydrogenated silicon subsurface from *in situ* infrared spectroscopy. *Appl. Phys. Lett.* **71**, 3832–3834 (1997).

[54] Boyce, J. B. & Stutzmann, M. Orientational Ordering and Melting of Molecular H_2 in an a-Si Matrix: NMR Studies. *Phys. Rev. Lett.* **54**, 562–565 (1985).

[55] Keating, P. N. Effect of Invariance Requirements on the Elastic Strain Energy of Crystals with Application to the Diamond Structure. *Phys. Rev.* **145**, 637–645 (1966).

[56] Stillinger, F. H. & Weber, T. A. Computer simulation of local order in condensed phases of silicon. *Phys. Rev. B* **31**, 5262–5271 (1985).

[57] Vink, R. L. C., Barkema, G. T., van der Weg, W. F. & Mousseau, N. Fitting the Stillinger–Weber potential to amorphous silicon. *J. Non-Cryst. Solids* **282**, 248 – 255 (2001).

[58] Štich, I., Car, R. & Parrinello, M. Amorphous silicon studied by *ab initio* molecular dynamics: Preparation, structure, and properties. *Phys. Rev. B* **44**, 11092–11104 (1991).

[59] Bartók, A. P., Payne, M. C., Kondor, R. & Csányi, G. Gaussian Approximation Potentials: The Accuracy of Quantum Mechanics, without the Electrons. *Phys. Rev. Lett.* **104**, 136403 (2010).

[60] Tucker, M. G., Keen, D. A., Dove, M. T., Goodwin, A. L. & Hui, Q. RMCProfile: reverse Monte Carlo for polycrystalline materials. *J. Phys.: Condens. Matter* **19**, 335218 (2007).

[61] Biswas, P., Atta-Fynn, R. & Drabold, D. A. Experimentally constrained molecular relaxation: The case of hydrogenated amorphous silicon. *Phys. Rev. B* **76**, 125210 (2007).

[62] Mott, N. F. Electrons in glass. *Contemporary Physics* **18**, 225–245 (1977).

[63] Bell, R. J. & Dean, P. Atomic vibrations in vitreous silica. *Discuss. Faraday Soc.* **50**, 55–61 (1970).

[64] Polk, D. Structural model for amorphous silicon and germanium. *J. Non-Crystalline Solids* **5**, 365–376 (1971).

[65] Guttman, L. Vibrational spectra of fourâĂŘcoordinated random networks with periodic boundary conditions. *AIP Conf. Proc.* **31**, 268–272 (1976).

[66] Hastings, W. Monte Carlo Sampling Methods Using Markov Chains and Their Applications. *Biometrika* **57**, 97–109 (1970).

[67] Allen, M. P. & Tildesley, D. J. *Computer Simulation of Liquids* (Oxford University Press, 1987).

[68] Parr, R. G. & Yang, W. *Density Functional Theory of Atoms and Molecules* (Oxford University Press, Oxford, 1989).

[69] Martin, R. M. *Electronic Structure: Basic Theory and Practical Methods* (Cambridge University Press, Cambridge, 2004).

[70] Hohenberg, P. & Kohn, W. Inhomogeneous electron gas. *Phys. Rev.* **136**, B864–B871 (1964).

[71] Kohn, W. & Sham, L. J. Self-Consistent Equations Including Exchange and Correlation Effects. *Phys. Rev.* **140**, A1133–A1138 (1965).

[72] Thomas, L. H. The calculation of atomic fields. *Mathematical Proceedings of the Cambridge Philosophical Society* **23**, 542–548 (1927).

[73] Fermi, E. Eine statistische methode zur bestimmung einiger eigenschaften des atoms und ihre anwendung auf die theorie des periodischen systems der elemente. *Zeitschrift für Physik* **48**, 73–79 (1928).

[74] Hartree, D. R. The wave mechanics of an atom with a non-coulomb central field. Part I. Theory and Methods. *Mathematical Proceedings of the Cambridge Philosophical Society* **24**, 89–110 (1928).

[75] Hartree, D. R. The wave mechanics of an atom with a non-coulomb central field. Part II. Some Results and Discussion. *Mathematical Proceedings of the Cambridge Philosophical Society* **24**, 111–132 (1928).

[76] Dirac, P. A. M. Note on exchange phenomena in the thomas atom. *Mathematical Proceedings of the Cambridge Philosophical Society* **26**, 376–385 (1930).

[77] Perdew, J. P. & Zunger, A. Self-interaction correction to density-functional approximations for many-electron systems. *Phys. Rev. B* **23**, 5048–5079 (1981).

[78] Perdew, J. P. & Yue, W. Accurate and simple density functional for the electronic exchange energy: Generalized gradient approximation. *Phys. Rev. B* **33**, 8800–8802 (1986).

[79] Perdew, J. P., Burke, K. & Ernzerhof, M. Generalized Gradient Approximation Made Simple. *Phys. Rev. Lett.* **77**, 3865–3868 (1996).

[80] Soler, J. M. *et al.* The SIESTA method for *ab initio* order-N materials simulation. *J. Phys.: Condens. Matter* **14**, 2745 (2002).

[81] McGreevy, R. L. & Pusztai, L. Reverse Monte Carlo Simulation: A New Technique for the determination of Disordered Structures. *Molecular Simulation* **1**, 359–367 (1988).

[82] Limbu, D. K. & Biswas, P. Structure of transition metal clusters: A force-biased Monte Carlo approach. *J. Phys.: Conf. Series* **921**, 012010 (2017).

[83] Limbu, D. K., Atta-Fynn, R., Drabold, D. A., Elliott, S. R. & Biswas, P. Structural properties of transition-metal clusters via force-biased Monte Carlo and *ab initio* calculations: A comparative study. *Phys. Rev. B* **96**, 174208 (2017).

[84] Limbu, D. K., Madueke, M. U., Atta-Fynn, R., Drabold, D. A. & Biswas, P. *Ab initio* density-functional studies of 13-atom Cu and Ag clusters. *J. Phys: Conf. Series* **1252**, 012009 (2019).

[85] Biswas, P. & Limbu, D. K. *Ab Initio* Hydrogen Dynamics and the Morphology of Voids in Amorphous Silicon. *physica status solidi (b)* 2000494 (2021).

[86] Hansen, J.-P. & McDonald, I. R. *Theory of Simple Liquids* (Academic Press, Burlington, 2006), 3rd edn.

[87] Keen, D. A. A comparison of various commonly used correlation functions for describing total scattering. *J. Applied Crystallography* **34**, 172–177 (2001).

[88] King, S. V. Ring Configurations in a Random Network Model of Vitreous Silica. *Nature* **213**, 1112 (1967).

[89] Franzblau, D. S. Computation of ring statistics for network models of solids. *Phys. Rev. B* **44**, 4925–4930 (1991).

[90] Drabold, D. A. Molecular dynamics simulations of network glasses. In *Insulating and Semiconducting Glasses*, 607–651 (World Scientific, Singapore, 2000).

[91] Biswas, P. Vibrational properties of amorphous silicon from tight-binding $O(N)$ calculations. *Phys. Rev. B* **65**, 125208 (2002).

[92] Maradudin, A. A., Montroll, E. W., Weiss, G. H. & Ipatova, I. P. *Theory of Lattice Dynamics in the Harmonic Approximation* (Academic Press, New York, 1971).

[93] Walters, J. K. & Newport, R. J. Reverse Monte Carlo modeling of amorphous germanium. *Phys. Rev. B* **53**, 2405–2410 (1996).

[94] Brodsky, M. H. & Title, R. S. Electron Spin Resonance in Amorphous Silicon, Germanium, and Silicon Carbide. *Phys. Rev. Lett.* **23**, 581–585 (1969).

[95] Kirsch, A. *An Introduction to the Mathematical Theory of Inverse Problems* (Springer-Verlag, New York, 1996).

[96] Born, M. & Green, H. S. A General Kinetic Theory of Liquids. I. The Molecular Distribution Functions. *Proceedings of the Royal Society of London Series A* **188**, 10–18 (1946).

[97] Kirkwood, J. G. The Statistical Mechanical Theory of Transport Processes I. General Theory. *J. Chem. Phys.* **14**, 180–201 (1946).

[98] Pandey, A., Biswas, P. & Drabold, D. A. Inversion of diffraction data for amorphous materials. *Scientific Reports* **6**, 33731 (2016).

[99] Cliffe, M. J., Dove, M. T., Drabold, D. A. & Goodwin, A. L. Structure Determination of Disordered Materials from Diffraction Data. *Phys. Rev. Lett.* **104**, 125501 (2010).

[100] Cliffe, M. J. *et al.* Structural simplicity as a restraint on the structure of amorphous silicon. *Phys. Rev. B* **95**, 224108 (2017).

[101] Igram, D., Bhattarai, B., Biswas, P. & Drabold, D. A. Large and realistic models of amorphous silicon. *J. Non-Cryst. Solids* **492**, 27 – 32 (2018).

[102] Djordjević, B. R., Thorpe, M. F. & Wooten, F. Computer model of tetrahedral amorphous diamond. *Phys. Rev. B* **52**, 5685–5689 (1995).

[103] Meredig, B. & Wolverton, C. A hybrid computational–experimental approach for automated crystal structure solution. *Nature Materials* **12**, 123–127 (2013).

[104] Biswas, P., Tafen, D. N., Atta-Fynn, R. & Drabold, D. The inclusion of experimental information in first principles modelling of materials. *J. Phys.: Condens. Matter* **16**, S5173–S5182 (2004).

[105] Biswas, P., Atta-Fynn, R., Chakraborty, S. & Drabold, D. A. Real space information from fluctuation electron microscopy: applications to amorphous silicon. *J. Phys.: Condens. Matter* **19**, 455202 (2007).

[106] Biswas, P., Drabold, D. A. & Atta-Fynn, R. Microstructure from joint analysis of experimental data and *ab initio* interactions: Hydrogenated amorphous silicon. *J. Appl. Phys.* **116**, 244305 (2014).

[107] Biswas, P. & Timilsina, R. Vacancies, microstructure and the moments of nuclear magnetic resonance: the case of hydrogenated amorphous silicon. *J. Phys.: Condens. Matter* **23**, 065801 (2011).

[108] Timilsina, T. & Biswas, P. A study of hydrogen microstructure in amorphous silicon via inversion of nuclear magnetic resonance spectra. *J. Phys.: Condens. Matter* **25**, 165801 (2013).

[109] Biswas, P., Paudel, D., Atta-Fynn, R., Drabold, D. A. & Elliott, S. R. Morphology and Number Density of Voids in Hydrogenated Amorphous Silicon: An *ab initio* Study. *Phys. Rev. Applied* **7**, 024013 (2017).

[110] Prasai, K., Biswas, P. & Drabold, D. A. Sculpting the band gap: a computational approach. *Scientific Reports* **5**, 15522 (2015).

[111] Biswas, P. & Elliott, S. R. Nanoscale structure of microvoids in *a*-Si:H: a first-principles study. *J. Phys.: Condens. Matter* **27**, 435201 (2015).

[112] Hadamard, J. *Lectures on the Cauchy Problem in Linear Partial Differential Equations* (Yale University Press, New Haven, 1923).

[113] Artacho, E., Sánchez-Portal, D., Ordejón, P., García, A. & Soler, J. M. Linear-Scaling ab-initio Calculations for Large and Complex Systems. *Phys. Stat. Sol. (b)* **215**, 809–817 (1999).

[114] Troullier, N. & Martins, J. Efficient pseudopotentials for plane-wave calculations. *Phys. Rev. B* **43**, 1993–2006 (1991).

[115] Laaziri, K. *et al.* High-energy x-ray diffraction study of pure amorphous silicon. *Phys. Rev. B* **60**, 13520–13533 (1999).

[116] Pandey, A., Biswas, P., Bhattarai, B. & Drabold, D. A. Realistic inversion of diffraction data for an amorphous solid: The case of amorphous silicon. *Phys. Rev. B* **94**, 235208 (2016).

[117] Roorda, S. *et al.* Structural relaxation and defect annihilation in pure amorphous silicon. *Phys. Rev. B* **44**, 3702–3725 (1991).

[118] Donovan, E. P., Spaepen, F., Turnbull, D., Poate, J. M. & Jacobson, D. C. Heat of crystallization and melting point of amorphous silicon. *Appl. Phys. Lett.* **42**, 698–700 (1983).

[119] Steinhardt, P. J., Nelson, D. R. & Ronchetti, M. Bond-orientational order in liquids and glasses. *Phys. Rev. B* **28**, 784–805 (1983).

[120] Weaire, D. & Thorpe, M. F. Electronic Properties of an Amorphous Solid. I. A Simple Tight-Binding Theory. *Phys. Rev. B* **4**, 2508–2520 (1971).

[121] Kageyama, S., Akagawa, M. & Fujiwara, H. Dielectric function of *a*-Si:H based on local network structures. *Phys. Rev. B* **83**, 195205 (2011).

[122] Zink, B. L., Pietri, R. & Hellman, F. Thermal Conductivity and Specific Heat of Thin-Film Amorphous Silicon. *Phys. Rev. Lett.* **96**, 055902 (2006).

[123] Kamitakahara, W. A. *et al.* Measurement of Phonon Densities of States for Pure and Hydrogenated amorphous Silicon. *Phys. Rev. Lett.* **52**, 644–647 (1984).

[124] Guinier, A. & Fournet, G. *Small-angle scattering of x rays* (John Wiley & Sons, Inc., New York, 1955).

[125] Warren, B. E. *X-ray diffraction* (Addison-Wesley Publishing Company, Inc., Reading, Mass., 1969).

[126] Strong, S. L. & Kaplow, R. The structure of crystalline B_2O_3. *Acta Cryst. B* **24**, 1032–1036 (1968).

[127] Kaplow, R., Rowe, T. A. & Averbach, B. L. Atomic arrangement in vitreous selenium. *Phys. Rev.* **168**, 1068–1079 (1968).

[128] Keen, D. A. & McGreevy, R. L. Structural modelling of glasses using reverse Monte Carlo simulation. *Nature* **344**, 423âĂŞ425 (1990).

[129] Klazes, R. H., van den Broek, M. H. L. M., Bezemer, J. & Radelaar, S. Determination of the optical bandgap of amorphous silicon. *Philosophical Magazine B* **45**, 377–383 (1982).

[130] Biswas, P., Barkema, G. T., Mousseau, N. & van der Weg, W. F. Efficient tight-binding Monte Carlo structural sampling of complex materials. *Europhysics Letters* **56**, 427–433 (2001).

[131] von Keudell, A. & Abelson, J. R. The interaction of atomic hydrogen with very thin amorphous hydrogenated silicon films analyzed using in situ real time infrared spectroscopy: Reaction rates and the formation of hydrogen platelets. *J. Appl. Phys.* **84**, 489 (1998).

[132] Paudel, D., Atta-Fynn, R., Drabold, D. A., Elliott, S. R. & Biswas, P. Small-angle x-ray scattering in amorphous silicon: A computational study. *Phys. Rev. B* **97**, 184202 (2018).

[133] Gereben, O. & Pusztai, L. Extension of the invariant environment refinement technique + reverse Monte Carlo method of structural modelling for interpreting experimental structure factors: The cases of amorphous silicon, phosphorus, and liquid argon. *J. Chem. Phys.* **135**, 084111 (2011).

[134] Errington, J. R. & Debenedetti, P. G. Relationship between structural order and the anomalies of liquid water. *Nature* **409**, 318–321 (2001).

[135] DeWolf, S., Descoeudres, A., Holman, Z. & Ballif, C. High-efficiency silicon heterojunction solar cells: A review. *Green* **2**, 7–24 (2012).

[136] Ge, J., Ling, Z., Wong, J., Mueller, T. & Aberle, A. Optimisation of Intrinsic *a*-Si:H Passivation Layers in Crystalline-amorphous Silicon Heterojunction Solar Cells. *Energy Procedia* **15**, 107 – 117 (2012).

[137] Staebler, D. L. & Wronski, C. R. Reversible conductivity changes in discharge-produced amorphous Si. *Appl. Phys. Lett.* **31**, 292–294 (1977).

[138] Su, T., Taylor, P. C., Ganguly, G. & Carlson, D. E. Direct Role of Hydrogen in the Staebler-Wronski Effect in Hydrogenated Amorphous Silicon. *Phys. Rev. Lett.* **89**, 015502 (2002).

[139] Bobela, D. C., Branz, H. M. & Stradins, P. Anneal treatment to reduce the creation rate of light-induced metastable defects in device-quality hydrogenated amorphous silicon. *Appl. Phys. Lett.* **98**, 201908 (2011).

[140] Chakraborty, S. & Drabold, D. A. Static and dynamic properties of hydrogenated amorphous silicon with voids. *Phys. Rev. B* **79**, 115214 (2009).

[141] Biswas, P., Paudel, D., Atta-Fynn, R. & Elliott, S. R. Temperature-induced nanostructural evolution of hydrogen-rich voids in amorphous silicon: a first-principles study. *Nanoscale* **12**, 1464–1477 (2020).

[142] Guerrero, E. & Strubbe, D. A. Computational generation of voids in *a*-Si and *a*-Si:H by cavitation at low density. *Phys. Rev. Materials* **4**, 025601 (2020).

[143] Sekimoto, T., Matsumoto, M. & Terakawa, A. Dense restructuring of amorphous silicon network induced by non-bonded hydrogen. *Jpn. J. Appl. Phys.* **57**, 08RB07 (2018).

[144] Mahan, A. H. *et al.* Structural properties of hot wire *a*-Si:H films deposited at rates in excess of 100 Å/s. *J. Appl. Phys* **90**, 5038–5047 (2001).

[145] Junquera, J., Paz, O., Sánchez-Portal, D. & Artacho, E. Numerical atomic orbitals for linear-scaling calculations. *Phys. Rev. B* **64**, 235111 (2001).

[146] Nosé, S. A unified formulation of the constant temperature molecular dynamics methods. *J. Chem. Phys.* **81**, 511–519 (1984).

[147] Beyer, W. Diffusion and evolution of hydrogen in hydrogenated amorphous and microcrystalline silicon. *Solar Energy Materials and Solar Cells* **78**, 235 – 267 (2003).

[148] Beyer, W. & Wagner, H. Determination of the hydrogen diffusion coefficient in hydrogenated amorphous silicon from hydrogen effusion experiments. *J. Appl. Phys* **53**, 8745–8750 (1982).

[149] Sekimoto, T., Matsumoto, M., Hishida, M. & Terakawa, A. Impact of microcrystalline-silicon surface-morphology on film quality and solar cell performance. *Jpn. J. Appl. Phys.* **53**, 095501 (2014).

[150] Kokalj, A. XCrySDen−a new program for displaying crystalline structures and electron densities. *J. Mol. Graph. Model.* **17**, 176 – 179 (1999).

[151] Wadell, H. Volume, Shape, and Roundness of Quartz Particles. *J. Geology* **43**, 250–280 (1935).

[152] Eiben, A. E. & Smith, J. E. *Introduction to Evolutionary Computing* (Springer, 2003).

[153] Engelbrecht, A. P. *Computational Intelligence – An introduction* (John Wiley and Sons, Ltd, 2007).

[154] Biswas, K. A thermally driven differential mutation approach for the structural optimization of large atomic systems. *J. Chem. Phys.* **147**, 104108 (2017).

[155] Rossky, P. J., Doll, J. D. & Friedman, H. L. Brownian dynamics as smart Monte Carlo simulation. *J. Chem. Phys.* **69**, 4628–4633 (1978).

[156] Li, Y.-L., Kinloch, I. A. & Windle, A. H. Direct Spinning of Carbon Nanotube Fibers from Chemical Vapor Deposition Synthesis. *Science* **304**, 276–278 (2004).

[157] Elliott, J., Shibuta, Y. & Wales, D. Global minima of transition metal clusters described by Finnis-Sinclair potentials: A comparison with semi-empirical molecular orbital theory. *Philosophical Magazine* **89**, 3311–3332 (2009).

[158] Doye, J. P. K. & Wales, D. J. Global minima for transition metal clusters described by Sutton-Chen potentials. *New J. Chem.* **22**, 733–744 (1998).

[159] Wales, D. J. & Doye, J. P. K. Global Optimization by Basin-Hopping and the Lowest Energy Structures of Lennard-Jones Clusters Containing up to 110 Atoms. *J. Phys. Chem. A* **101**, 5111–5116 (1997).

[160] Li, Z. & Scheraga, H. A. Monte Carlo-minimization approach to the multiple-minima problemin protein folding. *Proc. Natl. Acad. Sci.* **84**, 6611–6615 (1987).

[161] Valiev, M. *et al.* Nwchem: A comprehensive and scalable open-source solution for large scale molecular simulations. *Comput. Phys. Commun.* **181**, 1477 – 1489 (2010).

[162] Lathiotakis, N. N., Andriotis, A. N., Menon, M. & Connolly, J. Structure and stability of ni clusters: A tight-binding molecular-dynamics study. *Europhys. Lett.* **29**, 135–140 (1995).

[163] Grigoryan, V. G. & Springborg, M. Structure and energetics of ni clusters with up to 150 atoms. *Chem. Phys. Lett.* **375**, 219 – 226 (2003).

[164] Luo, C. A possible packing sequence of nickel clusters: Ni_3–Ni_2. *New J. Phys.* **4**, 10 (2002).

[165] Montejano-Carrizales, J. M., Iñiguez, M. P., Alonso, J. A. & López, M. J. Theoretical study of icosahedral Ni clusters within the embedded-atom method. *Phys. Rev. B* **54**, 5961–5969 (1996).

[166] Gupta, R. P. Lattice relaxation at a metal surface. *Phys. Rev. B* **23**, 6265–6270 (1981).

[167] Massobrio, C., Pasquarello, A. & Car, R. Structural and electronic properties of small copper clusters: a first principles study. *Chem. Phys. Lett.* **238**, 215 – 221 (1995).

[168] Calaminici, P., Köster, A. M., Russo, N. & Salahub, D. R. A density functional study of small copper clusters: $Cu_n (n \leq 5)$. *J. Chem. Phys.* **105**, 9546–9556 (1996).

[169] Oviedo, J. & Palmer, R. E. Amorphous structures of cu, ag, and au nanoclusters from first principles calculations. *J. Chem. Phys.* **117**, 9548–9551 (2002).

[170] Chang, C. M. & Chou, M. Y. Alternative Low-Symmetry Structure for 13-Atom Metal Clusters. *Phys. Rev. Lett.* **93**, 133401 (2004).

[171] Aprà, E., Ferrando, R. & Fortunelli, A. Density-functional global optimization of gold nanoclusters. *Phys. Rev. B* **73**, 205414 (2006).

[172] Longo, R. C. & Gallego, L. J. Structures of 13-atom clusters of fcc transition metals by *ab initio* and semiempirical calculations. *Phys. Rev. B* **74**, 193409 (2006).

[173] Yang, M., Jackson, K. A., Koehler, C., Frauenheim, T. & Jellinek, J. Structure and shape variations in intermediate-size copper clusters. *J. Chem. Phys.* **124**, 024308 (2006).

[174] Wang, L.-L. & Johnson, D. D. Density functional study of structural trends for late-transition-metal 13-atom clusters. *Phys. Rev. B* **75**, 235405 (2007).

[175] Pereiro, M., Baldomir, D. & Arias, J. E. Unexpected magnetism of small silver clusters. *Phys. Rev. A* **75**, 063204 (2007).

[176] Hu, C. H., Chizallet, C., Toulhoat, H. & Raybaud, P. Structural, energetic, and electronic trends in low-dimensional late-transition-metal systems. *Phys. Rev. B* **79**, 195416 (2009).

[177] Aguilera-Granja, F., García-Fuente, A. & Vega, A. Comparative ab initio study of the structural, electronic, and magnetic trends of isoelectronic late $3d$ and $4d$ transition metal clusters. *Phys. Rev. B* **78**, 134425 (2008).

[178] Chou, J. P. *et al.* 13-atom metallic clusters studied by density functional theory: Dependence on exchange-correlation approximations and pseudopotentials. *Phys. Rev. B* **80**, 165412 (2009).

[179] Piotrowski, M. J., Piquini, P. & Da Silva, J. L. F. Density functional theory investigation of $3d$, $4d$, and $5d$ 13-atom metal clusters. *Phys. Rev. B* **81**, 155446 (2010).

[180] Chou, J. P., Hsing, C. R., Wei, C. M., Cheng, C. & Chang, C. M. *Ab initio* random structure search for 13-atom clusters of fcc elements. *J Phys: Condens. Matter* **25**, 125305 (2013).

[181] Datta, S., Raychaudhuri, A. K. & Saha-Dasgupta, T. First principles study of bimetallic $Ni_{13-n}Ag_n$ nano-clusters (n = 0-13): Structural, mixing, electronic, and magnetic properties. *J. Chem. Phys.* **146**, 164301 (2017).

[182] Baletto, F. & Ferrando, R. Structural properties of nanoclusters: Energetic, thermodynamic, and kinetic effects. *Rev. Mod. Phys.* **77**, 371–423 (2005).

[183] Martin, T. P. Shells of atoms. *Phys. Rep.* **273**, 199 – 241 (1996).

[184] Parks, E. K., Zhu, L., Ho, J. & Riley, S. J. The structure of small nickel clusters. II. Ni_{16}–Ni_{28}. *J. Chem. Phys.* **102**, 7377–7389 (1995).

[185] Parks, E. K., Nieman, G. C., Kerns, K. P. & Riley, S. J. Reactions of Ni_{38} with N_2, H_2, and CO: Cluster structure and adsorbate binding sites. *J. Chem. Phys.* **107**, 1861–1871 (1997).

[186] Parks, E. K., Nieman, G. C., Kerns, K. P. & Riley, S. J. The thermodynamics of nitrogen adsorption on nickel clusters: $Ni_{19} - Ni_{71}$. *J. Chem. Phys.* **108**, 3731–3739 (1998).

[187] Parks, E. K., Kerns, K. P. & Riley, S. J. The structure of nickelâĂŞiron clusters probed by adsorption of molecular nitrogen. *Chem. Phys.* **262**, 151 – 167 (2000).

[188] Henry, C. R. Surface studies of supported model catalysts. *Surf. Sci. Rep.* **31**, 231 – 325 (1998).

[189] Valden, M., Lai, X. & Goodman, D. W. Onset of catalytic activity of gold clusters on titania with the appearance of nonmetallic properties. *Science* **281**, 1647–1650 (1998).

[190] Joo, S. H. *et al.* Ordered nanoporous arrays of carbon supporting high dispersions of platinum nanoparticles. *Nature* **412**, 169–172 (2001).

[191] Entel, P. *et al.* First-principles investigations of multimetallic transition metal clusters. *Phil. Mag.* **88**, 2725–2738 (2008).

[192] Elliott, J. A., Hamm, M. & Shibuta, Y. A multiscale approach for modeling the early stage growth of single and multiwall carbon nanotubes produced by a metal-catalyzed synthesis process. *J. Chem. Phys.* **130**, 034704 (2009).

[193] Park, S.-J., Taton, T. A. & Mirkin, C. A. Array-based electrical detection of dna with nanoparticle probes. *Science* **295**, 1503–1506 (2002).

[194] Mirkin, C. A., Letsinger, R. L., Mucic, R. C. & Storhof, J. J. A dna-based method for rationally assembling nanoparticles into macroscopic materials. *Nature* **382**, 607 (1996).

[195] Wolf, M. D. & Landman, U. Genetic algorithms for structural cluster optimization. *J. Phys. Chem. A* **102**, 6129–6137 (1998).

[196] Poteau, R. & Pastor, G. M. Genetic algorithms for determining the topological structure of metallic clusters. *Eur. Phys. J. D* **9**, 235–241 (1999).

[197] Joswig, J.-O. & Springborg, M. Genetic-algorithms search for global minima of aluminum clusters using a Sutton-Chen potential. *Phys. Rev. B* **68**, 085408 (2003).

[198] Darby, S., Mortimer-Jones, T. V., Johnston, R. L. & Roberts, C. Theoretical study of Cu-Au nanoalloy clusters using a genetic algorithm. *J. Chem. Phys.* **116**, 1536–1550 (2002).

[199] Lazauskas, T., Sokol, A. A. & Woodley, S. M. An efficient genetic algorithm for structure prediction at the nanoscale. *Nanoscale* **9**, 3850–3864 (2017).

[200] Atiş, M., Aktaş, H. & Güvenç, Z. B. Structures and melting of Ag_n (n = 7, 12-14) clusters. *Modell. Simul. Mater. Sci. Eng.* **13**, 1411 (2005).

[201] Michaelian, K., Rendón, N. & Garzón, I. L. Structure and energetics of Ni, Ag, and Au nanoclusters. *Phys. Rev. B* **60**, 2000–2010 (1999).

[202] García-Rodeja, J., Rey, C., Gallego, L. J. & Alonso, J. A. Molecular-dynamics study of the structures, binding energies, and melting of clusters of fcc transition and noble metals using the voter and chen version of the embedded-atom model. *Phys. Rev. B* **49**, 8495–8498 (1994).

[203] Özçelik, S. & Güvenç, Z. B. Structures and melting of cu n (n= 13, 14, 19, 55, 56) clusters. *Surf. Sci.* **532**, 312–316 (2003).

[204] Erkoç, Ş. & Shaltaf, R. Monte Carlo computer simulation of copper clusters. *Phys. Rev. A* **60**, 3053–3057 (1999).

[205] Jellinek, J. & Garzón, I. L. Structural and dynamical properties of transition metal clusters. *Z. Phys. D- At., Mol. and Clu* **20**, 239–242 (1991).

[206] Rey, C., García-Rodeja, J. & Gallego, L. J. Computer simulation of the ground-state atomic configurations of Ni-Al clusters using the embedded-atom model. *Phys. Rev. B* **54**, 2942–2948 (1996).

[207] Luo, C. The structure of small nickel clusters: Ni_2-Ni_{19}. *Modell. Simul. Mater. Sci. Eng.* **8**, 95 (2000).

[208] Kabir, M., Mookerjee, A. & Bhattacharya, A. K. Structure and stability of copper clusters: A tight-binding molecular dynamics study. *Phys. Rev. A* **69**, 043203 (2004).

[209] Finnis, M. W. & Sinclair, J. E. A simple empirical *N*-body potential for transition metals. *Philosophical Magazine A* **50**, 45–55 (1984).

[210] Finnis, M. W. & Sinclair, J. E. Erratum. *Philosophical Magazine A* **53**, 161 (1986).

[211] Sutton, A. P. & Chen, J. Long-range Finnis–Sinclair potentials. *Philosophical Magazine Letter* **61**, 139–146 (1990).

[212] Garzón, I. L. & Jellinek, J. Melting of gold microclusters. *Z. Phys. D-At., Mol. and Clu* **20**, 235–238 (1991).

[213] Posada-Amarillas, A. & Garzón, I. L. Vibrational analysis of Ni_n clusters. *Phys. Rev. B* **54**, 10362–10365 (1996).

[214] Häkkinen, H., Moseler, M. & Landman, U. Bonding in Cu, Ag, and Au Clusters: Relativistic Effects, Trends, and Surprises. *Phys. Rev. Lett.* **89**, 033401 (2002).

[215] Fernández, E. M., Soler, J. M., Garzón, I. L. & Balbás, L. C. Trends in the structure and bonding of noble metal clusters. *Phys. Rev. B* **70**, 165403 (2004).

[216] Kresse, G. & Furthmüller, J. Efficient iterative schemes for *ab initio* total-energy calculations using a plane-wave basis set. *Phys. Rev. B* **54**, 11169–11186 (1996).

[217] Mitas, L., Grossman, J. C., Stich, I. & Tobik, J. Silicon clusters of intermediate size: Energetics, dynamics, and thermal effects. *Phys. Rev. Lett.* **84**, 1479–1482 (2000).

[218] Pangali, C., Rao, M. & Berne, B. On a novel Monte Carlo scheme for simulating water and aqueous solutions. *Chem. Phys. Lett.* **55**, 413 – 417 (1978).

[219] Kleinman, L. & Bylander, D. M. Efficacious Form for Model Pseudopotentials. *Phys. Rev. Lett.* **48**, 1425–1428 (1982).

[220] Car, R. & Parrinello, M. Unified approach for molecular dynamics and density-functional theory. *Phys. Rev. Lett.* **55**, 2471–2474 (1985).

[221] Gutsev, G. L., Weatherford, C. W., Belay, K. G., Ramachandran, B. R. & Jena, P. An all-electron density functional theory study of the structure and properties of the neutral and singly charged M_{12} and M_{13} clusters: M=Sc-Zn. *J. Chem. Phy.* **138**, 164303 (2013).

[222] Wu, M., Kandalam, A. K., Gutsev, G. L. & Jena, P. Origin of the anomalous magnetic behavior of the $Fe_{13}{}^{+}$ cluster. *Phys. Rev. B* **86**, 174410 (2012).

[223] Frisch, M. J. *et al.* Gaussian 09 Revision E.01. Gaussian Inc. Wallingford CT 2009.

[224] Chaves, A. S., Piotrowski, M. J. & Da Silva, J. L. F. Evolution of the structural, energetic, and electronic properties of the 3*d*, 4*d*, and 5*d* transition-metal clusters (30 TMn systems for n = 2-15): a density functional theory investigation. *Phys. Chem. Chem. Phys.* **19**, 15484–15502 (2017).

[225] Hoppe, R. Effective coordination numbers (ECoN) and mean Active fictive ionic radii (MEFIR). *Z. Kristallogr.* **150**, 23–52 (1979).